UNIVERSITÀ
DEGLI STUDI
DI PADOVA

FACSIMILE FRONTESPIZIO TESI

Sede Amministrativa: Università degli Studi di Padova

Dipartimento di Ingegneria dell'informazione

CORSO DI DOTTORATO DI RICERCA IN: Ingegneria dell'informazione
CURRICOLO: Bioingegneria
CICLO: 29

IMAGE PROCESSING IN OPHTHALMOLOGY TOWARDS IMPROVED DIAGNOSTIC MARKERS

This research was made possible by a Marie Curie grant from the European Commission in the framework of the REVAMMAD ITN (Initial Training Research network), Project number 316990.

Supervisore: Alfredo Ruggeri

Dottorando: Pedro Guimarães Sá Correia

IMAGE PROCESSING IN OPHTHALMOLOGY TOWARDS IMPROVED DIAGNOSTIC MARKERS

Pedro Guimarães

University of Padova

Supervisor: Alfredo Ruggeri

ACKNOWLEDGMENTS

I would like to express my sincere gratitude to my advisor, Professor Alfredo Ruggeri for the opportunity, support, motivation, and knowledge. I would like to thank all the principal investigators (PIs) in the REVAMMAD project for their advice and insightful comments. I also thank my fellow early stage researchers (ESRs) for their friendship and collaboration.

Besides the people in the REVAMMAD project, I would like to thank everybody in the University of Padova that helped me during this time, from staff and professors, to lab mates. You made this ride so much easier and interesting. My sincere thanks to the team at Charité, Berlin, that helped me with my secondment.

I am grateful to Dr. Neil Lagali and collaborators, who provided me with knowledge and data, without which this work would not have been possible. I would also like to thank the University Hospital of Padova for the conjunctiva images provided.

Last but not the least, I have to thank my family and friends for always being there. A special thanks to my parents for supporting me in every step of my life. I have to thank my sister for overall being an amazing person. And finally, I want to thank my girlfriend and lifelong partner for being with me in every step of the way, for the constant support and encouragement, for all the help and advice, for everything.

Thank you for everything **·** **Grazie** infinitamente**·** **Obrigado** a todos

TABLE OF CONTENTS

LIST OF FIGURES

LIST OF TABLES

ABSTRACT

The eye is a window to the outside world. It takes in light from the environment, converts it to electrical signals, and forwards it to the brain. In a similar manner it has been regarded as a window to our health. By imaging the eye we can visualize blood vessels and nerves noninvasively. Thus, ophthalmic imaging may allow us to diagnose and monitor both ocular and systemic diseases.

The retina has been the main focus of this line of research. Nevertheless, within the eye other structures of interest exist. Blood vessels of the bulbar conjunctiva and nerve fibers from the corneal subbasal plexus can be easily imaged. However, studies on these structures are still few in comparison to the retina. In this work, we have developed novel software tools to explore and aid the exploration of these alternative research fields.

Conjunctival Blood Vessels Segmentation

The bulbar conjunctiva is a thin mucous membrane that runs over the anterior sclera. Due to its location and transparency, this highly vascularized tissue can be easily imaged. Vascular features such as width, tortuosity or branching angle, computed from conjunctiva vasculature, may lead to important predictors of disease. Furthermore, blood vessel detection in the conjunctiva can serve as a base towards blood flow velocity computation.

We propose a novel algorithm capable of segmenting blood vessels from conjunctival images. Vessel segmentation is achieved using the phase-congruency, a dimensionless quantity invariant to contrast and scale.

In our pilot experiments, a total of 40 slit-lamp microscopy images from the conjunctiva were used test the proposed algorithm. Most blood vessels from these images appear to be correctly traced. The low running time of the proposed algorithm is appropriate for the clinical setting.

Blood Flow Velocity from Video Recordings

The use of video cameras attached to microscopes has become common. Furthermore, *in vivo* measurements of blood flow velocity may provide novel and/or improved disease markers. Therefore, a software tool designed to measure the blood velocity from video recordings is of interest. In this work, such software is proposed.

The software tackles three main issues in velocity measurement from videos, the registration, segmentation, and finally the measuring itself. To quantitatively validate it, a computer simulation of blood flow was created. The software was also tested in videos of an animal model (chick chorioallantoic membrane). These were captured *in vivo* with different resolutions, frame rates, and even cameras. The proposed algorithm performed well in all our tests. The obtained results show the robustness achieved.

Corneal Nerves Segmentation

The automatic tracing of corneal nerves is an important step for the quantitative analysis of corneal nerves in daily clinical practice. The rationale of the proposed method is to minimize required computing time while still providing accurate results. Our method consists of two sequential steps – a thresholding step followed by a supervised classification. For the classification we use a support vector machines approach. The proposed fast technique allows features, such as corneal nerve density and tortuosity, to be computed in a few seconds.

To validate the obtained tracings, we evaluated the tracing accuracy and reliability of extracted clinical parameters (corneal nerves density and tortuosity). The proposed algorithm proved capable to correctly trace 0.89 ± 0.07 of the corneal nerves. The obtained performance level was comparable to a second human grader. Furthermore, the proposed approach compares favorably to other methods. For both evaluated clinical parameters the proposed approach performed well. An execution time of 0.61 ± 0.07 seconds per image was achieved. The proposed algorithm was applied successfully to mosaic images, with run times of the order of tens of seconds.

The achieved quality and processing time of the proposed method appear adequate for the application of this technique to clinical practice. The application of nerve tracing to mosaics covering a large area can be a key component in clinical studies aimed at investigating neuropathy influence in various ocular or systemic diseases.

Corneal Nerves Density Estimation: Application to Mosaic Images

The corneal nerve density is already an established disease marker. However, most studies have only relied on single confocal images to establish correlations to diseases. The problem is that the typical confocal image only covers a small area of the central cornea. In this work we explore the corneal nerve density as computed from wide-field mosaic images.

The corneal nerves density was automatically computed and compared to a manual approach. A Pearson correlation coefficient of 0.94 was achieved. Furthermore, the proposed automatic approach was around 100 times faster (10 to 50 seconds per mosaic) than manual one.

Nerve density analysis from mosaic images was compared to the combination of multiple single images. Both underestimation and overestimation bias were verified. Furthermore, the combination of multiple single images carries a large variability depending on the area of the cornea sampled. The obtained results, demonstrate the potential of fully-automatic corneal nerve density analysis from mosaic images.

Corneal Nerves Tortuosity

The correlation between corneal nerve tortuosity and pathology has been shown multiple times. However, because there isn't any *de facto* definition of tortuosity, reproducibility is poor. Indeed, many studies still rely on the manual observation and judgment of tortuosity.

Recently, two distinct forms of corneal nerve tortuosity have been identified, describing either short-range or long-range directional changes. In this study we were able to develop automatic corneal nerve tortuosity measurements that correctly and independently represent these two tortuosity definitions.

We show that a combination of mathematical tortuosity measurements improves on single metric results. Spearman rank correlation coefficients of 0.99 and 0.96 with respect to the short-range and long-range tortuosity ground-truths were obtained. These results show that the proposed tortuosity measurements highly correlate to clinical perception.

INTRODUCTION

THE HUMAN EYE

The human eye takes in light from the environment and focuses it into a thin layer of photoreceptor cells located in the retina that convert it to electrical signals. These are then transmitted to the visual cortex in the brain via the **optic nerve** through the **optic disk** [1], [2]. The anatomy of this sense organ will be shortly described in this section and is represented in Figure 1.

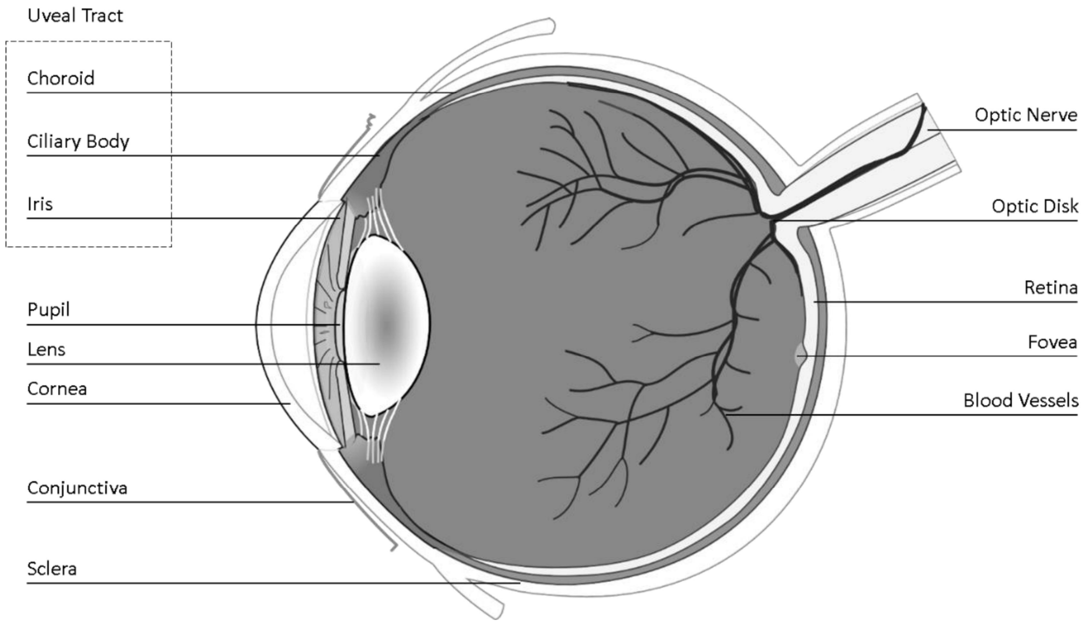

Figure 1: Human eye anatomy. Adapted from [3].

Light enters the eye through the tear film and into the **cornea**. This structure provides ideal light transmission due to the absence of blood vessels and tissue transparency [4], [5]. At its periphery the cornea is continuous with the **sclera** and the **conjunctiva.** The sclera is an opaque white tissue layer that surrounds the whole eye globe, the first out of three coats of the eye. The sclera maintains the eye globe shape, resists to internal and external forces, and serves also as an attachment for the ocular muscles [4], [5]. The sclera is anteriorly covered by a transparent and highly vascularized tissue layer, the conjunctiva. This thin membrane covers the eye globe and lines the eyelids.

Interior to the sclera lays a second layer of tissue (the second coat of the eye), the **uveal tract**, also known simply as uvea. It is formed by three distinct continuous structures: the iris, ciliary body, and choroid:

- The **iris** is a circular structure that controls the amount of light that enters the eye. This is accomplished by a set of muscles that can change the size of its center aperture, the **pupil**. The iris is located anteriorly to the lens and it defines eye color [6], [7].
- The **ciliary body** includes two components, the ciliary muscles and the ciliary epithelium. The ciliary muscles are strong smooth muscles that are connected to the lens and are able to adjust its refractive power. The ciliary epithelium is responsible for the production of the anterior chamber fluid (the aqueous humor) [6], [8].
- The **choroid** coats the eye in between the sclera and the retina. It is mainly composed by blood vessels as it plays an important role in nourishing the retina. The macula, a retinal region responsible for the central vision, is particularly dependent on the blood supply of the choroid [6], [7].

Before reaching the retina light beams also pass through the **crystalline lens**, that together with the cornea is responsible for focusing the light onto the retina [9], [10]. Two fluid-filled chambers exist in the eye: the **anterior chamber**, located between the cornea and the lens, which contains the **aqueous humor** that supplies nutrients to both these structures [7], [11], and the **vitreous chamber**, between the lens and the retina, containing the **vitreous humor** that accounts for the maintenance of the eye shape and contains phagocytic cells that are able to eliminate debris that might obstruct light transmission [12].

Finally the **retina**, the third and innermost coat of the eye, is where light is transformed into neural signals. Despite its location, it is still part of the central nervous system. It is a multilayered structure composed of multiple neuron types interconnected by synapses [13]. The light sensitive photoreceptor cells are located in the outermost layers of the retina. Light beams are focused on these cells as they are able to convert photons into neural signals through a process called phototransduction [13]–[15]. The signals are then transferred to bipolar cells, which in turn synapse with ganglion cells, which transmit the signal from the eye to the brain [13], [16]. The inner retina is vascularized, although no vessels exist in the macula region [14]. Both neural signals and blood circulation pass through the optic disk. No photoreceptors exist in this region, thus it is known as a blind spot [14].

Conjunctiva

The conjunctiva is a thin mucous membrane that runs inside the eyelids over the anterior sclera. It secretes a mucous that contributes to a smooth movement of the eyelids over the globe (lubricant function) and helps prevent the entrance of microbes into the eye [17], [18]. This mucous is also important for tear film stability. The conjunctiva also produces tears, although only a minimal amount when compared to the lacrimal gland [17], [19]. It is translucent, allowing the sclera to show through, and highly vascularized. Because the conjunctiva is subject to external factors, such as microbes, chemicals or foreign bodies, infection is common. The typical response includes redness, swelling, and exudation [17].

The conjunctiva can be divided into three different sections according to their location: **palpebral conjunctiva** that lines the eyelids, **bulbar conjunctiva** that covers the eye globe and the **fornix** that connects the palpebral and bulbar sections (Figure 2).

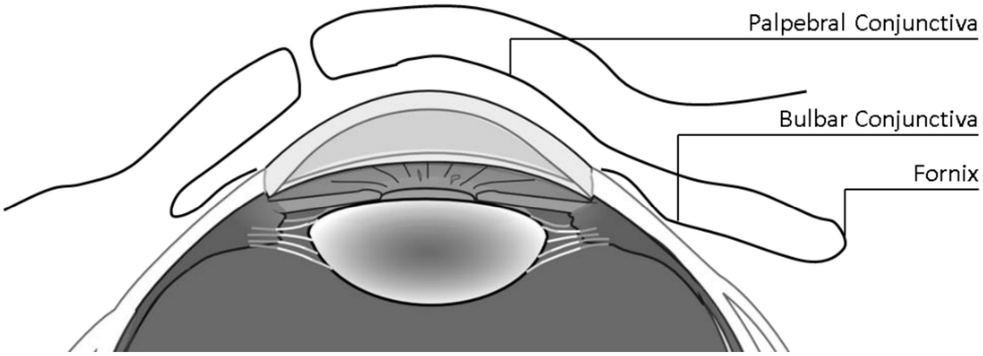

Figure 2: The three sections of the conjunctiva.

Histologically, two layers can be distinguished in the conjunctiva: a stratified epithelial layer, that is continuous with the corneal epithelium, and a connective tissue stromal layer, the submucosa. In the epithelial layer there are Goblet cells that produce the mucous component [17], [18]. Conjunctiva blood vessels are located in the submucosa [20].

A complex network tree of arterioles, venules, capillaries, and capillary meshes can be visualized in the conjunctiva. Vessel diameters range between 5 and 70 µm [17]. The network morphology can be very different between individuals. Since blood vessels are extremely close to ambient air, direct oxygen diffusion strongly influences blood oxygenation [17].

Cornea

The cornea is the first structure to interact with the light beams that enter the eye. It has two major functions: to refract and transmit these beams [4], [5]. Indeed it is the main refracting component of the eye, accounting for up to two thirds of its total refractive power. The lens accounts for the remaining one third [10]. Cornea's minimal scattering and absence of vasculature provide ideal transmission. The precise arrangement of its molecular components is of major importance to maintain transparency and therefore maximize light transmission [4], [5].

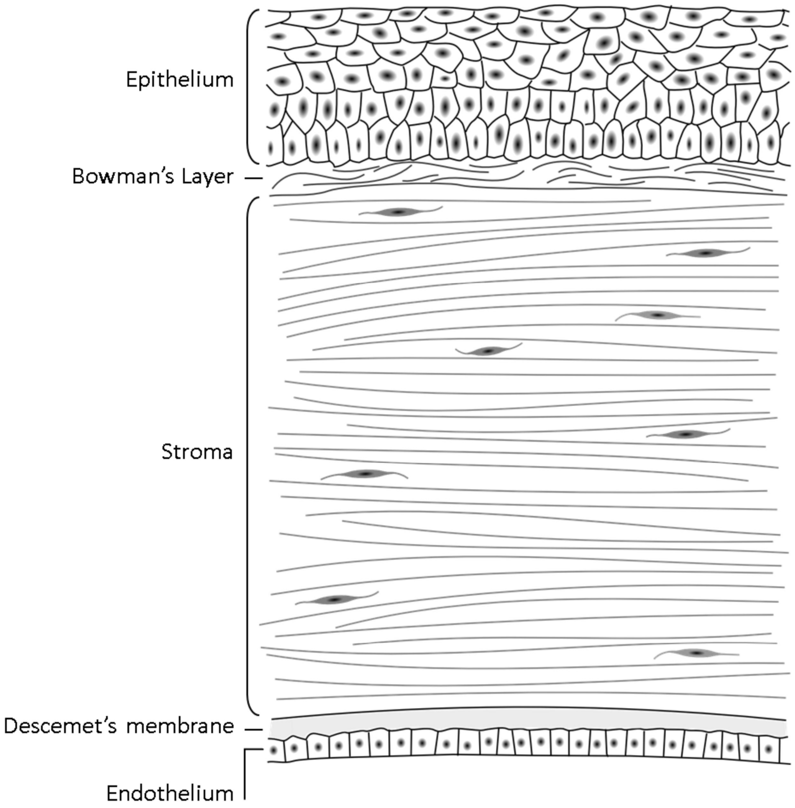

Figure 3: Human cornea anatomy.

The cornea is covered anteriorly by the tear film, while posteriorly it encapsulates, with the lens, the aqueous humor [7]. Histologically, it is a stratified structure composed by five layers (Figure 3):

- The **epithelium** is the outermost layer of the cornea. It is about five to seven cells thick. Surface epithelial cells are arranged in a regular form to provide the smoothest possible optical surface [4], [5]. This is important to minimize light scattering. To maintain corneal surface smoothness, these cells are regularly shed and replaced with cells from epithelial layers below. Basal cells, at the basal layer of the epithelium, differentiate and move up to replace wing cells, and wing cells differentiate and move up to replace shed surface cells. New basal cells are constantly being generated in the limbal region, a rim located at the cornea periphery [4], [5].
- The **Bowman's layer** is sometimes considered as a membrane. It is a transitional layer between the epithelium and the stroma. Indeed, there is no clear boundary between the Bowman's layer and the latter, as the transition is gradual. It is acellular mostly composed of smaller unbundled collagen fibrils. Bowman's layer does not regenerate if injured. However, it is still not clear whether this layer is needed to maintain normal corneal function [4].
- The **stroma** accounts for around 90% of the cornea's thickness. It is composed mostly of bundled collagen fibrils that run parallel to the corneal surface. Collagen fibrils arrangement is of major importance to maintain corneal transparency [4]. Keratocyte cells are present in the stroma. These are in charge of maintaining this layer by synthesizing collagen and extracellular matrix components, and play an important role during stroma wound healing [5].
- The **Descemet's membrane** is the base of the endothelium. It is composed of collagen that is constantly being secreted by the endothelial cells as this layer thickens throughout life. The arrangement of collagen give the membrane an elastic property [4].
- The **endothelium** borders the aqueous humor as it is the innermost layer of the cornea. It is composed of a single layer of regularly shaped (mostly hexagonal) flattened cells. These cells do not divide, as so the endothelium does not regenerate [5]. Upon cell death, other endothelium cells migrate, enlarge and morph to fill the left space. A minimum cell density in the endothelium is needed for proper function. Endothelial cells are responsible for controlling water flux to maintain the proper hydration of the cornea [4].

Corneal Nerves

The cornea is known for being one of the most sensitive tissues in the body. Indeed, corneal nerve density is 300 to 400 times higher than in the normal human skin. For this reason any corneal abrasion may be extremely painful. Besides the sensation of pain, the nerves in the cornea are responsible for the sensations of temperature and touch [4]. Furthermore, they contribute for the maintenance of a healthy corneal surface by playing an important role in the protective blink reflex, promotion of wound healing and lacrimal secretion [4], [21]–[23].

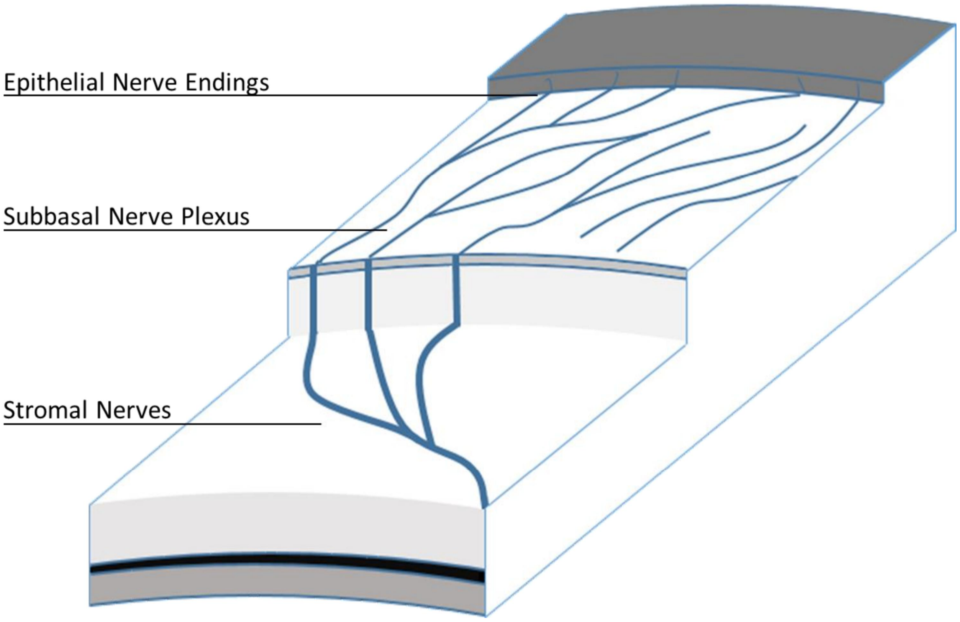

Figure 4: Corneal Nerves.

Three distinct nerve networks can be seen in the cornea (Figure 4). Nerves enter the cornea radially from the periphery at the mid-stroma level [4], [23], [24]. These then branch to form the first network at this level, parallel to the corneal surface. About 2 to 3 mm after they enter the cornea, nerves lose their myelin sheath [4]. Myelin absence is important for corneal transparency. However, covering from Schwann cell still remains [4]. Some stromal nerves then turn upwards and penetrate the Bowman's layer [22]–[24]. These then branch to form a second network, parallel to the corneal surface, right below the basal cells of the epithelium, the subbasal nerve plexus [23]. At this level Schwann cell covering is lost [4]. The final nerve network is located within the epithelium as some branches from the second network enter this layer and terminate as naked nerve endings between the epithelial cells [23], [24].

A DIAGNOSTIC WINDOW

For a long time the eye has been regarded as a window to the human body. By imaging the eye we can not only diagnose ocular diseases, but also detect a number of systemic diseases. Ophthalmic imaging allows us to visualize microvessels and nerves noninvasively (Figure 5). Thus, symptomatic manifestations of diseases such as diabetes mellitus, multiple sclerosis, or cardiovascular diseases can be detected, diagnosed, and managed by looking at the eye.

The retina has been the main focus of this research field. Imaging modalities such as color fundus photography allows one to visualize retinal blood vessels (Figure 5). Changes in these vessels have been found to correlate to several cardiovascular [25]–[27] and cerebrovascular [25], [28]–[32] outcomes. Vascular properties such as vessel tortuosity or arteriolar diameter at bifurcations have been correlated with death from ischemic heart disease [28]. Arteriolar narrowing has been correlated with increased mortality from stroke [28]. Furthermore, multiple studies have found that the arteriovenous (A/V) ratio, *i.e.* the ratio between the diameter of arteries and veins, is highly correlated to diseases such as atherosclerosis and hypertension [33]–[35].

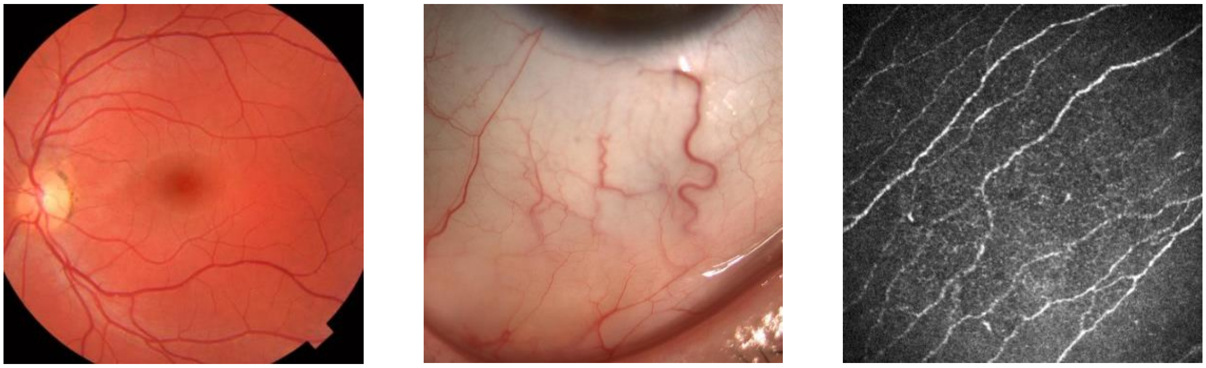

Figure 5: From left to right: retinal color fundus photography, conjunctival slit-lamp microscopy, and corneal confocal microscopy.

Diabetes mellitus is one of the most common chronic diseases in humans [36]–[38]. Its continued growth has led many to consider it the *epidemy* of the 21st century. It is characterized by the presence of high levels of blood glucose, known as hyperglycemia. As a consequence, blood vessels and nerve cells are damaged. In the retina, hyperglycemia can have nefarious effects such as fluid leakage, growth of new blood vessels, photoreceptor damage, and eventually blindness [39]. Diabetes complications in the retina are collectively referred to as diabetic retinopathy.

Despite research community focus on the retina, this is not the only structure of interest in the eye. One of the advantages of the retina is the possibility of direct visualization of microvasculature. Another structure in the eye offers such possibility – the bulbar conjunctiva (Figure 5). Due to its location and transparency, this highly vascularized tissue can be easily imaged in a clinical environment. The quantitative analysis of blood vessels from the conjunctiva parallels that of retinal analysis. Vascular features such as width, tortuosity or branching angle may lead to important predictors of disease. Furthermore, because it is unobstructed, high-resolution cameras can be readily used (without distortion), which opens up the opportunity for single blood cell visualization, *i.e.* the possibility of an easy and inexpensive *in vivo* method for measuring blood flow velocity [40]. Thus, the analysis of the conjunctiva can provide information not only on blood vessel morphology, but also on hemodynamics. The conjunctiva microcirculation has already been studied in diseases such as diabetes mellitus [41]. Methods for conjunctival blood flow velocity measurement have been previously reported [40], [42]–[45].

Recently, there has been an increasing interest in the cornea, specifically on the topic of corneal innervation (Figure 5). This may be explained by the possible correlation between corneal nerve injury and surgical interventions such as photorefractive keratectomy (PRK) and laser *in situ* keratomileusis (LASIK) [21], [46], [47]. After LASIK surgery the recovery of corneal sensation and the subbasal nerve morphology and density were shown to be strongly correlated [47]–[50]. Furthermore, corneal nerve density has been shown to be a biomarker of peripheral nerve degeneration. Some nerve properties, such as nerve density or tortuosity, have been linked to systemic diseases such as diabetes mellitus and its complications [21], [23], [46], [51]–[54], cancer [55], and neurodegenerative diseases such as amyotrophic lateral sclerosis [56] or Parkinson’s disease [57].

Overall, the quantitative description of these eye structures can be and has been used to establish correlations to clinical outcomes, thus providing important tools to clinicians for an objective and improved diagnosis.

PURPOSE

This work was part of a European Union project, the Marie Curie initial training network (ITN) entitled **RE**tinal **VA**scular **M**odeling, **M**easurement **A**nd **D**iagnosis (REVAMMAD). The project was aimed at tackling some of the most severe diseases affecting the European Union using ophthalmic imaging. The project intended to “train a new generation of interdisciplinary scientists for the academic, clinical, and industrial sectors” to apply the latest vascular modeling and image analysis techniques into practice.

As the name indicates, the retinal vasculature was the main focus of the REVAMMAD project. Although retinal image analysis has already been shown to be an important asset for the diagnosis and monitoring of important chronic diseases such as hypertension and diabetes [26], [39], [58], [59], there is still little translation into clinical practice. The project brought together image analysts, modelers, and clinicians, and incentivized collaboration and idea exchange. REVAMMAD was designed to establish standard working procedures and tools across fields to try to unlock the potential of this field of research.

Despite the main focus of REVAMMAD in the retina, the purpose of my work was instead to look at other structures of interest in the human eye. Both corneal and conjunctival imaging systems are now common tools in a clinical environment. However, studies on these structures are still few when compared to the retina. I believe that there is an opportunity to establish improved or novel biomarkers through measurements of vascular morphology and hemodynamics from the conjunctiva, and nerve morphology from the cornea.

The goal of this work was to develop novel software tools to explore and aid the exploration of these alternative sources of information; to analyze corneal and/or conjunctival images and provide a lead way into novel and improved diagnostic markers.

VASCULAR TREE AND BLOOD FLOW ANALYSIS

The circulatory system is composed by all the blood vessels and organs that permit the circulation of blood. It is responsible for the transportation of oxygen, carbon dioxide, nutrients, hormones, and blood cells. The eye is the only place in the human body where blood vessels and the movement of single blood cells can be directly visualized. Local measurements taken in the eye of vascular morphology or hemodynamics, may be used to infer on the state of the entire circular system. In order to compute such measurements, the location of blood vessels must be known. In this chapter we present an algorithm capable of segmenting blood vessels from conjunctival images. This was then used as a basis to a software capable of measuring the blood flow velocity from video recordings, also presented in this chapter.

CONJUNCTIVAL BLOOD VESSELS SEGMENTATION

The study of blood vessel morphology and hemodynamics in the conjunctiva has several key advantages. Its location and transparency make the human bulbar conjunctiva easily accessible for examination. This means that simple imaging protocols using inexpensive noninvasive imaging methods, such as, slit-lamp microscopy or scanning laser ophthalmoscopy (SLO), are possible.

As aforementioned, measurements from conjunctival blood vessels may be used to infer on the state of the entire vascular system. Furthermore, blood circulation in this structure has some specific advantages when considering the brain vasculature. Conjunctival circulation replicates in many ways the brain. Both the eye and part of the brain are supplied by branches of the internal carotid artery, *i.e.*: similar caliber size vessels; similar distance from the main branching tree; parallels in fluid dynamics. The effects of blood pressure on the vascular network are presumably the same. Both structures are also located in the skull, which means that the same internal and external forces are exerted on both circulations [17], [60].

Figure 6: From left to right, inferior, nasal, superior, and temporal slit-lamp microscopy images from a single subject.

As aforementioned, the quantitative analysis of blood vessels has been proven to provide information on several diseases [27], [58], [61], [62]. Manual or semi-automatic processes are impractical in the daily clinical practice, due to their difficulty and execution time. Thus, several fully-automatic blood vessel segmentation approaches have been proposed. Most of these methods focus on retinal vasculature. Supervised pixel classification [63]–[66], matched filters [63], [67]–[70], or tracking-based methods [71], [72] are some of the many approaches proposed over the years.

From the literature, only a few algorithms have been proposed for segmenting the conjunctival blood vessels. Reza Pourreza *et al.* [73] in 2008, proposed a conjunctival blood vessel segmentation algorithm based on a local Radon transform. In 2011, Seyed M. Zabihi *et al.* [74] proposed a different method. A supervised classifier using artificial neural fuzzy inference system was used to classify each individual pixel based local binary patterns. Jzau-Sheng Lin *et al.* 2012 [75] relied on fuzzy C-means and modified cone responses to extract the blood vessels from the conjunctiva.

Materials and Methods

The conjunctiva of 10 healthy subjects was imaged using a digital camera attached to a SL 990 slit-lamp microscope (C.S.O., Scandicci, Italy). For each patient, 4 images from different regions of 960×1280 pixels with a magnification of 10× were acquired – one image per region (inferior, superior, nasal, and temporal). Figure 6 shows an example for a single subject.

Blood vessel segmentation is a well-studied topic (especially in the retina [63], [69], [76], [77]). However, when considering the conjunctiva, some specific challenges must be overcome:

- There is not a specific imaging protocol/system, *i.e.*, important features such as vessel scale and/or intensity histogram are not known;

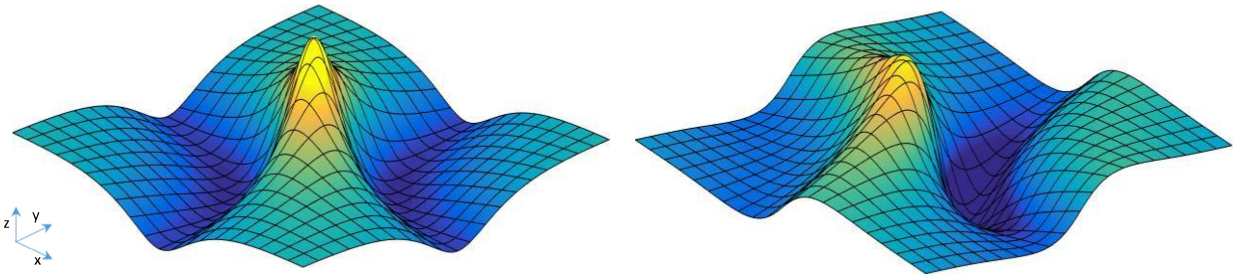

Figure 7: From left to right, even and odd logGabor kernels represented in the time domain, respectively.

- Other structures such as the iris or eyelashes may also be present in the image.

The green channel (from the RGB color map) is used for the segmentation as it presents improved contrast between the blood vessels and the background. Each image undergoes top-hat filtering, *i.e.* the morphological opened image is subtracted from the original grayscale image. This method has been shown to correct for different imaging artifacts such as uneven illumination and contrast.

Vessel segmentation is achieved using the phase-congruency (PC), a dimensionless quantity computed for each image pixel and invariant to contrast and scale [78]. It measures the agreement of the phase of the Fourier components of an image, with the same relevance being given to all frequency components, independent of gradient magnitude. P. Kovesi in [79] has shown the performance of edge and corner detection by PC. This method has already been proved to be useful for vascular segmentation [76], [80].

The PC takes into account the local phase information computed using 2-D logGabor even and odd kernels (Figure 7). It is computed as

$$PC = \frac{\sum_o \sum_n \omega_o \lfloor \varphi_{o,n} . \bar{\varphi}_o - \left| \varphi_{o,n} \times \bar{\varphi}_o \right| - T_o \rfloor}{\varepsilon + \sum_o \sum_n A_{o,n}}, \tag{1}$$

where $\lfloor . \rfloor$ is an operator that turns the enclosed quantity to zero if negative, A is the norm of the phase angle vector φ, and ε the smallest possible positive constant to avoid division by zero. The sigmoid weighting function ω_o is given by

$$\omega_o = \frac{1}{1 + exp[a(b - s_o)]}, \tag{2}$$

where a and b constants model the sigmoid. The orientation dependent spread of the logGabor filters s_o is given by

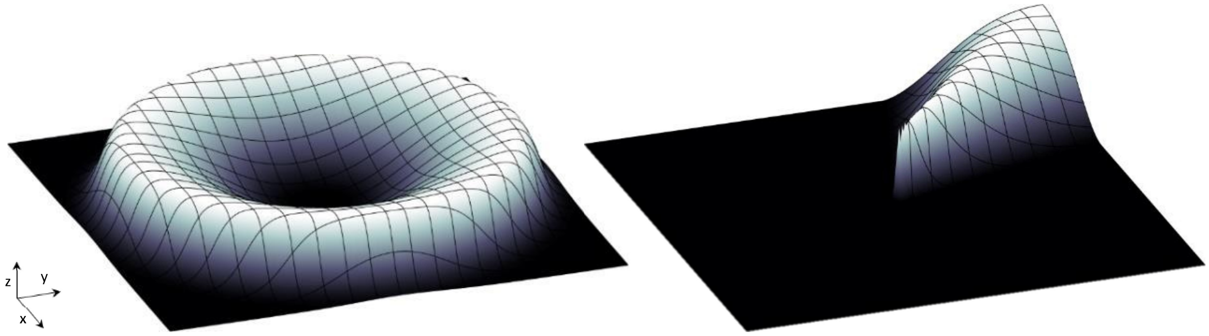

Figure 8: From left to right, the radial and angular components in the frequency domain that are combined to obtain the logGabor filter, respectively.

$$s_o = \frac{1}{N_n}\left(\frac{\sum_n A_{o,n}}{\varepsilon + A_o^{max}}\right). \tag{3}$$

The vector φ is defined as

$$\varphi_{no} = \begin{bmatrix} I_{o,n}^{even} & I_{o,n}^{odd} \end{bmatrix}. \tag{4}$$

The weighted mean phase angle vector $\bar{\varphi}_o$ is a unit vector computed as

$$\bar{\varphi}_o = \frac{1}{\sqrt{\left(\sum_n I_{o,n}^{even}\right)^2 + \left(\sum_n I_{o,n}^{odd}\right)^2}}\left[\sum_n I_{o,n}^{even} \quad \sum_n I_{o,n}^{odd}\right]. \tag{5}$$

I^{even} and I^{odd} result from the convolution of the image with the even and odd logGabor kernels, respectively.

A bank of 2-D log-Gabor kernels was used. These filters have been extensively used in the literature, specifically for vessel detection and enhancement [63], [67], [76]. Each of the filters in the bank results from the combination between a radial and an angular component, which limit the filter's frequency (scale) and orientation, respectively. As so, each logGabor filter has an exclusive orientation-scale (o, n) pairing. Both components are first computed and then multiplied in the frequency space to obtain the frequency domain logGabor filter. A representation of both components can be seen in Figure 8.

In the time domain, the even and the odd kernels are obtained as the real and imaginary parts of the filter, respectively. Figure 9 shows an example of the original image, the top-hat image, and the PC image, respectively.

Figure 9: From left to right, original image, top-hat filtered image, and phase-congruency. The region of interest is superimposed in red.

The phase congruency is then thresholded to obtain a binary image containing the segmented blood vessels. A region of interest (ROI) is automatically defined using the filtered images, color information and k-means clustering. This is to exclude the iris, eyelashes, and skin from the images. The region outside the ROI is not considered. Fragmented vessel segments are connected by morphological dilation of the resulting binary images, while isolated small segments are erased. The resulting segmentation is skeletonized to obtain the centerlines of the blood vessels.

Results

The proposed algorithm was used to segment all 40 images. Figure 10 shows examples of the obtained results. Visually, it appears that most blood vessels are correctly traced.

The time required to analyze a single image, using a prototype developed in MATLAB® (The MathWorks Inc., Natick, MA, USA) language, on a single core with an Intel® Core™ i7-4770 CPU (Intel Corporation, Santa Clara, CA, USA) at 3.4 GHz, was 1.83 ± 0.04 seconds (average ± standard deviation). Due to the lack of a ground truth segmentation no quantitative validation was performed.

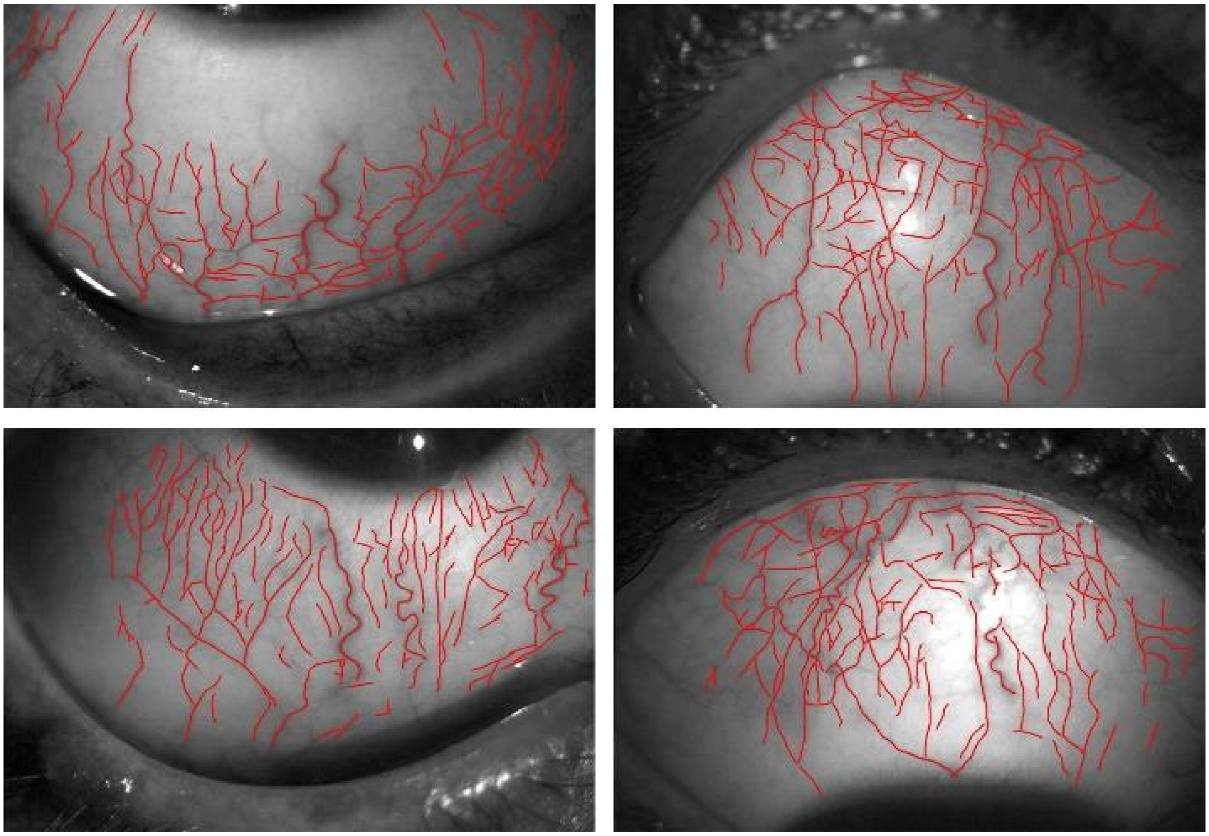

Figure 10: Four representative images: obtained segmentation results in red.

Discussion

Conjunctival blood vessels were imaged noninvasively using slit-lamp microscopy. A novel approach to segment the conjunctival vasculature was presented. In our pilot experiments, the proposed algorithm seems capable of correctly tracing the conjunctival blood vessels. The low time required for the segmentation deems the algorithm appropriate for the clinical setting. However, further tests are needed.

Conjunctival vessel segmentation software must overcome the lack of standardize imaging protocol. Thus, the use of phase-congruency, a dimensionless quantity invariant to contrast and scale. However, this method also has some limitations. The PC makes usage of logGabor kernels. For this reason, some vessels of the conjunctiva that run parallel, very close to each other, may appear fused. Furthermore, in cases of high vessel tortuosity, logGabor kernels may handle their high curvature poorly.

In this work, despite our efforts, no segmentation ground truth was available. Thus, the lack of quantitative validation results. This severely impacted both the development and optimization of the proposed algorithm. In the future, in order to continue the work done a ground truth must be created.

A robust conjunctival segmentation approach will open the way to fully-automatic analysis of its microvasculature, which may provide important clinical insight for several pathologies. Blood vessel analysis in the conjunctiva has the potential to be a valid add-on or even alternative to retinal analysis. Furthermore, blood vessel detection in the conjunctiva is specifically important as a base towards blood flow velocity computation.

BLOOD FLOW VELOCITY FROM VIDEO RECORDINGS

A microvascular network is never static or final. During the life of an organism, blood vessels grow, adapt and regress, in response to functional demands [81]. Processes like vasculogenesis, angiogenesis, remodeling or pruning, are crucial to maintain adequate function of the vascular system. The study of these mechanisms is of major importance as they play a central role in many diseases such as coronary heart disease, stroke, hypertension, and tumors [81].

Several factors contribute to the development and adaptation of a microvascular network. Among these, blood flow plays a pivotal role [82], [83], and thus, transport of blood is an important agent in the control of vascular network design. Properties such as blood pressure, shear stress, type of flow or even its composition, can trigger changes in the vessels [83]. Because of these reasons, to fully understand the fundamentals of the vascular system adaptation, the measurement of blood velocity is of paramount importance.

A number of techniques have been proposed to measure blood flow velocity. These include indirect methods (the velocity is derived), such as perfusion measurement methods, or direct ones (the velocity is measured), such as laser Doppler velocimetry or particle tracking techniques [84]. The latter includes the tracking of blood cells from videos. By computing the displacement of these cells from frame to frame, one can compute the blood velocity.

Due to the multi-purpose nature of video capture, the use of video cameras attached to microscopes has become common in many experimental labs. Therefore, a software tool designed to measure the blood velocity from video recordings is of interest. Furthermore, *in vivo* measurements of blood flow velocity could provide novel and/or improved disease markers. As aforementioned, the conjunctiva allows one to directly capture high-resolution videos of the vascular tree. Thus, it allows measurement of blood flow velocity. Studies have already demonstrated this possibility. Measurements from the conjunctiva could not only provide information on local disorders but also on systemic diseases.

Materials and Methods

A software tool capable of measuring blood flow velocity from video recordings is proposed. In this section the three modules that compose the software (Registration, Segmentation, and Velocity Measurement), as well as the data used for validation, are described in detail.

To quantitatively validate the proposed software, a computer simulation of blood flow was created. Furthermore, the software was tested with videos captured *in vivo* from an animal model – chick chorioallantoic membrane (CAM).

Simulated Data

In order to validate the proposed software, a simulation of red blood cells moving within a vessel was created. The usage of simulation as a validation tool has several advantages over real data. For the latter, there is no readily available ground truth. Validation would have to rely either on a second algorithm or imaging technique. In a simulation, all parameters can be independently manipulated by the user. The real velocity is known *a priori*. Furthermore, we can impose specific disturbances (such as low contrast or increased tortuosity) in a controlled manner that is difficult to replicate in real models.

First, an initial vessel centerline is computed. Given the frame coordinates x and y, the centerline CL is described by

$$CL(x) = c_a + c_b \cos\left(\frac{x}{c_c}\right), \qquad (6)$$

where the constants c_a, c_b, and c_c control the shape of the vessel. Different paths/streamlines, parallel to the vessels centerline, are computed along the vessel's width. Each path is then populated with 2D Gaussian blobs simulating blood cells. The intensity and size of the cells can be changed. In this way, different conditions (such as low contrast) may be tested.

The first 5% of each path length is denominated the generation zone, *i.e.* the region where new blood cells are generated. At each frame, there is a chance that up to 3 new blood cells are generated. As to maintain a constant stream of cells, the higher the velocity, the higher the probability of multiple cells being generated. The location where cells are generated within the generation zone is random. In one frame, two cells cannot be generated in the same position. However, they can appear fused if they are generated very close to each other.

The maximum velocity v_{max} is computed as

$$v_{max}(t) = v_a \left[\cos\left(\frac{t}{v_b}\right) + \cos\left(\frac{t}{v_c}\right)\right] + v_d, \tag{7}$$

where t is time and the constants $v_{\{a,b,\dots d\}}$ control the cosine functions behavior. v_{max} is not the final velocity but instead serves as a reference. The cell velocity v is different from cell to cell, and is computed as

$$v(t,r) = v_{max}(t) \times (G(r) - G(r)v_{rand}). \tag{8}$$

In a real vessel, due to wall resistance, blood flow velocity is maximal in the center of the vessel and it decreases as it gets closer to the vessel's wall. The Gaussian function $G(r)$ simulates this behavior (r is the distance of the cell to the center of the vessel, *i.e.* CL). Furthermore, v_{rand} is a random constant computed for each cell in the range $[0, 0.02]$. This constant creates random variability within a streamline (up to 2% of the cell's velocity).

At each frame, a low and a high frequency noise components are introduced in the background. Noise intensity can be changed in order to test different conditions.

To ease validation, frame rate of the generated sequence is set at 1 fr/s. The final sequence is cropped to exclude the generation zone. The ground truth velocity used for validation is computed as the average velocity of all cells at each streamline. Several video sequences with different parameters

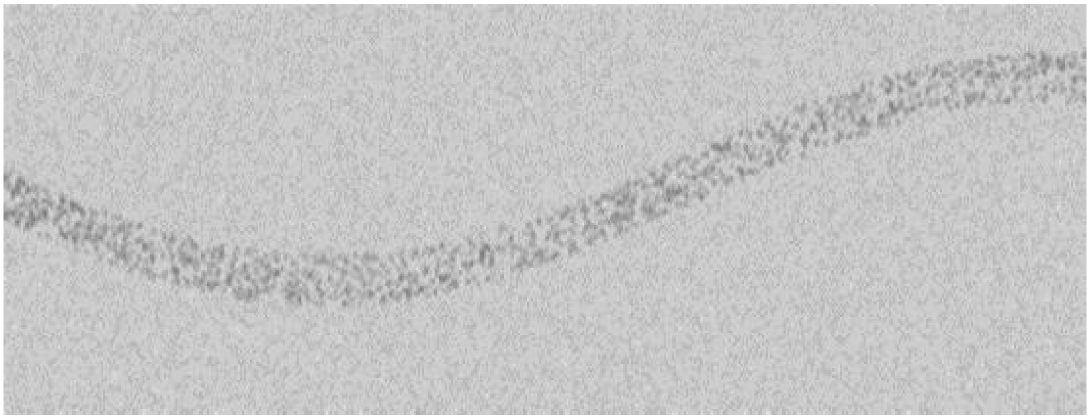

Figure 11: A single frame extracted from the created simulation of blood cells moving inside a blood vessels.

were generated to validate the proposed algorithm. All the generated sequences can be downloaded from[85]. Figure 11 shows a single frame from a simulation.

Video Recordings

The chick CAM is a common model for the study of microvascular network development, and is regularly used in the analysis of vascular flow [86]–[88]. Fertilized white leghorn chicken eggs (VALO BioMedia GmbH, Osterholz-Scharmbeck, Germany) were placed gently in an incubator (BB 16, Heraeus Instruments GmbH, Hanau, Germany) at 37.3°C (temperature) and with room humidity between 60 and 70%, on embryonic day 0 with their long axes parallel to the sea level. Seventy hours later the eggs were taken out of the incubator for embryo transfer performed as described in [89]. Once in the petri dish the *ex ovo* chicken embryos were brought back into the incubator for the development of chorioallantoic membrane.

In vivo recordings of the CAMs with two different cameras were performed on embryonic day 13. A high-resolution Sony camera (ILCE 6000, Tokyo, Japan) and a high recording speed MotionBlitz camera (EoSens mini1, Model MC 1370, Mikrotron GmbH, Unterschleiβheim, Germany) were used.

Both cameras were mounted on an intravital microscope (Zeiss Axioplan, Carl Zeiss, Oberkochen, Germany) equipped with an air objective (10x, NA 0.45, Zeiss, Germany). Figure 12 shows a single frame from both cameras.

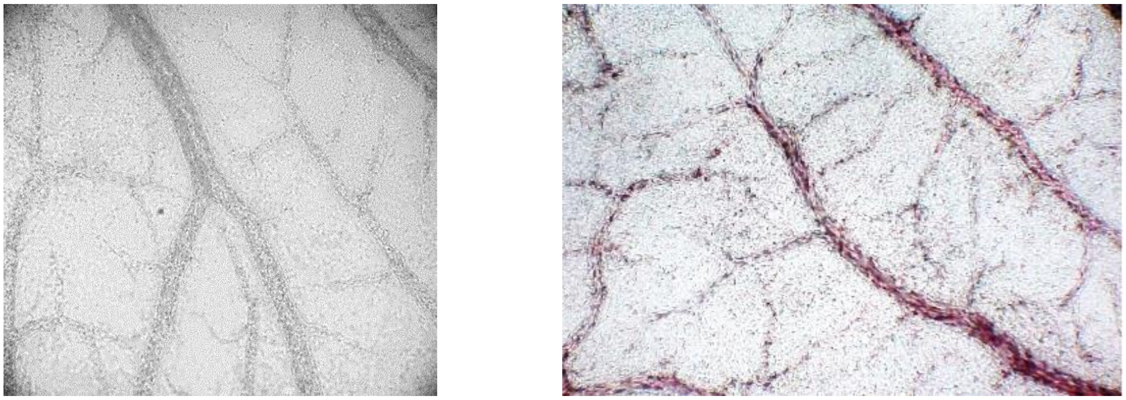

Figure 12: A single frame extracted from *in vivo* recordings of chickchorioallantoic membrane (CAM) microcirculations with the MotionBlitzEoSens mini1 (left) and Sony ILCE 6000 (right) cameras, respectively.

Registration

One of the main aspects to account for when measuring blood flow velocity from video recordings are irregular movements of the subject, the blood vessels, and/or the tissue. These constitute a severe problem when measuring blood flow velocity. It is assumed that each pixel corresponds to one unique location in the entire video. However, due to the movement, the time course of one pixel represents a signal from different locations. Because these movements influence the obtained measurements, motion correction is mandatory.

Motion correction is performed by estimating the movement between consecutive frames and subsequently realigning the data (registration). Due to the high frame count already necessary for velocity measurement, only small movements should be expected, with a large overlapping area between consecutive frames. Our tests showed that the registration between frames in the captured videos generally only involves moderate translations, while the need for rotation or scaling is negligible.

From the literature, a considerable number of medical image registration methods have been proposed [90]. The method of choice depends on the following key aspects:

- Depending on the used magnification, images may not exhibit any striking features such as sharp edges or corners;
- The translation between two consecutive frames may be minimal, especially when recording with a high frame rate – the algorithm must be able to measure sub-pixel translations;
- The frame rate used may be high, thus even a short video may contain a high number of frames – the chosen algorithm must be fast, but memory wise conservative.

In this work, an adaptation of the phase correlation method was applied. The main advantages of this method are the algorithm computing speed and robustness to imaging artifacts. First, the gradient norm of all video frames is computed by convolving each frame with first-order derivatives of a Gaussian filter. All frames are registered to the first frame of the video, the reference frame, by means of the fast Fourier transform.

To estimate the sub-pixel translation needed to align the frames, as a first step, we find the peak of the correlation matrix. A window of 5×5 pixels around the peak is then extracted and a two

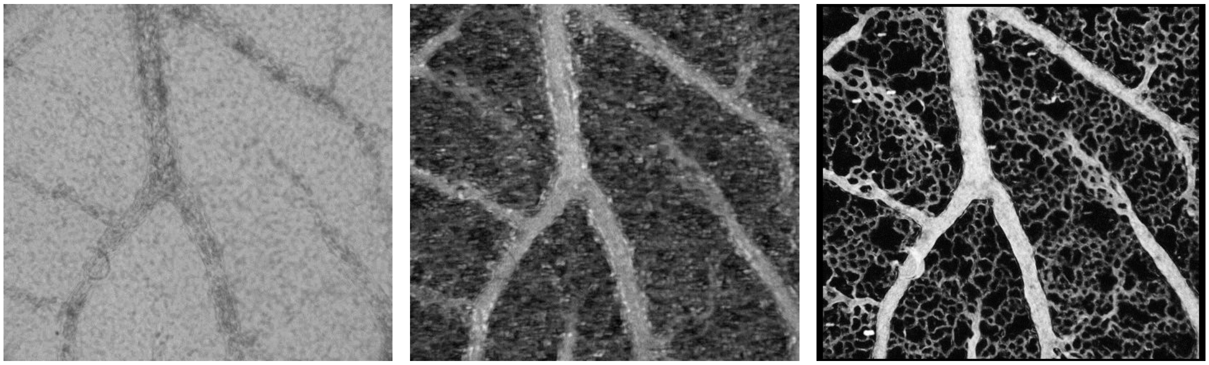

Figure 13: From left to right, a single frame extracted from *in vivo* recordings of chick chorioallantoic membrane, and the standard deviation (SD) image of the unregistered and registered videos, respectively.

dimensional Gaussian function fitted. The maximum of the fitted Gaussian is considered as the new peak and the translation matrix needed to align the two images is computed.

The final registered image is obtained by cubic interpolation. Figure 13 shows the standard deviation image (for each pixel the standard deviation is computed over all frames of the video) of the unregistered and registered videos. As shown, after the registration even the capillary meshes are easily distinguishable, demonstrating the quality of the achieved alignment.

Segmentation

To compute the blood flow velocity in a specific vessel segment, its position must be known. The SD image serves as the basis for blood vessel segmentation. Note that after registration vessels are static for the whole video. Thus the major source of change in time is the movement of the blood cells.

The approach proposed in the previous chapter ("*Blood flow velocity from video recordings*") is used to trace the centerline of all the main vessels. This serves as an initialization step. The precise location of the centerline is of extreme importance due to the laminar nature of the blood flow.

Blood flow velocity varies depending on wall distance, *i.e.*, blood in the center of the vessel moves at maximum velocity which decreases as we get closer to the vessel walls. If the centerline location is not precise, blood flow velocity measurements may be underestimated. Furthermore, it is mandatory

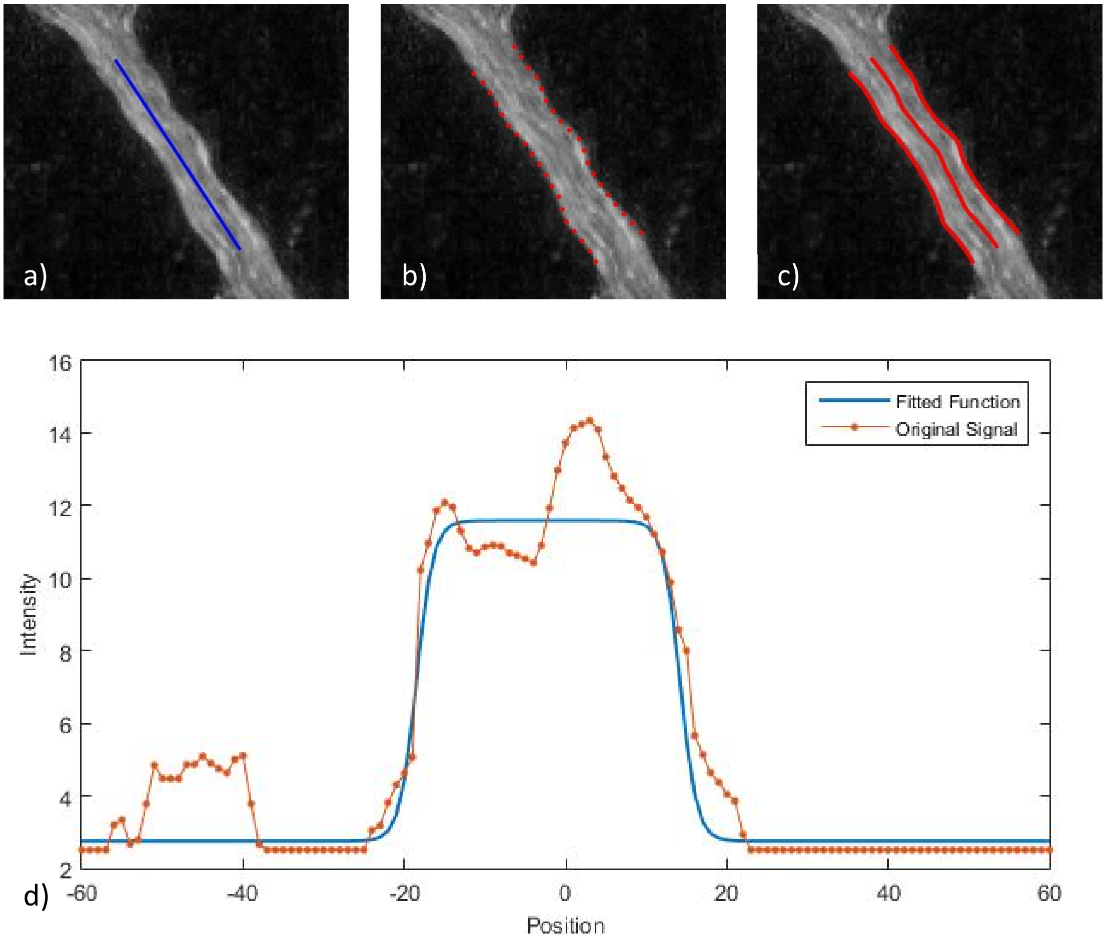

Figure 14: A cropped region of interest of the standard deviation (SD) image [a) b) and c)]. In a) the candidate centerline is shown marked in blue. The resulting candidate border points and final inner vessel limits and centerline are shown marked in red in b) and c), respectively. In d) an example of a single cross-sectional profile and the fitted function are shown.

to estimate the inner diameter of the vessel, as it is required to compute important features such as flow.

Centerlines obtained after skeletonization are corrected as follows:

- At specific length intervals, the orientation of the traced centerline is computed and a cross-sectional normal profile gathered (Figure 14a and d);
- A plateau function is fitted to each cross-sectional profile (Figure 14d);
- From this fitted functions one retrieves candidate border points (Figure 14b);
- Spline curves are fitted to the set of candidate border points to find the inner vessel limits.
- Finally, the centerline is corrected in accordance to the newly computed limits (Figure 14c).

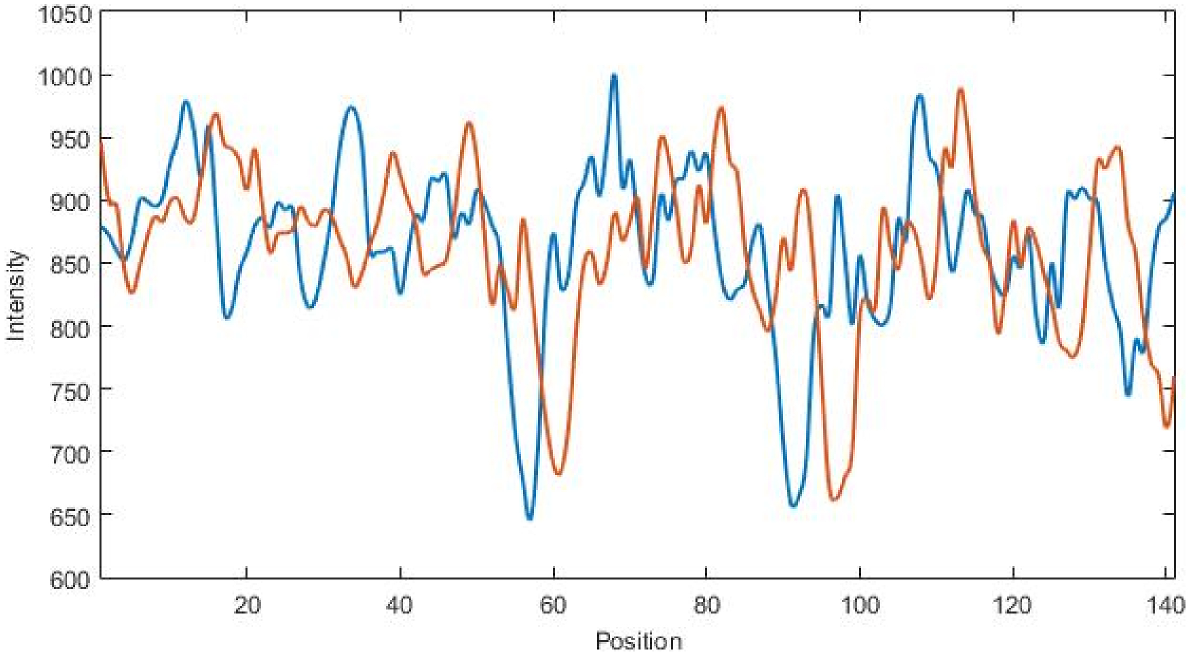

Figure 15: Intensity longitudinal profiles, taken along the vessel’s path, gathered from consecutive frames of the registered video.

Velocity Measurement

The blood cells move along the vessels at a speed proportional to the blood flow velocity [91]. Therefore, the displacement of these cells between two consecutive frames divided by the time delay between captures, is a measurement of flow velocity.

The time delay is extracted from the imported video file and the displacement computed. Typically, blood cells generate a fairly contrasted pattern along the vessel's path. To measure displacement, one possible solution would be to segment and track each individual cell. However, in multi-file flow conditions (more than one red cell on a given cross section through a vessel), individual red cells are difficult to identify and track. Furthermore, this mechanism is labor intensive and time demanding.

In our approach we take advantage of the laminar nature of the blood flow. After the segmentation step, an intensity longitudinal profile, taken along the vessel's path, is gathered from each frame of the registered video. Figure 15 shows an example of such profiles.

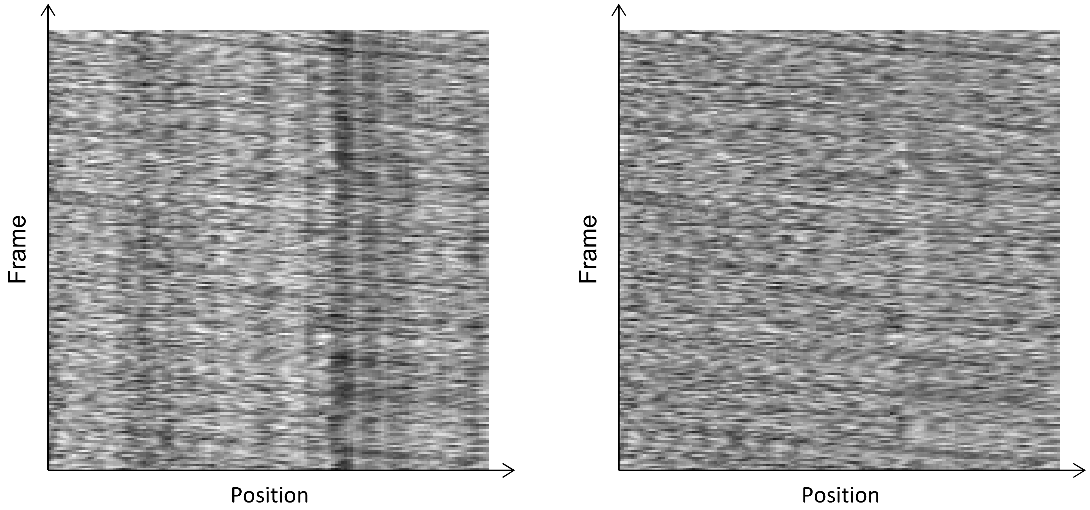

Figure 16: Intensity longitudinal profiles, taken along the vessel's path, before (right) and after (left) the median longitudinal profile is computed and subtracted. As shown, the static component (dark vertical bands) is removed.

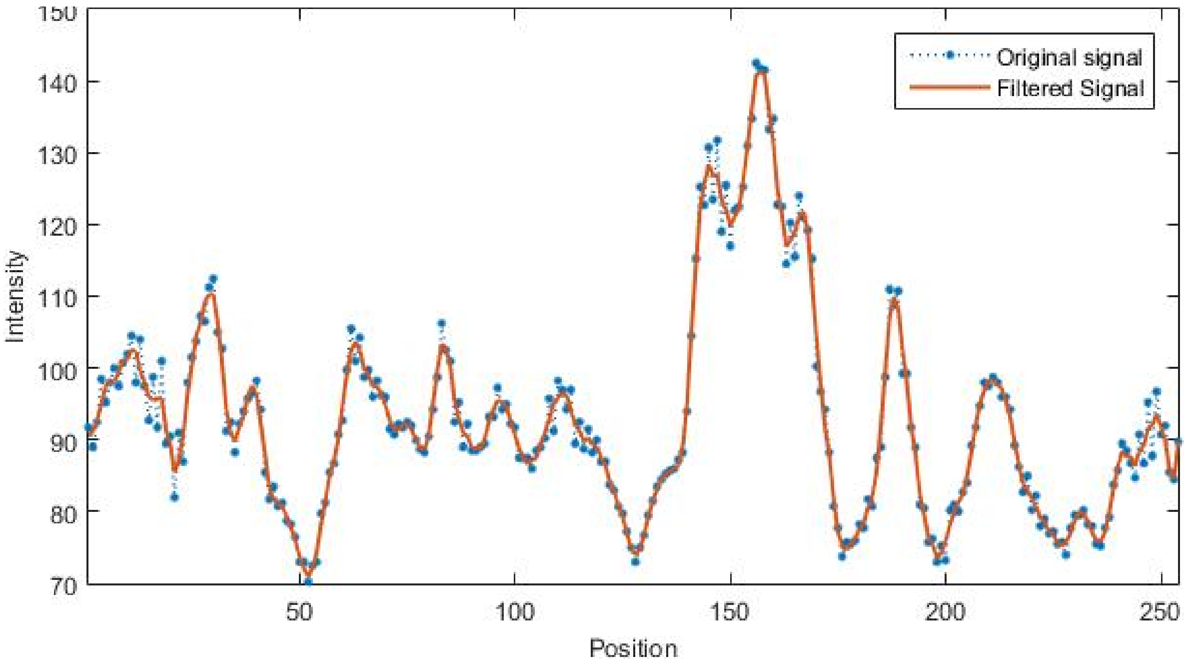

Figure 17: An example of a single intensity longitudinal profile before (blue) and after (orange) Savitzky-Golay filtering.

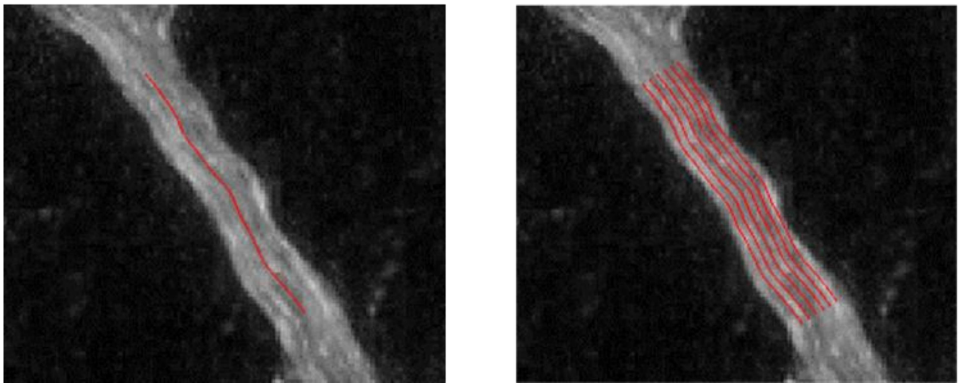

Figure 18: From left to right, marked in red are the profiles for single line and full width modalities, respectively.

The displacement between consecutive longitudinal profiles allows one to compute time dependent velocity changes [91].The displacement is computed as follows:

- Each longitudinal profile contains a static intensity component, generated by the vessel and tissue, and a moving component, the blood cells. The median longitudinal profile is computed and subtracted (Figure 16). This step ensures that the static component does not affect the measurement of the displacement.
- Each profile undergoes Savitzky-Golay filtering to correct for noise and other capture artifacts that may have been introduced in the recording process. This filter is typically used to smooth noisy signals. It is known to perform better than standard moving average filters as they are able to preserve relevant high frequency components [92]. Figure 17 shows an example of the filtered versus unfiltered signal.
- After filtering, the profiles are interpolated using a piecewise polynomial (spline) to allow for sub-pixel displacement measurement.
- The normalized cross-correlation is then computed between consecutive interpolated profiles. The correlation peak position corresponds to the shift between frames.

The user can choose between two different modalities for the computation of blood flow velocity: single line or full width (Figure 18). With the former, a single profile is used at the centerline of the vessel. Blood flow velocity is then computed as described above. For the latter, parallel profiles computed along the vessel's width are used. Velocity is then computed for each profile as described, and displayed in a three dimensional graph. This allows not only time dependent velocity changes, but also transversal flow velocity profiles.

Results

Simulated Data

To quantitatively assess the accuracy of the proposed software, ten different simulations with blood flow velocity set at increasing constant speeds were created. Contrast and background noise conditions were set to simulate typical *in vivo* measurements. Measured blood flow velocity was averaged over a time period of 2 seconds. Obtained results are shown in Figure 19. The software performs as expected matching the set real velocity.

To further evaluate the proposed algorithm three scenarios of increasing difficulty were created:

1. Smooth velocity variation, normal contrast and background noise;
2. Smooth velocity variation, low contrast and high level background noise;
3. High frequency velocity spikes, low contrast and high level background noise.

Contrast and noise level may be inspected in Figure 20: normal contrast and background noise in Figure 19(a) and low contrast and high level background noise in Figure 20b. Set and measured velocity for scenarios 1 to 3 are shown in Figure 20(c), (e), and (g), respectively. Relative error (%) was computed for all the scenarios as the absolute error divided by the set velocity, and is shown in Figure 20(d), (f), and (h) (scenarios 1 to 3, respectively). Computed relative error values were low for every

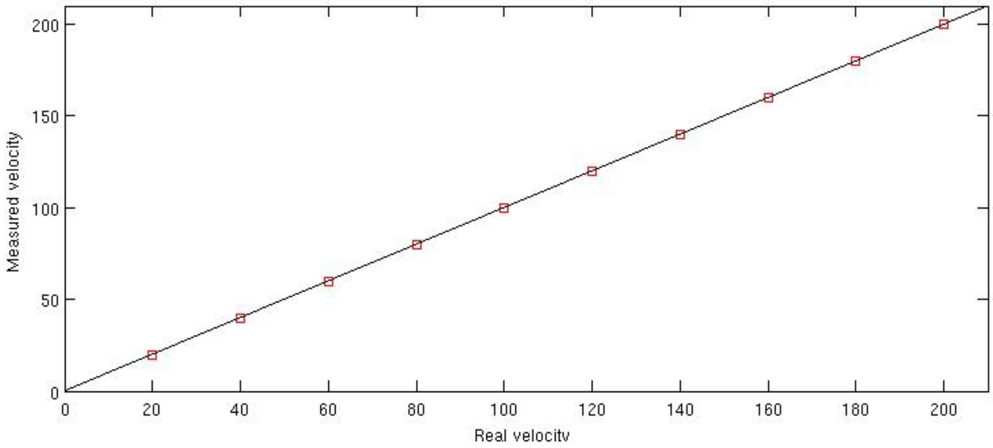

Figure 19: Measured blood flow velocity against set velocity.

scenario (overall maximum of 3.1 %). Average, standard deviation, and maximum absolute errors for each scenario are shown in table 1.

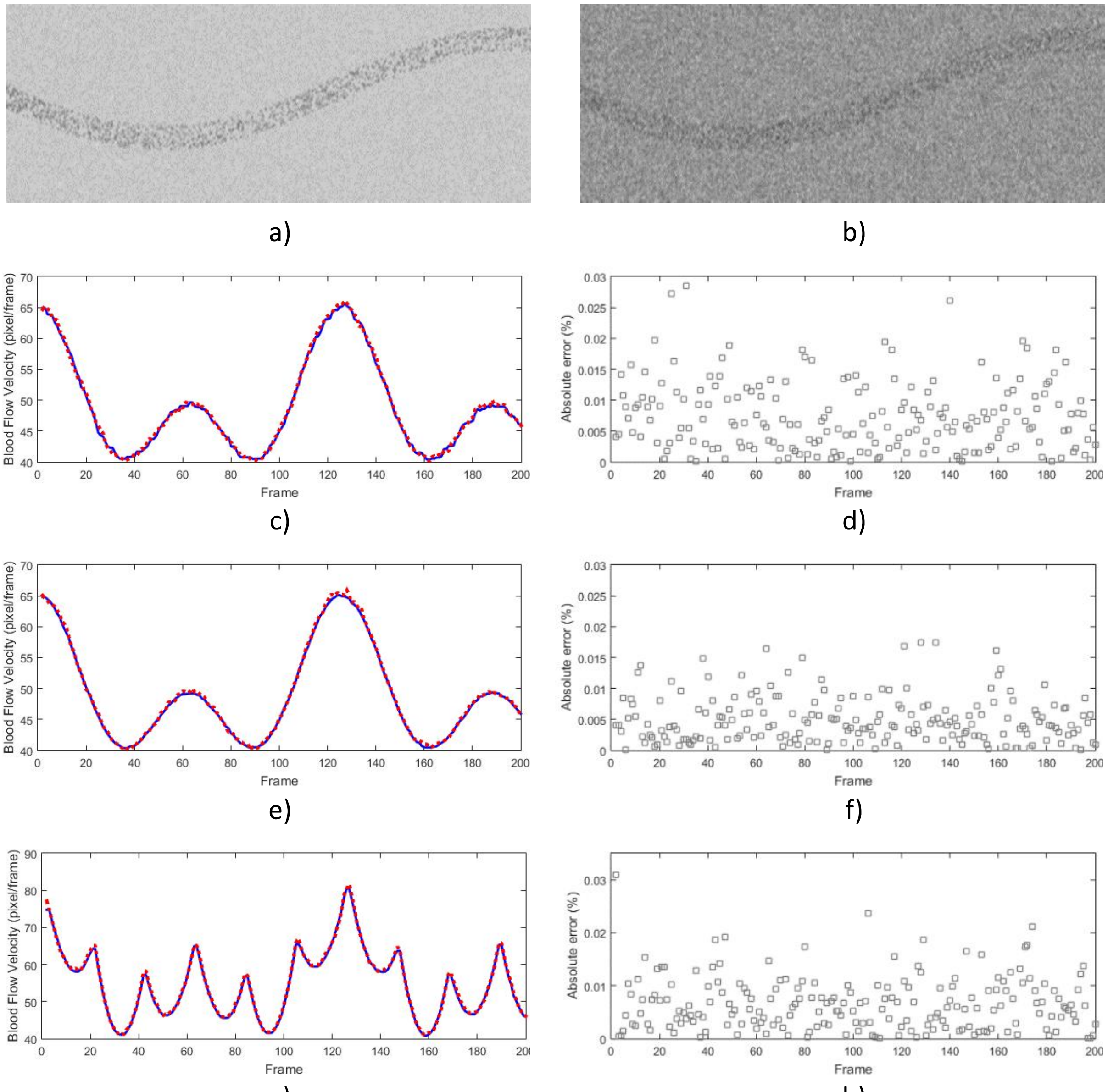

a)

b)

c)

d)

e)

f)

g)

h)

Figure 20: A representative frame extracted from simulated data with: (a) normal contrast low noise level; (b) low contrast, high noise level. Set (blue) and measured velocity (red) for scenarios 1 to 3 in (c), (e), and (g), respectively. Relative error (%) for scenarios 1 to 3 in (d), (f), and (h), respectively.

Table 1: Average, standard deviation and maximum relative errors for each simulation scenario.

Scenario	Relative Error (%)		
	Average	Standard Deviation	Maximum
1	0.50	0.38	1.75
2	0.66	0.56	2.85
3	0.70	0.51	3.10

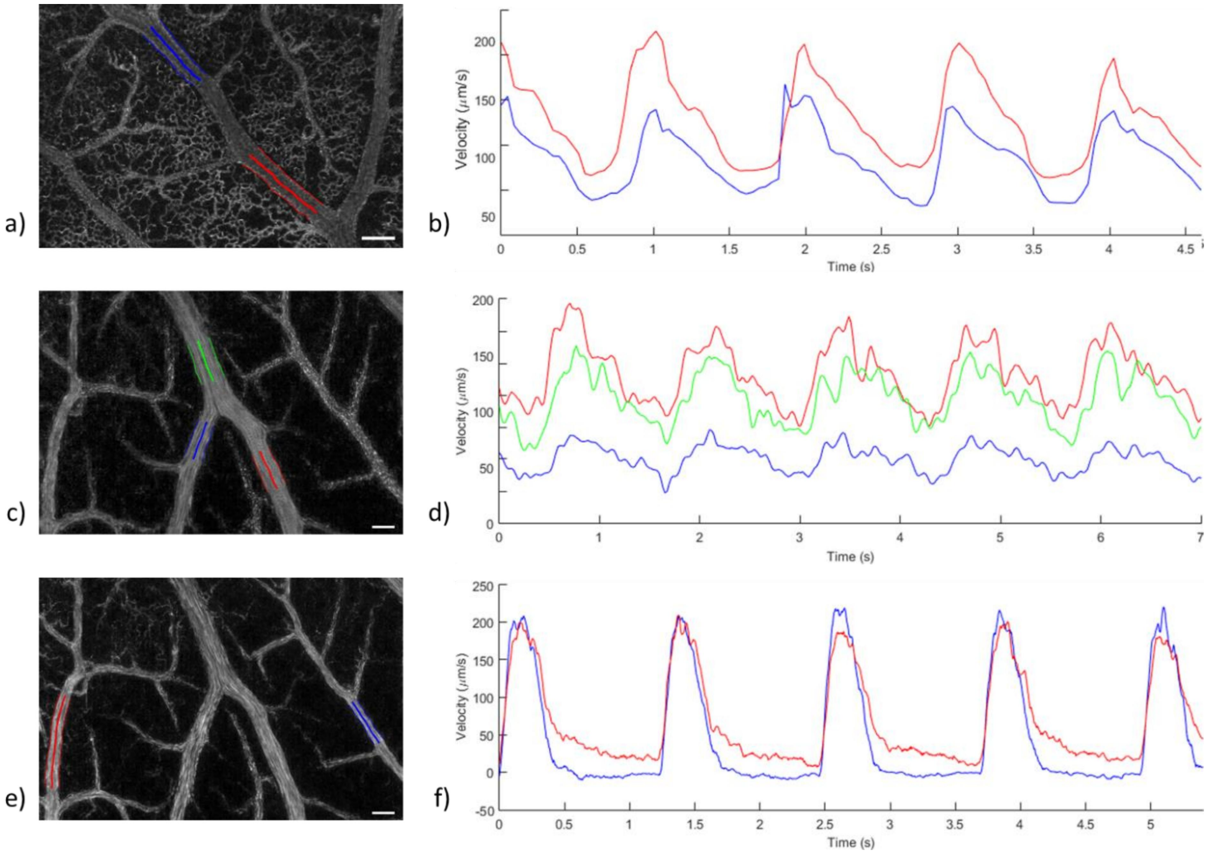

Figure 21: Single line velocity measurement modality. From left to right, standard deviation (SD) image with marked vessel segments and respective time dependent blood flow velocity for: (a) and (b) Sony camera at 25 fps; (c) and (d) MotionBlitz camera at 50 fps; (e) and (f) MotionBlitz camera at 200 fps.

Video Recordings

As aforementioned, CAM videos were used to evaluate the proposed software tool. Two different cameras were applied to test the robustness of the used approach. Both modalities, single line and full width, were tested (Figure 21 and 22, respectively).

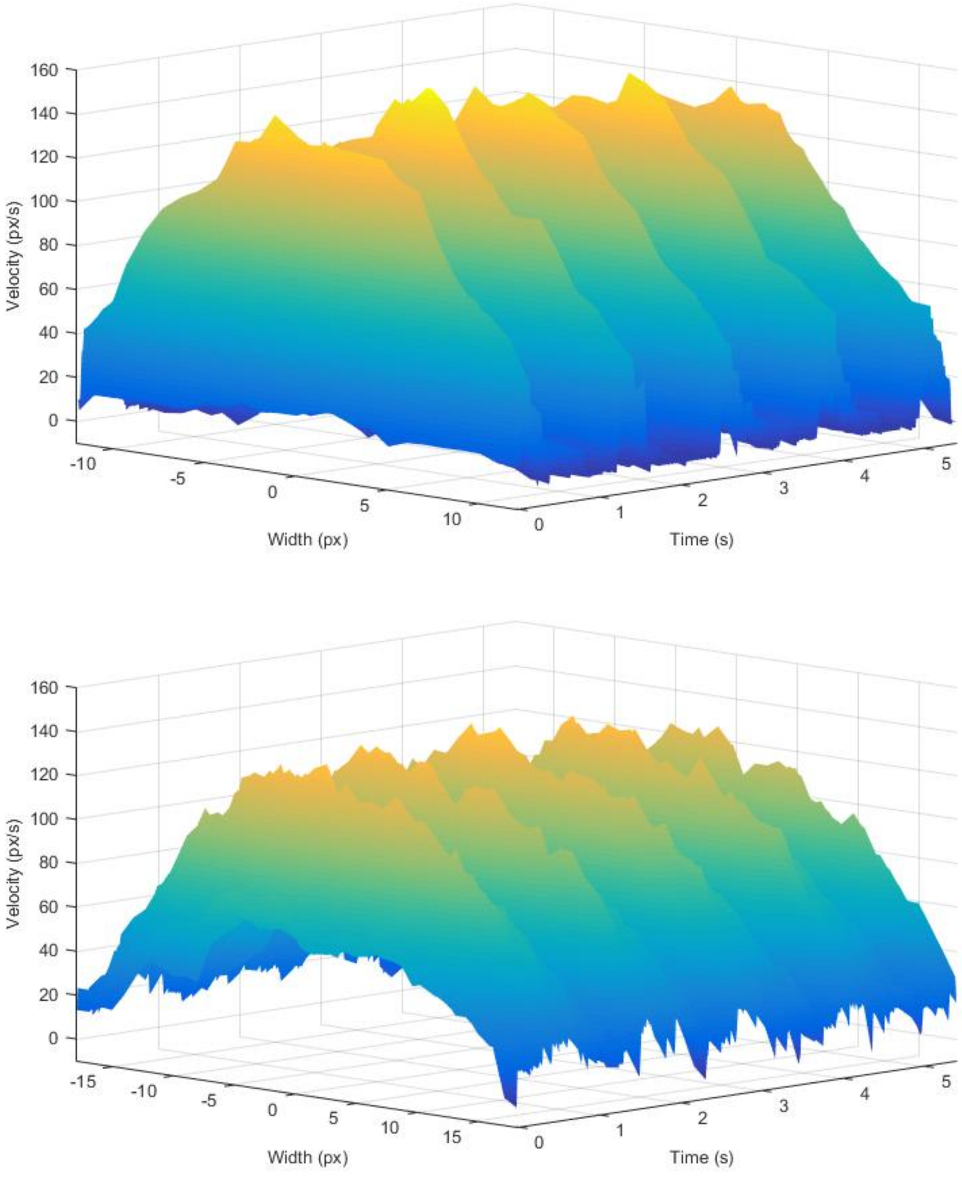

Figure 22: Full width velocity measurement modality. From top to bottom: time dependent blood flow velocity from an artery and a vein segments, respectively.

Figure 21(b) shows the obtained blood flow velocity measurements using the single line modality for two different vein segments (marked in Figure 21a) using video recordings from the Sony camera. The video was recorded at a rate of 25 frames per second (fps). Results show velocity curves typical for a vein, with evident pulsatility.

Figure 21(d) shows blood flow velocity measurements using the single line modality for three different vein segments (marked in Figure 21c) using video recordings from the MotionBlitz camera. The video was recorded at a rate of 50 fps. The higher frame rate allows one to visualize time dependent velocity changes in higher detail. Using the same camera, but now with 200 fps, time dependent velocity was computed (Figure 21f) for two artery segments (marked in Figure 21e). The recorded arterial blood flow velocities are in accordance with earlier experimental recordings [93].

The full vessel width measurement modality enables the cross-sectional analysis of blood flow velocity profiles. Using this modality, blood flow velocity of an artery and a vein segments was computed. Figure 22 shows the obtained results. As expected higher velocity values are achieved in the center of the vessel. As we move from the center towards the vessel walls, pulsatility is less pronounced.

Discussion

The proposed software tool allows the fully-automatic analysis of time dependent blood flow velocity changes from video recodings.

Objective *in vivo* validation of the measured velocities is a difficult task as there is no readily available ground truth. One would have to rely on a second software or technique. Instead, simulated data was used to quantitatively assess the accuracy and robustness of the proposed algorithm. The simulation consisted of blood cells moving along a set vessel path. Simulation behavior replicated real data. Velocity was streamlined, cells closer to center of the vessel moved faster and a stochastic velocity component was added to each individual cell. Properties such as cell contrast, background noise, vessel shape, and velocity curve were able to be independently manipulated. This allowed us to test different scenarios. The ability to control specific parameters is the main advantage against *in vivo* models.

To assess the accuracy of the measured velocities, ten simulations were created with blood cells at different constant speeds. Then, three different scenarios were tested (1 - Smooth velocity variation, normal contrast and background noise; 2 - Smooth velocity variation, low contrast and high level background noise; 3 - High frequency velocity spikes, low contrast and high level background noise). The proposed algorithm performed well in all our tests. A relative error of no more than 3.10% was obtained, despite the very low contrast and high level background noise in scenario 3. These results indicate that the algorithm is reliable and may be applied to *in vivo* data.

The chick CAM is an extraembryonic membrane found in chick eggs that allows the exchange of gasses such as oxygen or carbon dioxide between the developing bird and the air from pores in the egg's shell [88], [94]. As it acts as the chick's lung, it is a highly vascularized structure. Due to its dense capillary network and ease of access, it has become an important model for the study of blood vessel physiology, morphology and hemodynamics [86], [88]. The chick CAM is one of the main *in vivo* models to study the angiogenesis process [86], [88].

Two different cameras were used to capture *in vivo* videos from chick CAM vessels. The proposed software was used to analyze time dependent blood flow velocity from the recorded videos. Furthermore, the full width modality allowed for cross-sectional analysis, *i.e.* the analysis of not only the center blood flow velocity, but also changes with vessel width.

For chick CAM videos, no ground truth was available. Thus, the results can only be visually inspected. All the developed software modules (Registration, Segmentation, and Velocity Measurement) proved adequate to their tasks. The obtained blood flow velocity curves shape and values appear to be as expected. With the full width modality, as expected, blood flow velocity values are higher in the center of the vessel and decrease as one gets closer to the vessel walls. The use of different resolutions, frame rates, and even cameras, showed the robustness and versatility of the proposed software.

The software presented here, has already been used to study collateral remodeling after acute micro-occlusion [89], [95].

In vivo measurements of blood flow velocity could provide novel and/or improved disease markers. In the future, the proposed method may be employed to conjunctiva videos. In this work, we were unable to get these videos. Blood flow velocity software from conjunctiva videos could allow to establish blood flow properties of individuals and detect changes from systemic diseases.

CORNEAL SUBBASAL NERVE PLEXUS

The introduction of confocal microscopy as a tool for the visualization of corneal nerves has revolutionized our understanding of these structures. Confocal microscopy is now the method of choice to visualize corneal nerves in the subbasal nerve plexus. The ability to image these structures *in vivo* in a fast and noninvasive way has markedly boosted our knowledge of corneal nerves anatomy and physiology in healthy and diseased conditions [21], [23], [96], [97].

The basic principle behind this imaging methodology is simple but effective: there is a pinhole at the confocal plane of the lens in order to eliminate out-of-focus light. Typically, there is a second pinhole at confocal plane of the illumination path. The result is an increase in resolution and contrast [98]. Due to the transparency of the cornea, confocal microscopy is an ideal imaging technique to image the subbasal nerve plexus [21], [96]. The inherent optical sectioning capacity of this imaging technique allows one to image the cornea at multiple optical planes.

The typical corneal confocal image as imaged by the popular Heidelberg Retina Tomograph 2 (HRT-II) system with the Rostock Cornea Module (Heidelberg Engineering GmbH, Heidelberg, Germany), covers an area of $400 \times 400\ \mu m^2$. More and more, properties such as corneal nerve density, computed as the corneal nerve fibers length per unit of area, are being used in research and clinical environments [97]. However, single confocal images only cover a very small area (less than 1%) of the central cornea. The validity of extrapolation is uncertain.

Recently, there has been a particular increase of interest in the analysis of mosaics covering a large area. Corneal mosaics can be defined as groups of images that are “stitched” together to create a single image that covers the total imaged area (Figure 23). Although the manual mosaicking of corneal confocal images is an extreme task that may take up tenths of hours [99], fully automatic software has been proposed [100]–[102].

Fully automatic mosaicking and nerve tracing could be the key to novel clinical studies aimed at investigating correlations to diseases. In this chapter we present an algorithm capable of segmenting the corneal nerves from confocal microscopy images and mosaics in a fast and accurate manner. This was then used as a basis to explore the corneal nerve density, an already established disease biomarker, as computed from mosaic images. The obtained results, further demonstrate the feasibility of fully-automatic corneal nerve density analysis from wide-field mosaics. Furthermore, we have looked into the development of novel nerve tortuosity metrics. We were able to improve on existing metric results.

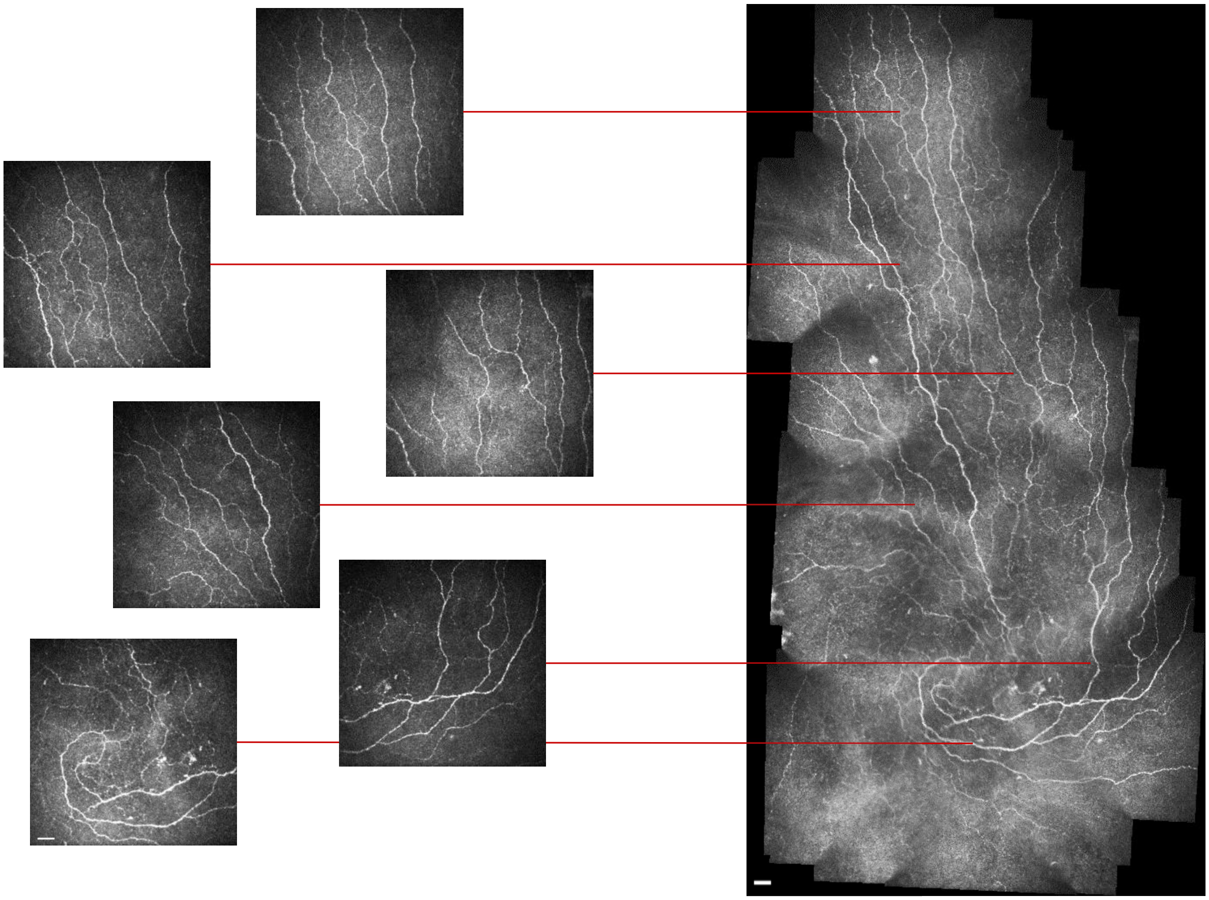

Figure 23: Representative scheme on corneal mosaic images. On the right, multiple single confocal microscopy images. On the left, corneal mosaic. Red lines indicate the position of each single image in the mosaic space. Scale bar: 30 µm

CORNEAL NERVES SEGMENTATION

The quantitative analysis of corneal nerves is still impractical in the daily clinical practice, due to the difficulty and execution time of manual or semi-automatic corneal nerves segmentation. A few automatic approaches have been proposed over the years. Scarpa *et al.* [103], applied a fuzzy c-mean clustering technique to classify each pixel as belonging to a nerve or not. More recently, a new multi-scale dual-model method to detect the corneal nerves was proposed by Dabbah *et al.* [52], while Poletti and Ruggeri [104] proposed a new approach based on a sparse tracking scheme. Ziegler *et al.* [54] used a minimum-error thresholding method in conjunction with log-Gabor filtering to trace corneal nerves from mosaic images. Studies have already shown the application of these fully automatic approaches [105]–[107]. Annunziata *et al.*, in [108], presented a fully automated corneal nerve tortuosity quantification system. For corneal nerves segmentation, the system made use of a hybrid segmentation method combining an appearance with a context model.

One of the main problems of existing corneal segmentation methods is their execution time (up to hundreds of seconds for single images). Recently, there has been a particular increase of interest in the analysis of mosaics covering a large area, instead of single corneal confocal images [53], [106], [109]. However, these larger images are computationally challenging and existing methods cannot cope with them in reasonable time. For instance, Ziegler *et al.* [54] report a running time of almost 27 minutes to process a mosaic image with an area of 2.23 × 106 μm^2. For these reasons, there is the need for a fast and accurate fully automatic approach to nerve tracing.

The method developed and herein described consists of two sequential steps – a thresholding step followed by a supervised classification. For the classification we use a support vector machines (SVM) approach. Initially, a large set of features is computed, which is later reduced using a backward elimination based on segmentation accuracy. To validate the obtained nerve tracings, we evaluated the tracing accuracy and reliability of extracted clinical parameters (specifically, the corneal nerves density and tortuosity).

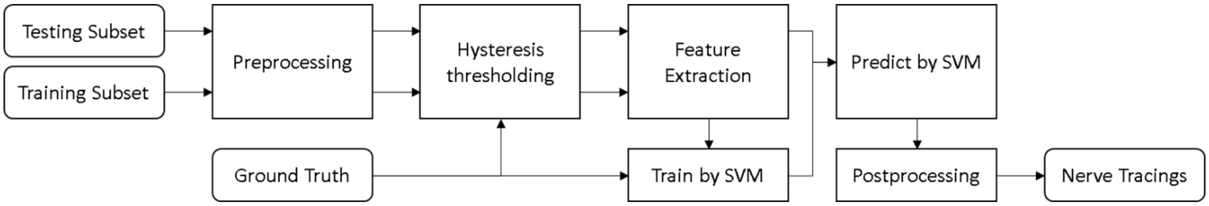

Figure 24: Flowchart representing the global workflow of the algorithm.

Materials and Methods

Throughout this section we describe a novel method for tracing the subbasal plexus nerves from human corneal confocal images and the data used in the validation process. Figure 24 shows the global workflow of the algorithm. Because an automatic approach to nerve tracing must provide accurate tracings and useful clinical parameters, the validation of the proposed algorithm deals with both issues.

Single Image Datasets

To evaluate the algorithm's performance, the nerve tracings obtained by the proposed automatic approach were compared with reference ground-truths. Furthermore, we evaluated the clinical descriptors of nerve tortuosity and density obtained from the automatic approach against manual measurements. Two different databases were used; both of them are described below.

A total of 246 confocal microscopy images of the subbasal corneal nerve plexus of healthy volunteer subjects were acquired using the HRT-II with the Rostock Cornea Module at the Ophthalmology Department in the Linköping University, Sweden. The imaging instrument was outfitted with an Achroplan 363/0.95 NA immersion objective lens (Carl Zeiss SMT GmbH, Oberkochen, Germany) to provide confocal images covering a field of 400 × 400 μm^2 (384 × 384 pixels).

All images from the dataset were segmented manually by two independent clinical graders (G1 and G2), who traced the centerlines of all visible nerves during several sessions over a 2-week period. Both graders used the NeuronJ [110] tracing plugin for ImageJ (available in the public domain at http://www.imagescience.org/meijering/software/neuronj/; version 1.45 s, Rasband, W.S., ImageJ; National Institutes of Health [NIH], Bethesda, MD, USA) over the raw unprocessed images.

The intersection between the tracing of G1 and G2 was used as the ground-truth tracing. For the sake of convenience, this set of images is from now on called database 1 (DB1). This dataset was split randomly into two different subsets, the training (N = 50) and testing (N = 196) subsets.

To evaluate corneal nerve tortuosity, a publicly available database (database 2 [DB2]) was used (available in the public domain at http://bioimlab.dei.unipd.it/, Laboratory of Biomedical Imaging, University of Padova, Italy). The database is composed of a total of 30 confocal images of the subbasal corneal nerve plexus. Images were acquired from healthy (N = 6) and pathologic (N = 24) subjects, using the same protocol as described above. The pathologic group included subjects diagnosed with diabetes mellitus (N = 10), pseudoexfoliation syndrome (N = 8), and keratoconus (N = 6). A grader evaluated the corneal nerves tortuosity of each image into three different classes – *High*, *Mid*, and *Low* tortuosity.

Mosaics

The confocal microscope used before (above described) was used to acquire multiple single images of the subbasal nerve plexus. Raster scanning is achieved by manual x/y translation to sweep the visible area of the nerve plexus. Manual adaptive depth correction is then implemented when the examiner feels visibility or contrast of the nerves is reduced. A total of 26 mosaics were created to test the proposed segmentation algorithm during the development stage. The number of images per mosaic was between 356 and 847 individual raw images.

Mosaicking was performed using an in-house approach, similar to what was proposed in [101]. Shortly, the algorithm attempts to roughly register each possible pair of images. This serves as an initiation step. Translation and rotation are stored (scaling is negligible), and the phase correlation between each pair of registered images serves as a similarity score. A low score means images are very different and probably should not be registered to each other. A high score means images cover a similar area of the cornea, and as so, can be mosaicked. A score matrix with all possible combinations is created.

To create the mosaic, images are registered sequentially. The score matrix is first thresholded to discard week pairings: each value in the matrix is set to 0 if the score is below 0.5. The image with the best connectivity is then selected as a starting image. Connectivity is computed as the line sum over the score matrix. The algorithm then iteratively mosaics all possible images:

- Gather all possible scores between images already in the mosaic (I^{in}), and images not yet in the mosaic (I^{out});
- Select the pairing with the highest score – pair I^{in}-I^{out};
- Crop a mosaic area around I^{in};
- Using the translation and rotation stored values as an initiation, fine register I^{out} to the cropped area (affine transform);
- Evaluate the correlation between registered I^{out} and the cropped area to decide wheter I^{out} can be incorporated in the mosaic;
- If so, merge I^{out} with the mosaic; if not set pair I^{in}-I^{out} score to 0;
- If there is still any pair with a valid score repeat.

No manual ground-truth was created for the mosaic images.

Preprocessing

The cornea is a transparent, spherical structure. Typically, confocal corneal images present illumination artefacts of a low-frequency nature. Furthermore, nerves also may appear dimmed due to focus problems, or even appear and disappear along their path (in and out of the focus plane). Other objects, such as bright elongated structures (e.g., cells), also are normally present and may cause false-positives. For these reasons, image and nerve enhancement are essential steps in the process of recovering the corneal nerve tree. In this work, we resort to top-hat filtering and a bank of log-Gabor filters to correct for the aforementioned issues.

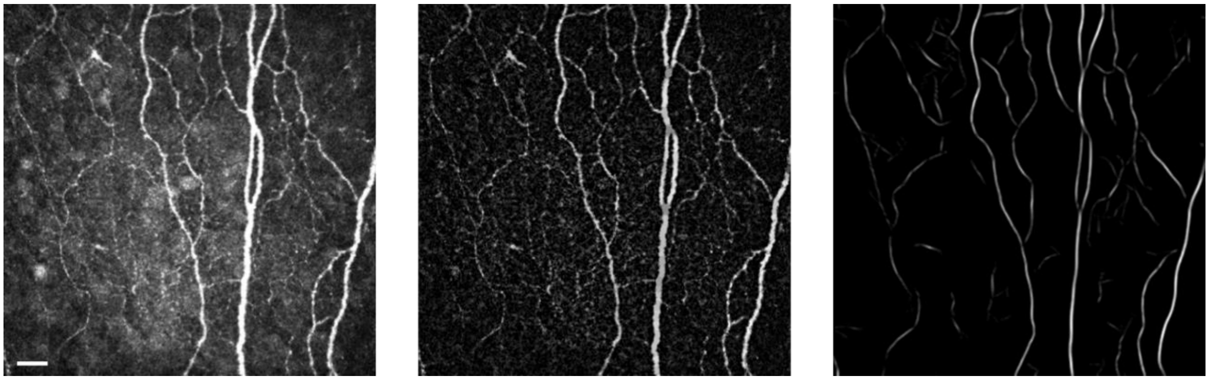

Figure 25: From left to right: original (I^{or}), corrected (I^{TH}), and log-Gabor filtered (I) confocal images, respectively. Scale bar: 30 µm

The original image (I^{or}) undergoes first top-hat filtering. The resulting images (I^{TH}) is then filtered with a bank of 2-D log-Gabor even and odd kernels. These kernels have already been described in the "*Conjunctival Blood Vessel Segmentation*" section. Each value in the final enhanced image (I) is defined as the difference between the even and odd maximal filter responses (I^{even} and I^{odd}, respectively), as

$$I = \left\lfloor \max_{o,n} I_{o,n}^{even} - \max_{o,n} I_{o,n}^{odd} \right\rfloor. \tag{9}$$

Figure 25 shows the results of the preprocessing step. As shown, this procedure normalizes the luminosity and greatly improves the contrast of corneal nerves against background.

Nerve Recognition

The recognition of the corneal nerves in the enhanced images is performed in two sequential steps: (1) image I is thresholded to obtain candidate nerve segments, which then (2) are classified using a supervised classifier. The rationale behind these two steps is to minimize computing time while still aiming at high accuracy.

First, we apply a hysteresis threshold – a popular method for edge detection. The centerline of each resulting thresholded region is considered as a nerve segment. In this way, we obtained candidate nerve segments, which corresponded to linear structures that could be found in the image, but that may or may not be nerves. To distinguish between true or false nerve segments, these were classified using a SVM approach.

Support vector machines classification is a widely used supervised-learning method, extensively described in the literature [111].In this work, we resorted to a C-support vector classification with a radial–basis–function kernel.

The best SVM model and parameters are derived from training. A large set of features is computed to be used by the classification algorithm. The final feature set was selected using a backward elimination approach, based on the accuracy of the segmentation. This set is described below. Two groups of features can be distinguished, morphologic and intensity-based features.

Morphologic features are extracted directly from the binary image, and are related to the shape and size of the candidate nerve segment. The final morphologic features included are the cumulative distance along the segment's path (Length) and the total number of pixels (Area).

Intensity-based features are computed using filters applied to the confocal images. The features are computed as the average and standard deviation intensity values along each candidate nerve segment's path. The final intensity-based feature set comprises:

- Average and standard deviation of I^{or}, I^{TH}, I, and I^{even};
- Average of I^{odd};
- Average and standard deviation of the Laplacian of Gaussian (I^{LoG}) and of the gradient magnitude (I^{G}).

The Laplacian of Gaussian (LoG) filter is a commonly used edge detector. It is computed as the Laplacian of a low-pass filtered image (Gaussian). In this work, a multiscale approach was used by convoluting image $I^{TH}$with several Gaussian filters with different standard deviations. Similarly, the gradient magnitude also was computed at multiple scales as the norm of the gradient of a Gaussian lowpass filtered image I^{TH}. For each of these features, the maximum value across scales weighted by the respective standard deviation of the used Gaussian filters then is selected to obtain $I^{LoG}$and I^{G}, respectively.

The SVM classifier was trained using the training subset from DB1 with the ground-truths as reference. The obtained SVM model was used for all the tests.

Postprocessing

After nerve recognition by classification, some nerve segments appear disconnected from the main nerve tree. This artifact is one of the disadvantages of the chosen enhancement method (log-Gabor filtering). To correct this issue, as a postprocessing step, these segments are connected over small gaps. This step is especially important if one aims to compute clinical parameters, such as tortuosity. For the connection, only the distance, angle, and intensity along the connection path between the two candidates are considered. Dijkstra's shortest path is then used to decide whether the segments should be connected. Although this is a simple approach, our tests revealed that the accuracy gain obtained by more complex methodologies does not compensate for the additional computational time required.

Results

As aforementioned, an automatic approach to nerve tracing must provide an accurate and robust nerve segmentation, but also reliable and useful clinical parameters. The validation of the proposed approach considers both these issues.

Nerve Tracing

To evaluate the system performance, the obtained nerve tracings were compared to the reference ground-truths for the testing subset of DB1. Nerve tracings are compared pixel by pixel to the respective reference ground-truth. However, the graders were asked to trace the centerlines of the nerves. As so, it is unlikely that different specialists chose exactly the same path to trace a given nerve. For this reason, a tolerance must be set. A true positive is considered as such, only if it is within three-pixels from the reference ground-truth. Sensitivity (Sen) and false discovery rate (FDR) were then computed as

$$Sen = \frac{TP}{TP + FN}$$
$$FDR = \frac{FP}{TP + FN} \tag{10}$$

where TP, FP, and FN are the number of true positives, false positives, and false negatives, respectively. *Sen* gives the proportion of correctly identified nerves (the higher the better), while FDR the proportion of nerves wrongly identified as such (the lower the better). As in a typical image, the vast majority of pixels do not belong to corneal nerves, specificity does not provide useful information.

To allow the comparison to previous approaches, the algorithm proposed by Scarpa *et al.* [103] was also applied to the testing subset and compared with the reference ground-truths. Furthermore, G1 and G2 tracings were also compared between them to establish inter-grader variability.

Table 2: Sensitivity (Sen) and false discovery rate (FDR) results (average ± standard deviation, N = 196).

	Sen	FDR
Proposed	0.89 ± 0.07	0.08 ± 0.07
Scarpa *et al.* [103]	0.89 ± 0.06	0.14 ± 0.07
Inter-grader	0.92 ± 0.05	0.08 ± 0.05

Table 2 shows the obtained results. Differences between the different tracing approaches were investigated using Student's t-test. Figure 26 shows some examples for visual inspection.

Regarding the sensitivity, when compared to the inter-grader variability, both the proposed approach and the approach by Scarpa *et al.* [103] achieve a significantly lower value ($p < 0.0001$). No significant differences were found between the two automatic approaches ($p >> 0.05$). As for the FDR, the proposed approach is not significantly different from a human grader ($p >> 0.05$). On the other hand, the approach by Scarpa *et al.* [103] achieves a FDR significantly higher ($p < 0.0001$) when compared to a human grader or the proposed approach.

The time required to analyze a single image, using a single core MATLAB® implementation, was 0.61 ± 0.07 seconds on an Intel® Core™ i7-4770 CPU at 3.4 GHz. Using the same computer, the approach by Scarpa *et al.* [103] requires 145.56 ± 26.42 seconds.

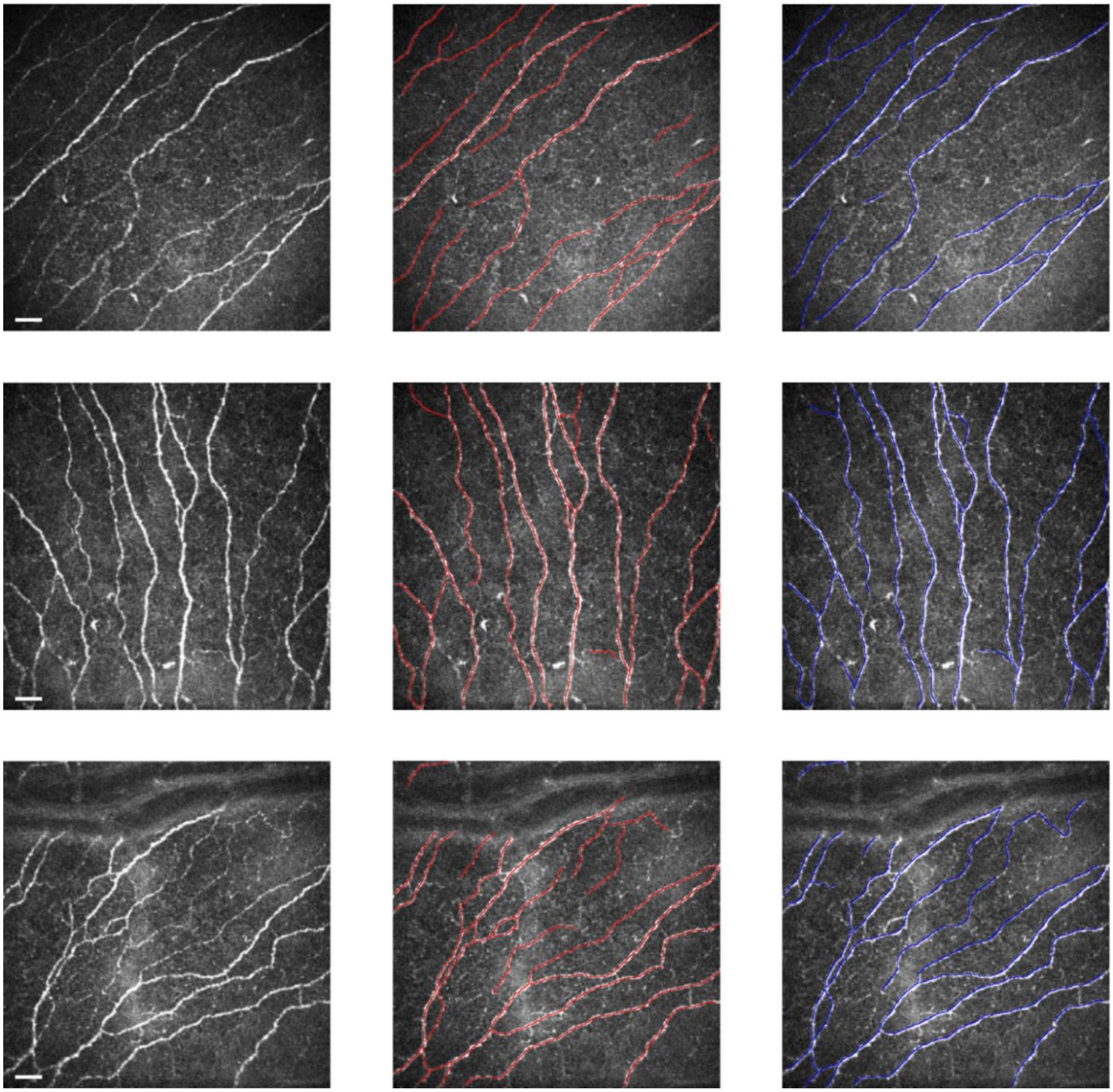

Figure 26: From left to right: original corneal confocal images, automatic tracing (in red), and ground-truth reference (in blue), respectively, for three representative images. Scale bar equals 30 µm.

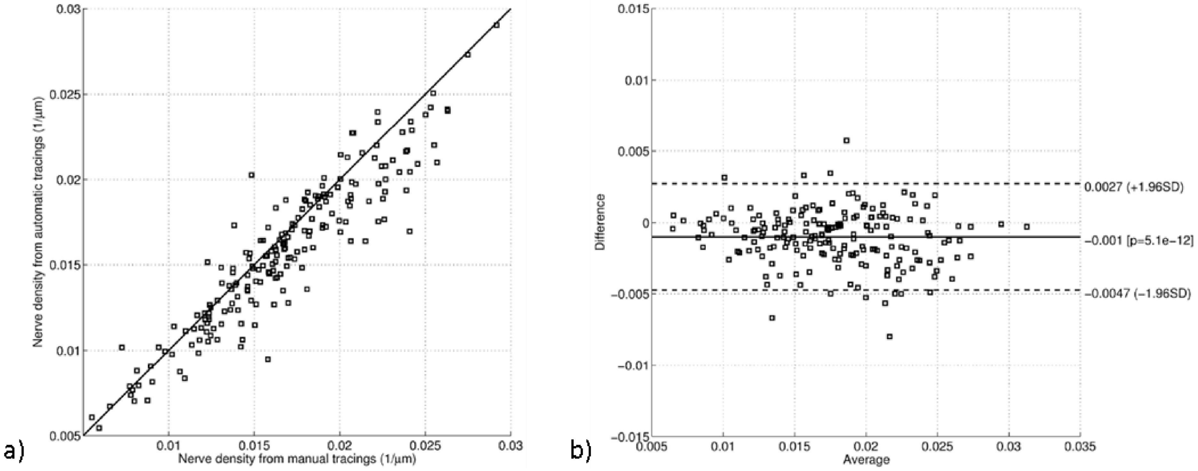

Figure 27: Corneal nerve density (N = 196): (a) automatic against manual tracings; (b) Bland-Altman plot.

Nerve density

Corneal nerve density (the cumulative length of the sub-basal nerves per unit of area of the cornea) was computed for the automatic and ground-truth tracings of the testing subset of DB1. This measure is an important clinical parameter to evaluate the cornea health status.

Figure 27(a) shows the nerve density computed from the automatic tracings against the one computed from the ground-truth (manual) tracings. The obtained agreement in the resulting subbasal nerve density between manual and automated segmentation methods is strong. The correlation coefficient between the two is 0.93 ($p < 0.0001$).

Figure 27(b) shows the Bland-Altman plot of the same results. The average difference between manual and automatic methods was -0.001 $\mu m/\mu m^2$ and Bland-Altman 95% limits of agreement were ± 0.0037 $\mu m/\mu m^2$ around the mean.

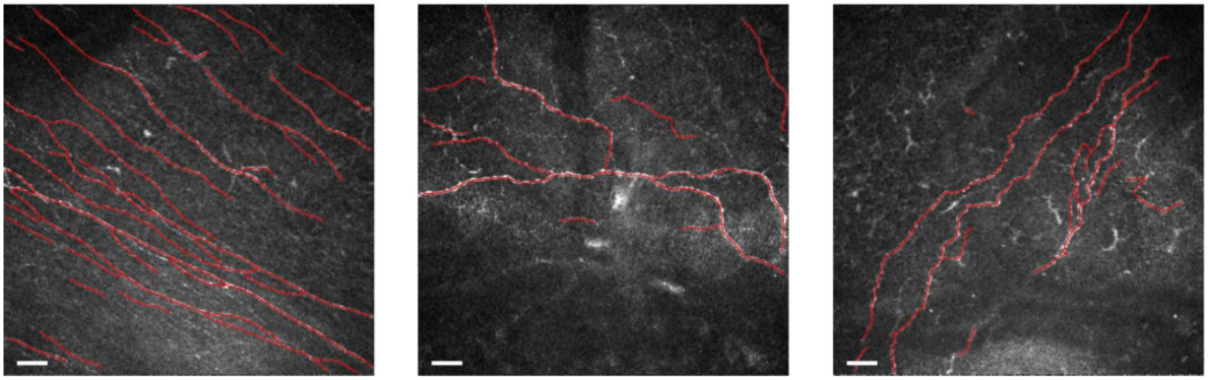

Figure 28: From left to right: automatic tracing (in red) of Low, Mid and High tortuosity images (as classified by the expert grader), respectively. Scale bar equals 30 μm.

Tortuosity

Corneal nerve tortuosity is an important feature of corneal nerves. To investigate the clinical usefulness of the proposed algorithm, it is essential to evaluate nerve tortuosity as computed from the automatic segmentation. The tortuosity was evaluated on the DB2 set of 30 images. First, the corneal nerves were traced for each image using the proposed algorithm. Then, corneal nerve tortuosity was computed as proposed in [112]. Shortly, each nerve segment s is divided into smaller sub-segments called "*turn curves*". A "*turn curve*" is a portion of the segment located between two consecutive twists, *i.e.*, between changes in the curvature sign. As so, each nerve segment is partitioned into n sub-segments s_i as: $s = s_1 \oplus s_2 \oplus \ldots \oplus s_n$. The tortuosity index TI for a given nerve segment s_j is then computed as:

$$TI = \frac{m-1}{m} \sum_{1}^{m} \left(\frac{L_c^{s_j}}{L^{s_j}} - 1 \right), \tag{11}$$

where L^{s_j} and $L_c^{s_j}$ are the curve length (cumulative Euclidean distance over the segment's path) and chord length (Euclidean distance between the first and last point) of segment s_j, respectively.

Figure 28, shows a sample image for each tortuosity class. Marked in these images are the automatically traced corneal nerves. Figure 29 shows the resulting corneal nerve tortuosity against the grader tortuosity classes – *High*, *Mid* and *Low* tortuosity. A Spearman's rank correlation coefficient

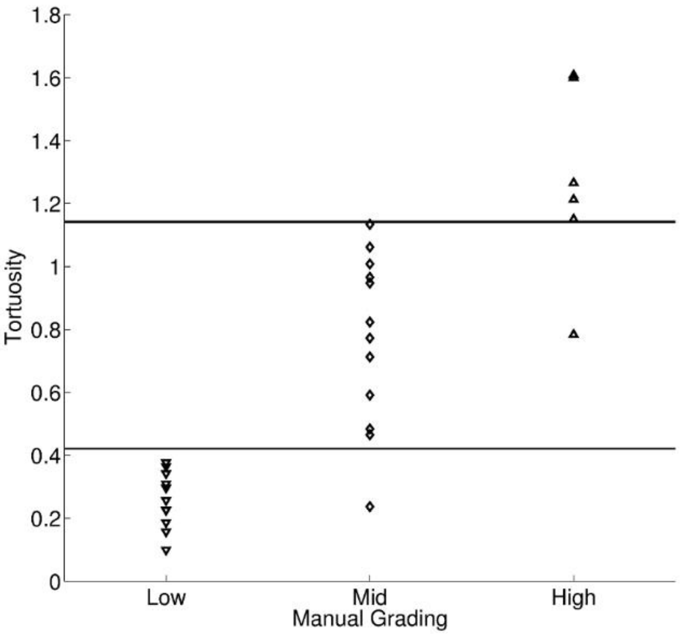

Figure 29: Automatic tortuosity values against its manual grading into three tortuosity classes – *High*, *Mid* and *Low* tortuosity (N = 30).

of 0.95 is achieved ($p<0.0001$). If one sets two thresholds to distinguish between the three classes (as shown in Figure 29), 28 out of the 30 images would be correctly classified (93.3%).

Mosaics

No changes were made to the tracing algorithm to adapt it for mosaic images. No quantitative validation was done for mosaic images. Visually, the algorithm was capable of tracing most visible nerves. Figure 30 shows two examples of obtained mosaic automatic nerve segmentation.

The execution time to trace each mosaic is in general directly proportional to its area. As an example, the proposed algorithm took 32.2 s for a mosaic with a total area of 4.9×10^6 μm^2 (or 30.6 times the area of a conventional single image). Using the above described computer, the time required to analyze each mosaic ranged between 8 and 40 seconds.

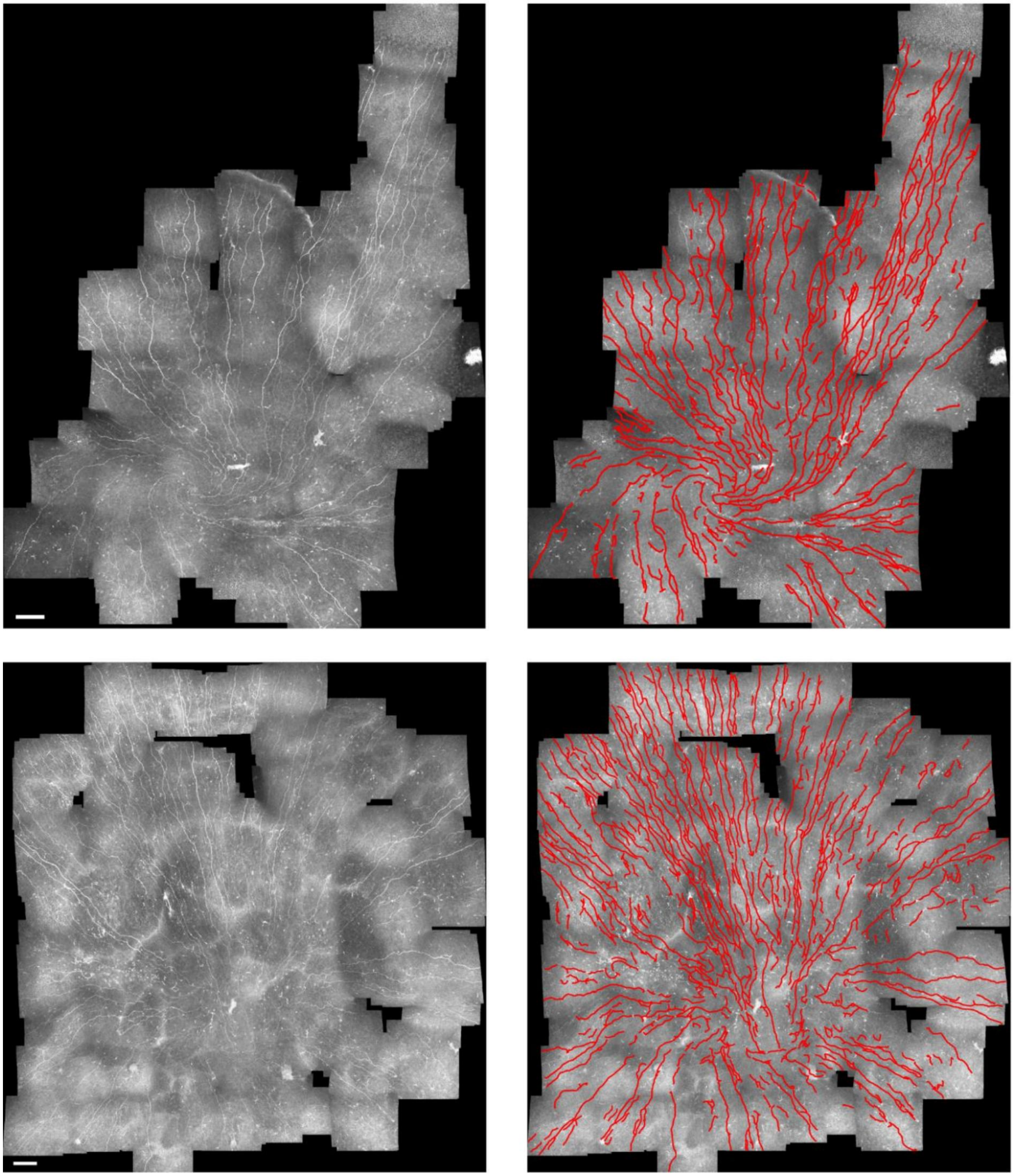

Figure 30: From left to right: original corneal mosaic images and automated nerve tracing (in red). Scale bar equals 120 µm.

Discussion

The use of confocal microscopy to image the human cornea has led to a revolution in the diagnosis and monitoring of this important structure. Furthermore, several studies have shown that the cornea may be regarded as a window to the study of some systemic diseases, such as diabetic neuropathy [21], [23], [46], [51], [52].

The analysis of the corneal nerves seems to be pivotal in these studies. However, the availability of manual or semiautomatic analysis limits the widespread use of this technique. Therefore, a fully automatic robust algorithm, capable of tracing nerves from confocal microscopy images of the subbasal corneal nerve plexus is needed, as it can provide robust corneal nerve descriptors, such as nerve density or tortuosity, and consequently the possibility of an improved diagnosis.

The proposed algorithm proved capable to correctly trace almost 90 % of the corneal nerves. When compared to the approach by Scarpa *et al.* [103], the proposed approach achieves better results (similar Sen, lower FDR). Furthermore, the FDR level achieved by the proposed approach is comparable to a human grader. However, the proposed approach is still significantly less sensitive. These results were achieved with an execution time of only 0.61 ± 0.07 seconds per image (compared to the 145.56 ± 26.42 seconds per image of the previous approach).

Dabbah *et al.* [52] also proposed an automatic classification system to detect nerve fibers in corneal confocal microscopy images. In their study, they reported an average sensitivity of 0.85 (against 0.89 obtained by the herein proposed approach). Although the images were captured with the same system, the datasets are different, and as such, the results are not directly comparable. Algorithm's run time was not reported. Dehghani *et al.* [105], using the same tracing software as Dabbah *et al.* [52], compared diabetic neuropathy detection rates between manual, semiautomated, and automated methods. They showed that the fully automated approach was comparable to the manual and semiautomated ones [105]. The average run time reported to obtain corneal nerve fiber length for a single image was 13 ± 2 seconds. Ziegler *et al.* [54] reported no validation results for the automatic nerve tracing. Annunziata *et al.* [108] only reports graphical results for the precision-recall curve. The average run time reported for segmenting a single image was about 30 seconds

The achieved quality and processing time of the proposed approach to trace the corneal nerves appeared adequate for the possible application of this technique to clinical practice.

The clinical usefulness of the proposed method was also assessed. The clinical parameters of nerve density and tortuosity of the corneal nerves were evaluated. For both parameters the proposed approach performed well. The nerve density computed from the automatic tracings was highly correlated with the one computed from the manual ones. Regarding tortuosity, approximately 93 % of the cases were classified correctly, compared to the manual grading. A high correlation to the rank also was achieved.

In the future, we believe that corneal mosaics will become more and more common in clinical settings. These composed images may greatly enhance the information on disease progression, as they allowed us to study complete nerve patterns and take global metrics. If manual tracing of corneal nerves from an image with 400×400 μm^2 (384×384 pixels) is difficult, performing this task in a large mosaic image is nearly impossible.

The proposed algorithm was also applied successfully to segment mosaic images of the cornea, with run times in the order of tens of seconds. This means that one can trace the corneal nerves in a very short time and as such enable the automatic and objective analysis of these images.

Previous methods, although capable of tracing corneal nerves, had as a main setback their execution time. Fully automated corneal nerve tracing algorithms have been previously applied successfully to cornea mosaics [53], [106]. The reported running time was of tens of minutes [53].

The corneal nerve segmentation algorithm presented here, has also been successfully adapted to study corneal nerve density thy1-YFP mice with induced diabetes [113].

The herein obtained results show the clinical applicability of the proposed approach for automatic nerve tracing and clinical parameter estimation.

CORNEAL NERVES DENSITY ESTIMATION: APPLICATION TO MOSAIC IMAGES

Several studies have shown that the density of the subbasal corneal nerves, quantified from confocal microscopic images, may be used to detect and monitor peripheral nerve degeneration [57], [114], [115]. Indeed, corneal nerve density is already an established biomarker of disease. It has been linked to a number of ocular and systemic diseases such as amyotrophic lateral sclerosis [56], diabetic neuropathy [46], [52]–[54], or Parkinson's disease [57].

The clinical assessment of this disease marker is still challenging and lacks standardization. Despite being the most used and matured corneal biomarker, the corneal nerve density computation is still prone to errors or bias.

So far, most studies have only relied on single confocal images to establish correlation to diseases [116]. The introduction of corneal mosaics together with a fully automatic nerve segmentation algorithm could be a stepping stone into improved correlation to diseases.

As aforementioned, confocal microscopy only provides images from a very small region of the cornea. Using a single image to extrapolate corneal nerve density can lead to errors. To mitigate this, more than one image, from different regions of the cornea, are sometimes used [116]. Since there is no guaranty of coverage, this approach is still prone to selection bias. Furthermore, reproducibility is low. Thus, nerve density analysis over time is unreliable and disease monitoring difficult.

In this section, we explore the corneal nerve density computed from mosaic images. One of the obstacles to the full wide spread usage of corneal mosaics to analyze nerve density of the subbasal plexus, is the time required to trace corneal nerves from these images. Because, the fully automatic segmentation algorithm proposed in the previous section ("*Corneal Nerves Segmentation*") was used, processing time was not an issue. All visible corneal nerves from a dataset of mosaic images were traced, and the automatic nerve density was compared to a manual approach for validation purposes. Mosaic nerve density was then compared to the nerve density computed from the combination of multiple single images.

Materials and Methods

Materials

A total of 160 mosaics from 82 subjects were used in this study. The study population consisted of both normal (N=43) and type 2 diabetic subjects (N=39). All participants were included as part of the Västerbotten Intervention Programme, a large population-based study in a Northern Swedish county. The full characterization of the study population is described in detail in [117], [118], and [99].

For all the subjects, multiple confocal microscopy images of the subbasal corneal nerve plexus of both eyes were acquired using the Heidelberg Retina Tomograph 3 (HRT-III; Heidelberg Engineering GmbH, Heidelberg, Germany) with the Rostock Cornea Module to provide images covering a field of 400 × 400 μm^2 (384 × 384 pixels).

An adaptive method was used to combine manual raster translation of the field-of-view and real-time axial depth correction, as described in [99]. This allowed the acquisition of full 3D confocal image stacks that are then used to create depth-corrected wide-area mosaics.

The mosaicking was not performed by our group. The method used was based on an approach reported previously [100], [102], [119]. Some minor changes were introduced to accommodate how the individual raw images were acquired. These are described in [99].

Manual versus Automatic Nerve Segmentation

To validate the automatic nerve density computed from mosaic images, the computed nerve density was obtained and compared with a ground-truth. Pearson correlation was used.

All mosaic images were segmented manually by an experienced observer, who traced the centerlines of all visible nerves using the NeuronJ tracing plugin for ImageJ. A second independent experienced observer checked the obtained tracings for consistency and accuracy. All abnormalities and missed nerves were corrected.

The approach presented in the "*Corneal Nerves Segmentation*" section was used to automatically segment the corneal nerves from all mosaic images.

The length of all traced segments (both automatically and manually) and image area were then determined and the nerve density computed (the ratio between the cumulative length of all the traced nerves and the total area covered by the mosaic image).

To avoid nerve density underestimation due to *out-of-layer* artifacts (in some mosaic edges, no nerves are visible due to partial oblique imaging of the corneal epithelium or Bowman's layer), the mosaic area determined and used for nerve density computation, did not include these regions (for both manual and automatic methods).

Inferocentral Whorl Region Analysis

In previous studies, it has been suggested that the inferocentral whorl region may be primarily affected by nerve degeneration and that prime information towards diagnostics may be obtained by selectively analyzing this region. In this work, some features regarding the nerve density of this region were explored.

In 2010, Marfurt *et al.* visually described the subbasal nerve plexus like a spiral/vortex pattern of long and diverging subbasal nerve fibers that originate from an imaginary center that is located in the inferocentral region of the corneal apex [22]. This phenomenon is known as the inferocentral whorl. This characteristic region was identifiable in 123 mosaics. The center of the whorl was located manually by an experienced observer (Figure 31a).

The nerve distribution around the whorl region was analyzed according to angle and distance from its center. To isolate the whorl region in the plexus and analyze nerve distribution according to distance, the whorl center was used to create concentric rings with 200, 300, 400, 500, 600, 700 and 800 µm of diameter (Figure 31b).

If a given ring contained a non-imaged cornea area, *i.e.* if no data was available for part of the ring, it was excluded. Nerve density for each mosaic image within each of these circular regions was computed and subsequently compared to mosaic nerve density. The density outside the 800 µm ring was also computed.

The nerve distribution with respect to direction was also analyzed within the whorl region. A ring with 800 μm of diameter centered at the whorl center was created. A region corresponding to a 45° arc was then defined. Nerve density within this area was computed. The arc was then rotated 12°. The process was repeated incrementally until a full rotation was completed. Nerve density was computed for each rotation. In the end the direction of maximum and minimum nerve density was computed. Figure 31(c) and (d) exemplify this method.

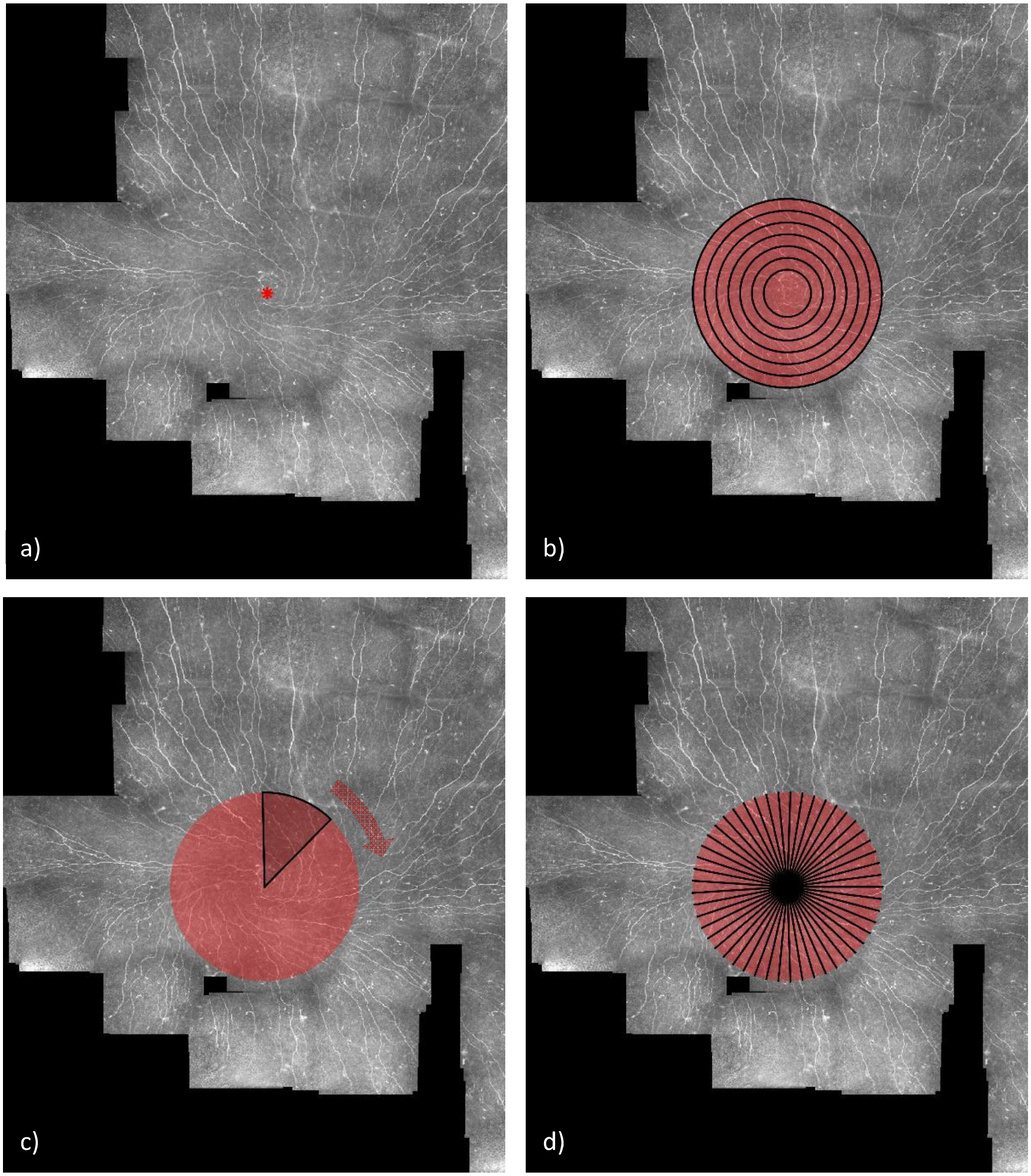

Figure 31: Inferocentral whorl analysis: (a) Characteristic whorl pattern. The center of the whorl as detected by an expert is marked in red. (b) Concentric rings with 200 to 800 μm of diameter, in 100 μm. (c) Within the 800 μm ring, a 45° arc was determined. This arc was subsequently rotated (c) in 12° increments until a full rotation is achieved (d).

Single Image versus Mosaic Analysis

It is assumed that, since mosaic images cover a much larger corneal area, corneal nerve density analysis based on mosaics is preferable to single confocal images. However, it is still unclear to which degree this may affect the obtained results. Furthermore, in previous studies, multiple single images from each subject have been used in order to negate this problem. In this work, the nerve density from both single and combinations of multiple images was compared to mosaic nerve density.

The comparison was performed for two scenarios:

1. Optimal depth-correction – non-overlapping 400 x 400 μm^2 single images were cropped directly from the mosaic itself;
2. Non-depth-corrected images – non-overlapping single 400 x 400 μm^2 raw images from the same position as images in scenario 1 (Figure 32). Because these are not cropped from the mosaic itself, no depth-correction was applied.

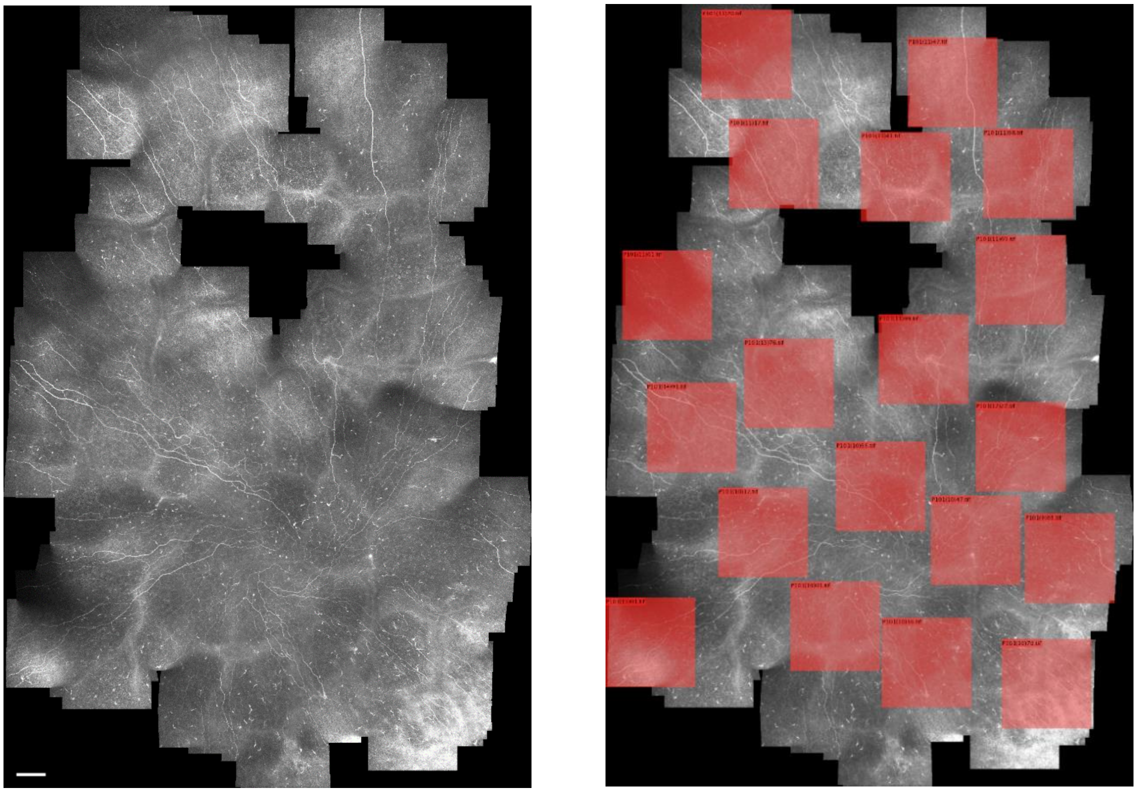

Figure 32: Up to 20 non-overlapping images were selected for each mosaic: marked in red (right) are actual locations of images selected. Scale bar: 120 µm

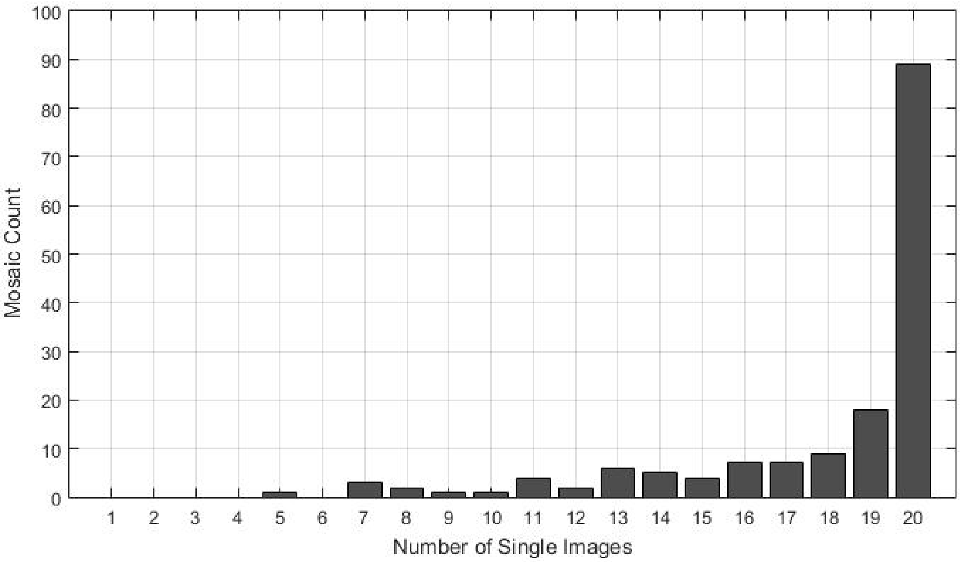

Figure 33: Distribution of number of selected non-overlapping images against number of mosaics containing that number of images (N=160).

Although both cropped and raw images are from the same position, due to rotation and skew changes during the mosaicking process, an exact match of the same imaged area is not possible. The depth-correction was performed during mosaicking.

All single images from both scenarios were automatically segmented using the same approach used for mosaic images. All possible combinations of single images were created as

$$C_1^{N_I}, C_2^{N_I}, \dots, C_{N_I}^{N_I}; \qquad (12)$$

where N_I is the total number of available single images.

For both scenarios, all possible single images were used up to a maximum of 20 images per mosaic. This limit was set due to memory limitations. Nevertheless, most studies typically only use between 1 to 8 individual images. Figure 33 shows a histogram representing the frequency of mosaics where a given number of non-overlapping images were selected. A total of 89 mosaics had the maximum of 20 images. 156 out of 160 mosaics had at least 8 images selected.

The corneal nerve density of each image was then computed and averaged for each combination. Density values obtained were compared with the density obtained in the mosaic image to determine the absolute and relative error.

Results

Manual versus Automatic Nerve Segmentation

Corneal nerve density was computed for the automatic and manual segmentations and compared. Figure 34 shows an example of manual and automatic segmentations. The resulting agreement between manual and automated segmentation methods is strong. A Pearson correlation coefficient of 0.94 ($p < 0.001$) was achieved. Figure 35 shows obtained automatic and manual density values plotted against each other. The average obtained nerve density difference between both methods was 0.26 ± 1.38 mm/mm^2.

The manual tracing of nerves in all mosaics was performed by an experienced observer that took approximately 90-120 minutes per mosaic. The fully-automated nerve segmentation of the same mosaics, using a single core MATLAB® implementation on an Intel® Core™ i7-4770 CPU at 3.4 GHz, took between 10 and 50 seconds per mosaic. As aforementioned, the execution time to segment a single mosaic is dependent on its area. Nevertheless, automatic vs manual tracing processing speed on average corresponds to a 100-fold improvement.

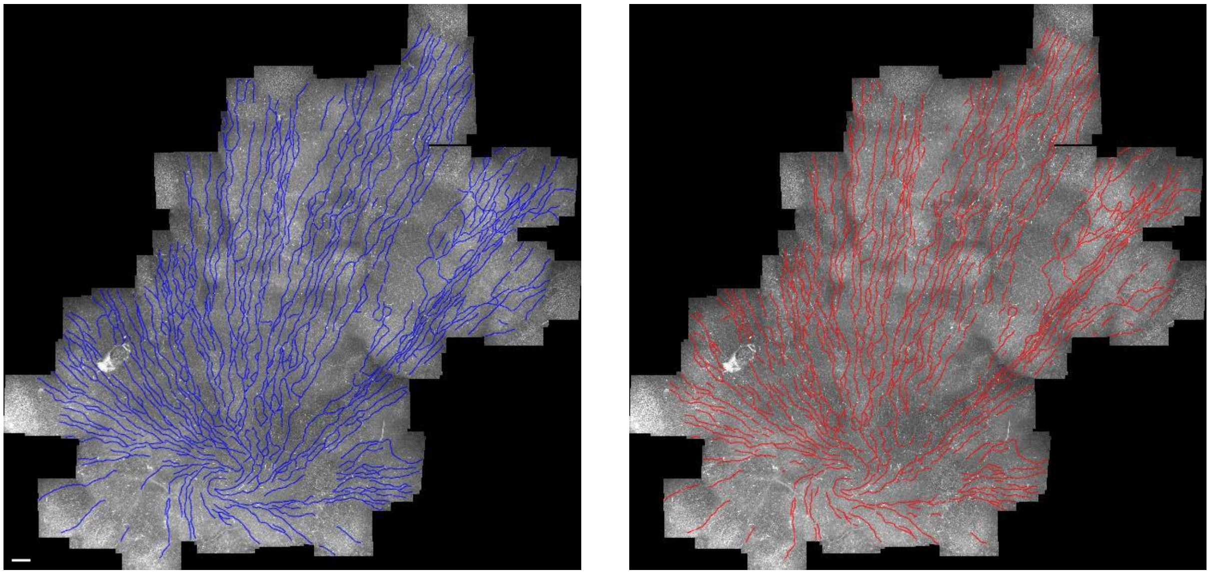

Figure 34: An example of manual (left) versus automatic (right) corneal nerves segmentation. Scale bar: 120 µm

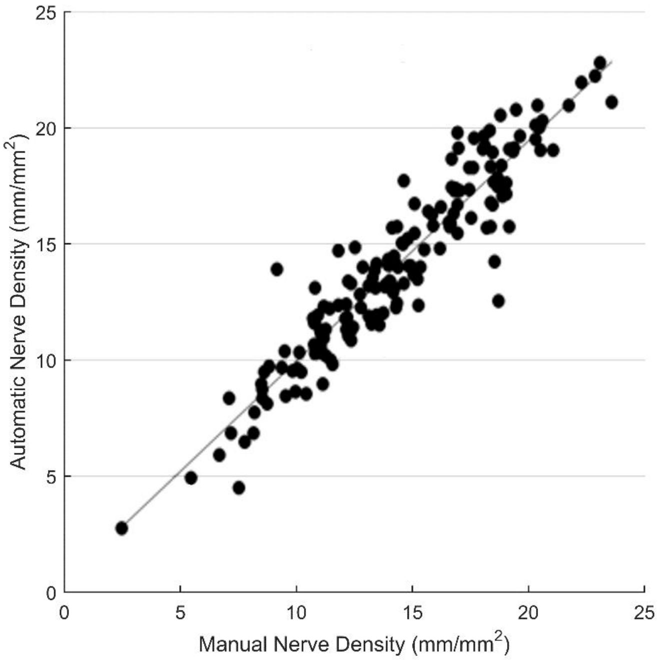

Figure 35: Manual versus automatic nerve density values (N = 160).

Inferocentral Whorl Region Analysis

The nerve distribution around the inferocentral whorl region was evaluated according to the angle and distance to the center. Regarding distance, the density within the 200 µm diameter ring is only weakly correlated to overall density, with a low correlation coefficient of 0.40 ($p<0.001$) (Figure 36a). As the diameter of the ring increases, the obtained correlation coefficient also increases. The density within the 800 µm diameter ring obtained a correlation coefficient of 0.79 ($p<<0.001$) when compared to mosaic density (Figure 36b). The density outside the 800 µm diameter ring is an almost match to the whole mosaic density (Figure 36c). A correlation coefficient of 0.99 ($p<<0.001$) was obtained when compared to mosaic density.

The inferocentral whorl region density directional variation (according to the angle) was also investigated. A 45° arc was rotated in 12° increments around the entire 800 µm diameter ring. At each rotation the density was recorded. Results for a given subject are shown in Figure 37(a) and (b). A left/right eye symmetry was generally observed in the data.

For each available mosaic, the arcs with maximum and minimum nerve density were recorded. The values are plotted as a function of direction in Figure 37(c) and (d), respectively. In both right and left eyes, maximum density was verified mostly in the superior region. As shown, no clear directional preference was noted for the minimum nerve density. Maximum nerve density was 2 to 6 times higher than minimum nerve density.

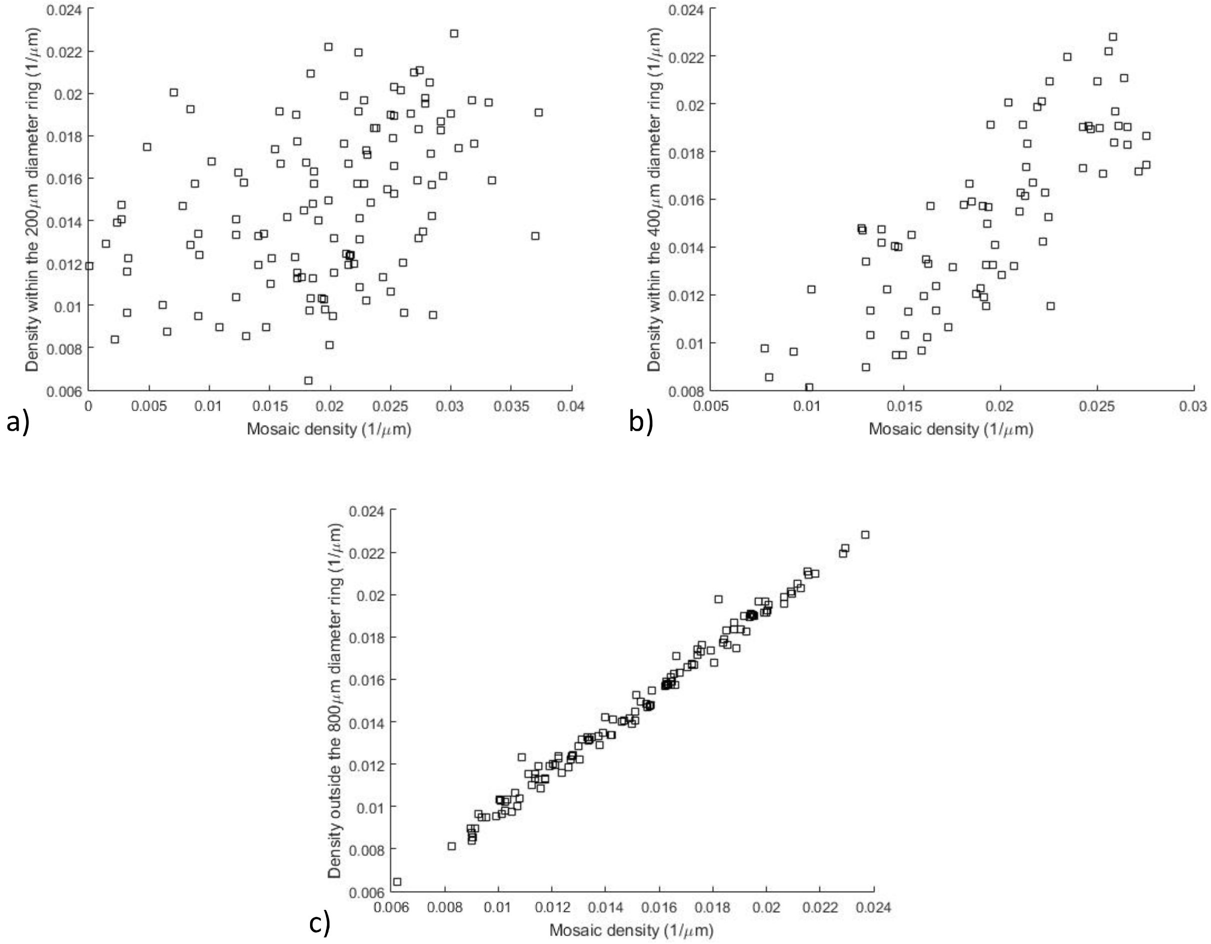

Figure 36: Inferocentral whorl region nerve density analysis according to distance to its center: Mosaic density values versus corneal nerve density (a) within the 200 μm ring (N=124), (b) within the 800 μm ring (N=81), and (c) outside the 800 μm ring (N=124).

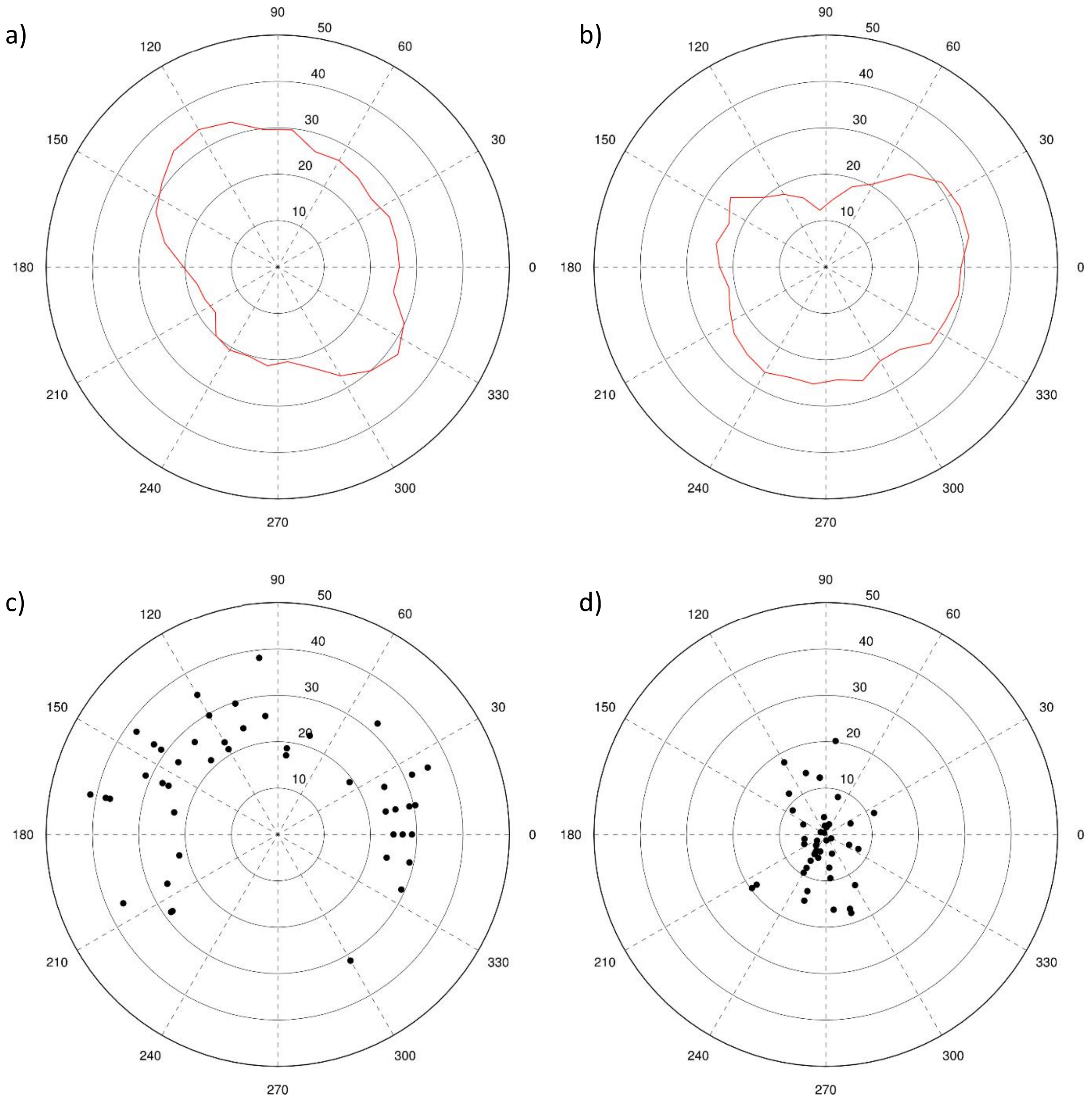

Figure 37: Inferocentral whorl region nerve density analysis according to direction. In the polar charts the angle represents direction (°), and distance to the center represents nerve density (mm/mm^2). An example of nerve density distribution according direction on a single normal subject is shown for (a) the left and (b) right eyes. (c) and (d) show the directions with the maximum and minimum subbasal nerve density for the right eye, respectively.

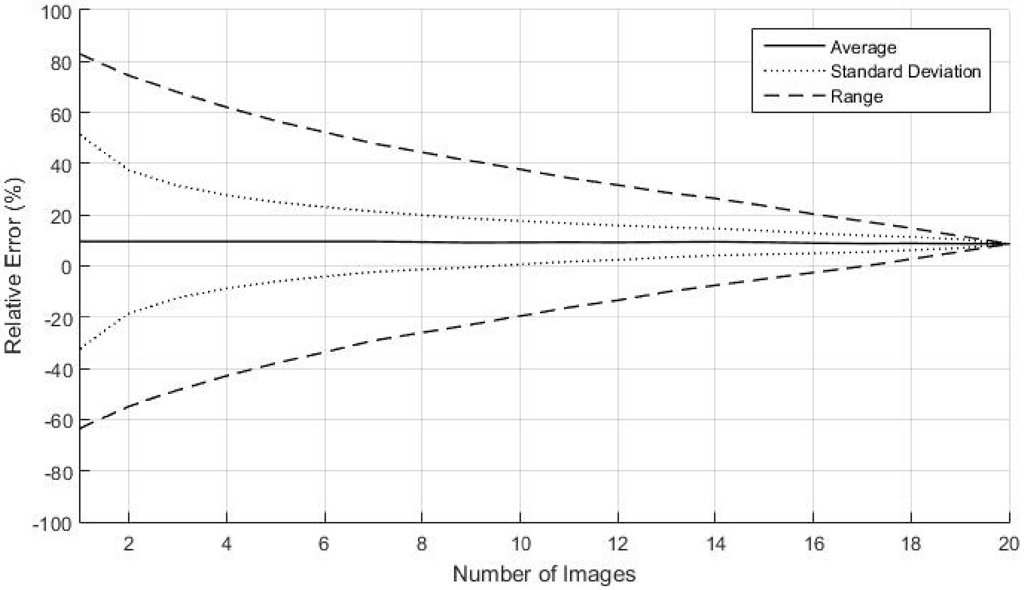

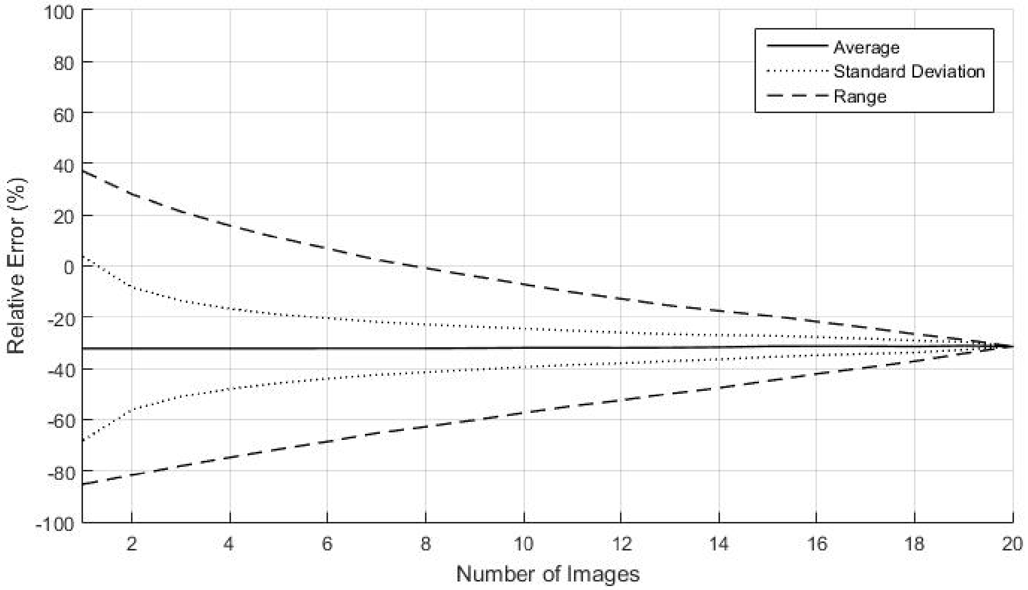

Figure 38: Relative error (%) of the average nerve density computed from multiple non-overlapping single confocal microscopy images against the mosaic nerve density. The error range, standard deviation and average (dashed, dotted, and full line respectively) are shown according to the number of images combined. On top, depth-corrected images were cropped from the mosaic (scenario 1). On the bottom, raw images were used instead.

Single Image versus Mosaic Analysis

An important question for corneal nerve analysis is whether sampling nerves from a combination of single images is an accurate estimation of corneal nerve density. In this work, this question is addressed. Two scenarios were tested. In scenario 1 new images were created by cropping the mosaic itself. The resulting images represent optimal depth-corrected fields of view. In scenario 2, images were selected from the initial image pool (used to create the mosaic) – raw non-depth-corrected images. For each scenario, up to 20 non-overlapping images per available mosaic were used.

Nerve density was calculated for each possible combination. As an example, there are 125970 possible combinations of 8 images out of a set of 20. The average, standard deviation, and range of the resulting nerve density error (computed as the difference between mosaic and combination nerve density) were then computed for each set of combinations with the same n, where n is the number of combined images ($n = 1,2,\ldots,N_I$, up to 20 images per mosaic). The obtained results for both scenarios are shown in Figure 38.

For the first scenario, the combination of multiple images yields an average 10% overestimation error when compared to mosaic nerve density. The overestimation is somewhat expected. When cropping the mosaic, the border regions are typically under-sampled. This regions include fewer nerves, *i.e.* a lower nerve density.

As fewer images are used to sample the subbasal plexus, the density error relative to the mosaic reference increases. For example, with only 1 image the obtained nerve density error ranges between 63% of underestimation to 83% of overestimation, while choosing 8 non-overlapping depth-corrected images results in an nerve density error range of -26% (underestimation) to 45% (overestimation).

Despite some exceptions, the usage of depth-corrected images is not common. Scenario 2 (non-depth-corrected raw images) is a more realistic scenario. Images are used right after acquisition without any need for processing.

For scenario 2, an average 32% underestimation error compared to mosaic nerve density was achieved when combining multiple images. Similarly to the first scenario, as the number of available images decreases, the nerve density error range increases. With a single image, the obtained nerve density error ranges from -85% (underestimation) to 37% (overestimation). By increasing the number of images to be combined to 8, nerve density error ranges between -63% (underestimation) to no error (0%).

The obtained average underestimation error for scenario 2 can be explained by the lack of depth-correction. Confocal microscopy was used to image the subbasal plexus. In non-depth-corrected images nerves appear and disappear as they '*move*' in and out of the plane of focus. Depth-corrected images overcome this problem. Thus, the underestimation error verified. Figure 39 shows non-depth-corrected images compared to depth-corrected images. As shown, fewer nerves are visible in non-depth-corrected images.

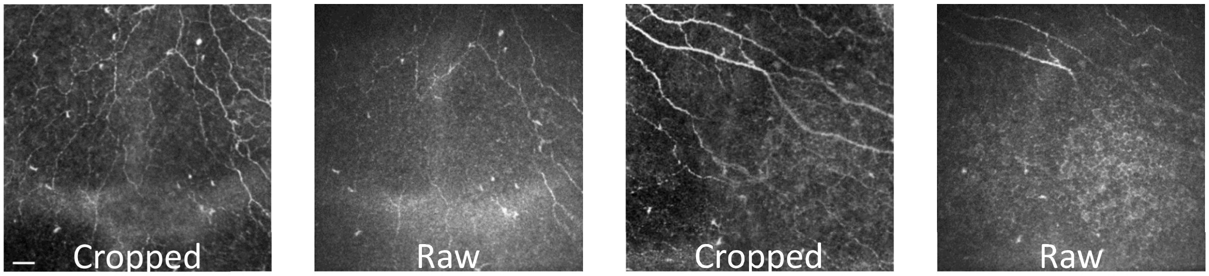

Figure 39: Images cropped from the mosaic versus raw non-depth-corrected images. Scale bar: 30 µm

Discussion

The density of corneal nerves in the subbasal plexus is already an established peripheral nerve degeneration marker. In this work, we explored the automatic corneal nerve density as computed from mosaic images.

Visible corneal nerves were automatically segmented and the computed nerve density compared to a manual approach. Both healthy and diseased subjects were used. The obtained automatic values were highly correlated to the manual ones, which confirms the results from the previous section ("*Corneal Nerves Segmentation*").

One of the main advantages of automatic approaches is their processing speed. The time required to manually segment a mosaic image (in this study 90 to 120 minutes per mosaic) is unfeasible in the daily clinical practice. With the same images, the proposed automatic approach was around 100 times faster (10 to 50 seconds per mosaic). The obtained results, further demonstrate the feasibility of fully-automatic corneal nerve density analysis from mosaic images, for both research and clinical practice.

It has been suggested that the selective analysis of the inferocentral whorl region could provide capital information towards diagnostics [120]–[122]. Nevertheless, the obtained results cast some doubts on these hypothesis.

Concentric rings centered in the whorl region were created to isolate the whorl region. The diameter of the rings was between 200 and 800 µm (a total of 7 rings, with 100 µm diameter increments). The nerve density within each ring was then computed. Within the smallest ring (200 µm of diameter) a low correlation coefficient to mosaic nerve density (0.40) was obtained. The correlation between ring and mosaic nerve density increased as the ring diameter increased. Further tests on whorl nerve density vs disease were carried and presented in [99].

Perhaps the most important conclusion from this study came from the comparison of single image analysis against mosaic analysis. It is clear that a single confocal image covers only a small area of the corneal subbasal plexus. Thus, multiple regions of the cornea are sometimes sampled to compute nerve density. In this study we compared this methodology against mosaic nerve density. The obtained results show that even when multiple single images from different regions of the cornea are acquired, large random errors occur.

Cross-study comparisons have shown a large variability in some reported corneal nerve parameters [123], [124]. It is impossible to understand the exact causes of the variability, as it may be inherent to the different study populations or used methodology. Nevertheless, it may be that the results presented here partially contribute to the observed variability.

Two important exceptions must be taken into account. It is possible that overestimation and underestimation biases can partially cancel each other. Furthermore, biases may be normally distributed on both normal and diseased subjects. In both cases, errors would be masked and not affect the obtained conclusions. Still, there is risk that should be taken into account in future studies. Even when not considering the comparison to mosaic density, the obtained high variability of computed nerve density with 8 or less images is a matter of concern.

In [99], the methodology presented here, has been used to study mosaic nerve density in normal and diseased subjects with type 2 diabetes mellitus.

CORNEAL NERVES TORTUOSITY

Recently, a particular increasing interest in corneal nerves tortuosity has surged. It is now a widely studied corneal nerve property. Many studies have found links between tortuosity and dry eye disease [125] or keratoconus [109]. Furthermore, correlation to systemic diseases such as diabetes [51], [126] rheumatoid arthritis [127], Wilson's disease [128], or amyotrophic lateral sclerosis [56], have been studied. However, the interpretation and consequently the quantification of this biomarker by clinicians can vary widely. Although, in theory, tortuosity can be defined as the degree of 'twistedness' of a curve, in practice, there is still no gold standard tortuosity measurement or definition.

Over the years, a number of quantitative metrics on tortuosity have been proposed. These focus mainly on retinal vessels [129]–[132]. Nevertheless, several studies have looked at tortuosity metrics specifically applied to corneal nerve tortuosity [108], [112], [133].

In [134], 10 clinical experts separately ranked 30 confocal images of the subbasal nerve plexus according the tortuosity of visible corneal nerves. Expert rankings were then compared by means of correlation. Obtained correlation coefficients ranged from 0.43 to 0.73. This clearly shows the high variability of tortuosity grading and creates unwelcome doubt on tortuosity studies.

In the literature, it is possible to find different studies regarding corneal nerve tortuosity in both diabetic peripheral neuropathy and dry eye disease that reach conflicting results [123], [125], [135]. Although the precise reasoning behind the observed differences cannot be pinpointed, it is possible that the lack of standardized tortuosity contributed negatively to the issue.

The clinical perception of corneal nerve tortuosity was recently hypothesized to have two distinct patterns [134]. These are defined by short-range (low amplitude, high frequency) or long-range (high amplitude, low frequency) directional changes. The introduction of this duality was shown to improve correlation between different graders [134]. Thus, it is possible it may also improve the current relation between perceived and measured tortuosity. Furthermore, it reinforces the idea that tortuosity is a multifaceted problem, that maybe a single mathematical definition cannot answer. Recently, the multi-scale nature of corneal nerve tortuosity was addressed in [133].

In this work, we explore established and novel tortuosity metrics against these novel focused definitions of tortuosity (long-range and short-range tortuosity). We also test whether a mixed model

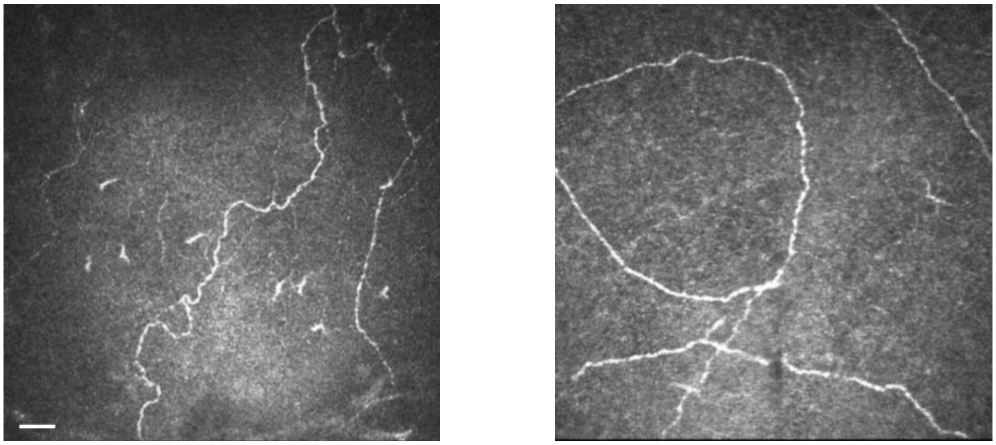

Figure 40: Corneal confocal images with the highest nerve tortuosity according to the short-range (left) and long-range (right) tortuosity definitions, respectively. Scale bar: 30 µm

created from the combination of multiple tortuosity metrics handles the multifaceted nature of tortuosity better than single mathematical definitions.

Materials and Methods

Materials

A set of 30 ordered nerve confocal images based on short- and long-range tortuosity definitions were used as ground truth in the current study. The full efforts in order to create and characterize this dataset are described in detail in [134]. Shortly, a set of 30 high-quality images from healthy (N=10) and diseased (N=20) subjects were selected (one image per subject). All images were acquired from the corneal subbasal plexus using the HRT-II with the Rostock Cornea Module, covering a field of $400 \times 400\ \mu m$ $(384 \times 384$ pixels).

Seven experienced clinical graders were asked to sort the set of 30 images arranging them in order of increasing tortuosity. Specific definitions of tortuosity regarding its scale were provided to the graders – images were sorted based on short-range tortuosity (SRT), characterized by frequent small-amplitude directional changes, and long-range tortuosity (LRT), characterized by infrequent large-amplitude directional changes. The final ground truth sortings (for LRT and SRT) are the ordered lists of the average sorting position of the seven graders. Figure 40 shows the corneal confocal microscopy images with the highest nerve tortuosity according to both SRT and LRT definitions.

In [134], the SRT and LRT sortings showed poor correlation with each other. This suggests two different tortuosity definitions that can be easily distinguishable by clinical graders. Furthermore, the provided specific tortuosity definitions improved intergrader agreement when compared to normal grading [134].

Corneal Nerve Tracing

The centerlines of all visible nerves in the selected 30 images were fully manually traced pixel-by-pixel by an experienced observer. The resulting binary images were then processed to obtain the position of each sequential nerve centerline point. At branching, the main nerve was selected, while a new segment was created for secondary branching. When possible, nerves were connected between small gaps, to obtain a more complete nerve tree. Distance, angle, and signal intensity were considered. At the end an observer was able to check each of these steps and correct if necessary. The nerve tracings were then defined as a spline and subsequently sampled at regular intervals ($0.01\ \mu m$).

Due to the relative low resolution of *in vivo* corneal confocal microscopy, sampling artifacts are common. These can be highly detrimental for tortuosity purposes by introducing high frequency directional changes. For this reason, it is normal to apply a smoothing function. However, because we are trying to distinguish between SRT and LRT, the function of choice must be carefully considered – for instance, if smoothing is overdone, LRT is highlighted, but SRT is masked.

In this study we decided to take advantage of this fact. By applying three different smoothing functions, with increasing scale, we hope to highlight differences between the two tortuosity classes. As a result, each nerve segment is defined by an ordered set of xy positions as $[(x_i^\sigma, y_i^\sigma),\ i = 1, \dots, n]$, with n being the total number of coordinates and σ the scale of the smoothing function ($\sigma = 1,2,3$). Figure 41 shows a traced nerve segment processed with each σ.

Figure 41: Original traced nerve segment (a) and smoothed segment at different scales (b-d).

Nerve Tortuosity Metrics

As aforementioned, there is no standardized definition of tortuosity. As a result, multiple metrics have been proposed over the years. Although all of them are focused in quantifying the degree of "twistedness" of a nerve (or other line-like structure), multiple general approaches have been taken. Typically, tortuosity measurements fall into one of four categories: length-, angle-, curve-, or twist-based measurements. In order to have a global view of tortuosity, we have specifically selected measurements from each of these groups. In this section all the implemented tortuosity metrics are described in detail.

Length-based Tortuosity

One of the first and most widely used measurements of tortuosity is the Arc over Chord Length ratio (AOC). This simple metric was introduce first by [136]. It is computed as the ratio between the length of nerve segment (L) over the length of its chord (L_c) as:

$$AOC = \frac{L}{L_c}, \tag{13}$$

where

$$L = \sum_{1}^{n} \sqrt{\Delta x_i^{\sigma\,2} + \Delta y_i^{\sigma\,2}}, \tag{14}$$

$$L_c = \|(x_1^\sigma, y_1^\sigma) + (x_n^\sigma, y_n^\sigma)\|. \tag{15}$$

This metric has been largely contested, as the same tortuosity value is given to a smoothly curved nerve or to a raggedly twisted one.

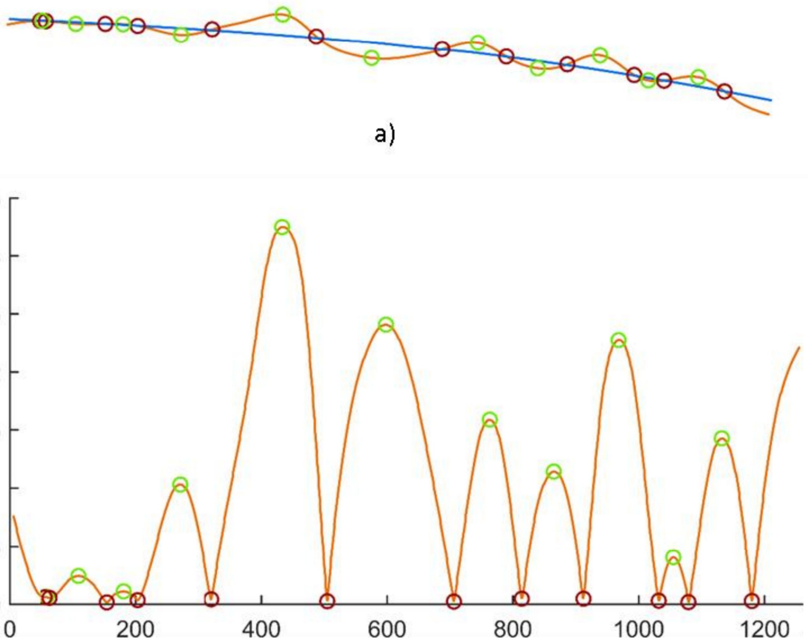

a)

b)

Figure 42: (a) Original (orange) and Savitzky-Golay filtered (blue) nerve segment. (b) Absolute difference between both curves. Marked in red and green are the local maximums and minimums, respectively.

In this study we also propose a novel length-based measurement. Each nerve segment is first filtered using a Savitzky-Golay filter. This consist of fitting, at each sampled position, a low-degree polynomial curve to neighboring points [92]. Upon experimentation, the polynomial degree was set to 2 and the length of the neighboring region to 5 μm. The result is a smooth curve, defined by $\left[\left(x_i^{SG}, y_i^{SG}\right),\ i\ = 1, \ldots, n\right]$, with no high-frequency directional changes. Figure 42(a) shows an example of this process. The Length Ratio (LR) is then computed as:

$$LR\ = \frac{L}{L_{SG}}, \tag{16}$$

where L_{SG} is the length of the filtered curve, computed as

$$L = \sum_{1}^{n} \sqrt{\Delta x_i^{SG^2} + \Delta y_i^{SG^2}}. \tag{17}$$

While AOC measures the deviation from a straight line, LR quantifies the deviation from a smooth curve.

Angle-based Tortuosity

This class of tortuosity metrics are based in the quantification of angle differences between consecutive vectors computed at discrete steps from the curve. Several implementations of this class of methods exist in the literature [130], [137]. For any point P_i, defined by (x_i, y_i), let us consider vectors $\overrightarrow{V1}_i$ and $\overrightarrow{V2}_i$ computed as

$$\begin{aligned}\overrightarrow{V1}_i &= P_i - P_{i-1}, \\ \overrightarrow{V2}_i &= P_{i+1} - P_i.\end{aligned} \tag{18}$$

The sum of angles metric ($SOAM$) is computed as

$$SOAM = \sum_{2}^{n-1} arccos \frac{\overrightarrow{V1}_i \overrightarrow{V2}_i}{\|\overrightarrow{V1}_i\| \|\overrightarrow{V2}_i\|}. \tag{19}$$

Curve-based Tortuosity

Curve-based tortuosity metrics are similar to angle-based ones. The idea is to quantify the curvature k_i over the entire nerve segment [130], as

$$AC = \sum_{3}^{n} |k_i|, \tag{20}$$

where AC is the absolute curvature and k_i is computed as

$$k_i = \frac{\Delta x_i^\sigma \Delta^2 y_i^\sigma - \Delta^2 x_i^\sigma \Delta y_i^\sigma}{\left(\Delta x_i^{\sigma 2} + \Delta y_i^{\sigma 2}\right)^{3/2}}. \tag{21}$$

Twist-based Tortuosity

The number of curve "twists" or "inflections" have been used as measurement of tortuosity [112], [137]. It seems straightforward that the higher the number of twists in a nerve, the more tortuous it is. More recently, the amplitude of the turn curve (defined as the curve between consecutive twists) has also been considered. For a curve with the same number of twists, a higher turn curve amplitude is clearly a good indication of a larger tortuosity value. In this study, two twist based metrics were used.

The tortuosity index (TI) was considered. This metric has already been described in section "*Corneal Nerves Segmentation*". Shortly, each nerve segment is partitioned into m subsegments ($s = s_1 \oplus s_2 \dots \oplus s_m$) [112]. TI is then computed as

$$TI = \frac{m-1}{m} \sum_{1}^{m} \left(\frac{L_c^{s_j}}{L^{s_j}} - 1 \right), \tag{22}$$

where L^{s_j} and $L_c^{s_j}$ are arch and chord length, respectively, of subsegment s_j.

In addition to TI, a novel twist-based measurement is also computed. Let us consider the absolute difference between the nerve curve (x_i^s, y_i^s) and the filtered curve $\left(x_i^{SG}, y_i^{SG}\right)$ where $i = 1, \dots, n$. Figure 42(b) shows the obtained result.

The number of twists and the amplitude of the turn curve may be derived from the local maximums and minimums of the obtained difference. As so, the proposed metric (High-pass Twist Tortuosity, HTT) may be computed as

$$HTT = \sum_{1}^{m} A_j \ , \tag{23}$$

where m is the total number of local maximums and A_j is the amplitude at the local maximum j ($j = 1, \dots, n$) computed as the difference between the local maximum and the average of the two surrounding local minimums.

Normalization

Angle-, curve-, and twist-based tortuosity measurements are computed locally. From the literature, many normalization factors have been proposed. For instance, several studies have used these metrics weighted by the length of the segment or its chord [112], [137]. However, it is not clear if this is advantageous.

A typical corneal confocal image may contain nerve segments with a large length variability. By applying this normalization, small segments are weighted as much as large ones. In this study we have decided to test this by applying different normalization factors. As so, each of these metrics is weighted by: 1 (no normalization); L; L_c; L_{SG}; and $\sum L$ (the sum of all segment lengths – image-based normalization).

Image-level Tortuosity

In the "*Neve Tortuosity Metrics*" section, we have described in detail all the computed tortuosity metrics for a single nerve. However, the goal is to evaluate image-level tortuosity. Different methods were used to combine all the individual nerve tortuosities into a single image-level value:

1. The average value for all nerves;
2. The maximum value for all nerves;
3. The 75th percentile;
4. The average value of the (at most) 3 longest nerves;
5. The average value of all nerves whose length is within 15% of the longest nerve.

Mixed Model

Deriving image-level tortuosity values is a complex task. The human perception of a given image tortuosity is convoluted, as it does not depend simply in mathematical straightforward operations. Many factors are taken into account. However, most studies so far have relied in a single view (mathematical feature) of tortuosity. We believe that in order to create a more comprehensive and robust tortuosity measurement, several features should be used together. In our opinion, for instance, the question should not be if image-level tortuosity should be derived by the average or 75th percentile, but instead in which way these can be combined to coherently explain clinical graders perception.

Each of the multiple variations of the proposed tortuosity metrics (features) is computed for all the 30 images. Spearman Rank Correlation (SRC) is then applied in order to rank all the features according to the two used ground-truths (for LRT and SRT). The 50 features with the highest SRC coefficient were then selected for each tortuosity definition.

A stepwise selection was then applied. Starting with the single best feature, leave-one-out cross-validation was used to test the predictive power of a linear regression model. SRC is then computed as a measure of fitness. A bidirectional elimination approach (add or remove features) is applied to evolve the algorithm. In the end, the best possible feature set (highest SRC coefficient) is selected.

Results

Single Feature

Best SRC coefficients for each metric according to SRT and LRT are summarized in Tables 3 and 4, respectively.

Table 3: Best SRC coefficients for each computed metric with respect to the short-range tortuosity (SRT) ground-truth.

Metric	σ	Normalization	Image-level*	SRC
$SOAM$	1	L	4	0.901
HTT	1	$\sum L$	5	0.887
LR	1	-	5	0.886
AC	1	L_c	1	0.823
TI	1	$\sum L$	4	0.759
AOC	3	-	1	0.555

* 1 - Average; 2 - Maximum; 3 - 75th percentile; 4 - Average of the three longest nerves; 5 - Average of 15% of the longest nerves

Table 4: Best SRC coefficients for each computed metric with respect to the long-range tortuosity (LRT) ground-truth.

Metric	σ	Normalization	Image-level*	SRC
TI	3	1	4	0.925
AOC	1	-	4	0.882
HTT	1	$\sum L$	2	0.766
$SOAM$	1	$\sum L$	2	0.739
AC	2	$\sum L$	1	0.677
LR	2	-	5	0.441

* 1 - Average; 2 - Maximum; 3 - 75th percentile; 4 - Average of the three longest nerves; 5 - Average of 15% of the longest nerves

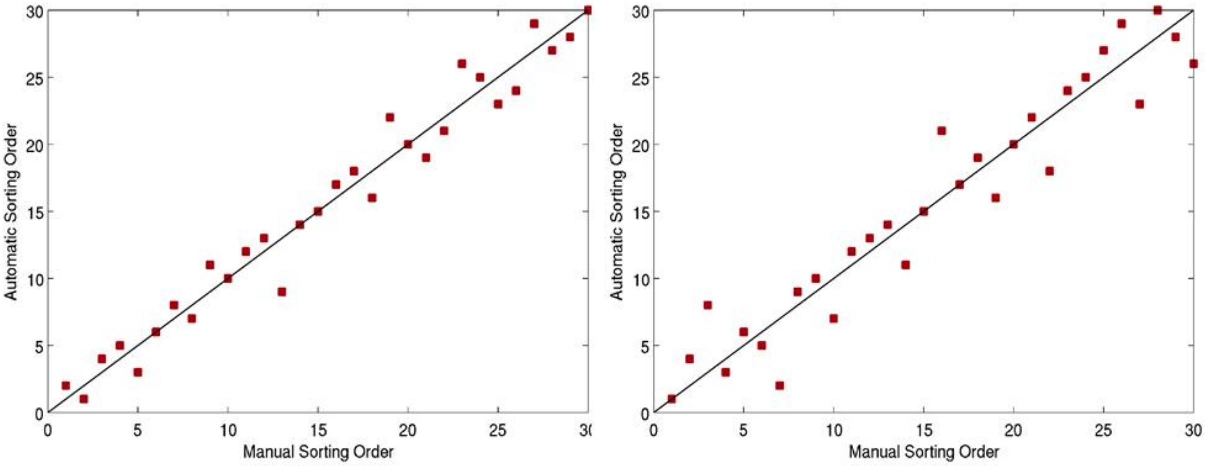

Figure 43: Automatic (best combination of tortuosity features) vs manual sorting order for the short range (left) and long range (right) tortuosity definitions, respectively.

For both tortuosity subtypes (SRT and LRT) high SRC values (>0.9) were achieved with at least one of the evaluated tortuosity metrics.

The metrics that achieved the highest SRC values for one of the subtypes, perform considerably worst for the other. While $SOAM$, HTT, and LR correlate well to SRT and poorly to LRT, TI and AOC correlate well to LRT and poorly to SRT. This reasserts the difference between the two definitions.

Mixed Model

As aforementioned, we combined different tortuosity metrics and/or variants in an attempt to improve single metric results. We were able to achieve SRC coefficients of 0.985 and 0.959 with respect to the SRT and LRT ground-truths, respectively. Figure 43 shows the proposed tortuosity metrics against SRT and LRT ground truths.

For the SRT model the combination of 19 variants of $SOAM$, HTT, LR, and AC metrics yielded the best results. Additionally, for the LRT model it was the combination of 13 variants of TI and AOC metrics that yielded the best results. Between the two models, the main difference is the included tortuosity metrics, since there was no preference for specific normalization, σ, and image-level aggregation approaches.

For both subtypes of tortuosity, SRT and LRT, the combination of multiple metrics achieved higher SRC coefficients than any single metric.

Discussion

Although corneal nerve tortuosity has become a widely used parameter for the assessment and diagnosis of several diseases, we still lack a standard definition of this nerve property. Because of this, studies have shown contradictory results [123], [125], [135]. In an attempt to reduce ambiguity, two distinct forms of corneal nerve tortuosity have been identified, describing either short-range or long-range directional changes (SRT and LRT, respectively) [134]. By defining focused tortuosity definitions, intergrader agreement was improved when compared to a single definition [134]. In this study we were able to automatically estimate corneal nerve tortuosity measurements that accurately and independently correlate to these two subtypes of tortuosity.

Over the years, multiple approaches to quantify corneal nerve tortuosity have been proposed. However, most of these, focus on quantifying a specific geometrical property. This might explain the low agreement between proposed measurements and grader perception. Herein, instead, we fitted an objective mathematical description to the expert clinical perception. We recognized the multifaceted nature of tortuosity by not looking to a single geometrical property, but to a possible combination of multiple tortuosity features. These included widely used measurements as well as novel ones. We have also looked at every step of the computation, from the smoothing of nerve tracings to the aggregation techniques, and tested for multiple alternatives.

We chose to use manual corneal nerves segmentation instead of the automatic approach presented in section "*Corneal Nerves Segmentation*". Our goal was to evaluate tortuosity independently of segmentation quality/accuracy. In the future, the obtained model should be tested with automatic nerve segmentations.

In this work, we were able to improve on single metric results and achieve SRC coefficients of 0.985 and 0.959 with respect to the SRT and LRT ground-truths, respectively. This shows that the proposed method highly correlates to clinical perception.

CONCLUSIONS

The main goal of this work was to investigate the feasibility of using the cornea and conjunctiva as alternative sources of information on both ocular and systemic diseases. The eye structure usually chosen for this purpose is the retina. Thus, studies on conjunctival blood vessels and corneal nerves are still few in comparison. We proposed to develop novel software tools to explore and aid the exploration of these alternative research fields; to obtain information on conjunctival blood vessels, hemodynamics from video recordings, and nerve morphology from corneal confocal microcopy images. With this we provided a lead way on new and improved disease markers to aid in the diagnosis and monitoring of different pathologies.

Vascular Tree and Blood Flow Analysis

A software capable of segmenting conjunctival blood vessels in due time was proposed and described. The same algorithm was then used as basis for the development of a software tool capable of measuring blood flow velocity from video recordings. Three modules compose the proposed software: Registration, Segmentation, and Velocity Measurement. All the developed software modules proved adequate to their tasks.

The proposed algorithm was tested in computer generated simulations and *in vivo* video recordings from chick CAM vessels. With the former, it was shown the high accuracy achieved, even in conditions such as low contrast. With the latter, both the obtained curves shape and measured velocities were as expected. Furthermore, we demonstrated the algorithm robustness by using video recordings with different resolutions, frame rates, and/or acquisition cameras.

Assessing this physiological property is of great interest, as it can help to better understand the fundamentals of the vascular system adaptation. In the future, the implementation of the proposed algorithm to video recordings from conjunctival vessels may provide important information on blood flow and aid in the detection and monitoring of systemic diseases.

Corneal Subbasal Nerve Plexus

The analysis of the corneal nerves from images of the subbasal nerve plexus is of high interest in the ophthalmologic field, as they can be used to predict and monitor both corneal and systemic diseases [54], [57], [123], [138]. Visual inspection, or manual/semi-automatic quantification methods, are sometimes still used in research or the clinical practice. However, these are time consuming, subjective, non-reproducible, and overall impractical in a clinical environment. In this work, we developed a fast and accurate fully automated method to segment visible nerves from confocal microscopy images of the human cornea.

We demonstrated that the proposed algorithm is capable of segmenting the nerves of individual images, in both normal and tortuous conditions. The achieved accuracy in nerve determination is comparable to a human grader. Furthermore, it improves on previously proposed methods. The low running time achieved means that features, such as corneal nerve density or tortuosity, can be determined from single images in just a few seconds.

A fast nerve segmentation algorithm is especially important if the analysis of wide-field mosaics is intended. These large images cover a much wider area of the central cornea. However, they are computationally challenging and existing automated analysis methods cannot cope with them in reasonable time. A fast method capable of segmenting the corneal nerves from mosaics is of interest. The proposed algorithm was capable of segmenting wide-field mosaic images in just tenths of seconds. Furthermore, the automatic nerve density computed from the mosaic images was highly correlated to the manual ground-truth. The obtained results, further demonstrate the feasibility of fully-automatic corneal nerve density analysis from mosaic images.

We have shown that the corneal nerve density averaged from multiple single images (sampled from different regions of the cornea) yield large random errors. Furthermore, we confirmed overestimation bias, due to uneven sampling of the subbasal plexus, and underestimation bias, due to depth artifacts. The obtained results cast doubts on current methodologies, and may partially explain the large variability verified in some cross-study comparisons [123], [124].

Another disease marker of interest is the tortuosity of corneal nerves. This morphological feature has already been linked to several pathologies [51], [56], [126]. However, the lack of a standard definition highly limits its reproducibility. Two distinct forms of corneal nerve tortuosity have been identified, SRT and LRT [134]. In this work, automatic corneal nerve tortuosity measurements that accurately and independently correlate to the two subtypes of tortuosity were created. Using a combination of different mathematical tortuosity measurements, we were able to create a tortuosity measurement that highly correlates to clinical perception.

REFERENCES

[1] L. A. Remington, “Visual Pathway,” in *Clinical Anatomy and Physiology of the Visual System*, Elsevier/Butterworth-Heinemann, 2012, pp. 233–252.

[2] L. Levin, S. Nilsson, J. Ver Hoeve, S. Wu, P. Kaufman, and A. Alm, “Optic Nerve,” in *Adler’s Physiology of the Eye*, 11th ed., Saunders/Elsevier, 2011, pp. 550–573.

[3] “Schematic diagram of the human eye - Wikipedia.” [Online]. Available: https://en.wikipedia.org/wiki/File:Schematic_diagram_of_the_human_eye_en.svg#globalusage.

[4] L. A. Remington, “Cornea and Sclera,” in *Clinical Anatomy and Physiology of the Visual System*, Elsevier/Butterworth-Heinemann, 2012, pp. 10–39.

[5] L. Levin, S. Nilsson, J. Ver Hoeve, S. Wu, P. Kaufman, and A. Alm, “Cornea and Sclera,” in *Adler’s Physiology of the Eye*, 11th ed., Saunders/Elsevier, 2011, pp. 71–130.

[6] L. A. Remington, “Visual System,” in *Clinical Anatomy and Physiology of the Visual System*, Elsevier/Butterworth-Heinemann, 2012, pp. 1–9.

[7] R. S. Snell and M. A. Lemp, “The Eyeball,” in *Clinical Anatomy of the Eye*, Blackwell Science Ltd,., 1997, pp. 132–213.

[8] L. Levin, S. Nilsson, J. Ver Hoeve, S. Wu, P. Kaufman, and A. Alm, “Three Dimensional Rotations of the Eye,” in *Adler’s Physiology of the Eye*, 11th ed., Saunders/Elsevier, 2011, pp. 208–219.

[9] L. A. Remington, “Crystalline Lens,” in *Clinical Anatomy and Physiology of the Visual System*, Elsevier/Butterworth-Heinemann, 2012, pp. 93–108.

[10] L. Levin, S. Nilsson, J. Ver Hoeve, S. Wu, P. Kaufman, and A. Alm, “The Lens,” in *Adler’s Physiology of the Eye*, 11th ed., Saunders/Elsevier, 2011, pp. 131–163.

[11] L. Levin, S. Nilsson, J. Ver Hoeve, S. Wu, P. Kaufman, and A. Alm, “Production and Flow of Aqueous Humor,” in *Adler’s Physiology of the Eye*, 11th ed., Saunders/Elsevier, 2011, pp. 274–307.

[12] L. Levin, S. Nilsson, J. Ver Hoeve, S. Wu, P. Kaufman, and A. Alm, “The Vitreous,” in *Adler’s Physiology of the Eye*, 11th ed., Saunders/Elsevier, 2011, pp. 164–181.

[13] D. Purves *et al.*, *Neuroscience*, 3rd ed. Sunderland, Massachusetts U.S.A.: Sinauer Associates, Inc., 2004.

[14] L. A. Remington, “Retina,” in *Clinical Anatomy and Physiology of the Visual System*, Elsevier/Butterworth-Heinemann, 2012, pp. 61–92.

[15] L. Levin, S. Nilsson, J. Ver Hoeve, S. Wu, P. Kaufman, and A. Alm, “Photoresponses of Rods and Cones,” in *Adler’s Physiology of the Eye*, 11th ed., Saunders/Elsevier, 2011, pp. 411–428.

[16] L. Levin, S. Nilsson, J. Ver Hoeve, S. Wu, P. Kaufman, and A. Alm, “The Synaptic Organization of the Retina,” in *Adler’s Physiology of the Eye*, 11th ed., Saunders/Elsevier, 2011, pp. 443–458.

[17] L. A. Remington, “Ocular Adnexa and Lacrimal System,” in *Clinical Anatomy and Physiology of the Visual System*, Elsevier, 2012, pp. 159–181.

[18] R. S. Snell and M. A. Lemp, “The Ocular Appendages,” in *Clinical Anatomy of the Eye*, Blackwell Science Ltd,., 1997, pp. 90–131.

[19] L. Levin, S. Nilsson, J. Ver Hoeve, S. Wu, P. Kaufman, and A. Alm, “Formation and Function of the Tear Film,” in *Adler’s Physiology of the Eye*, 11th ed., Saunders/Elsevier, 2011, pp. 350–362.

[20] L. A. Remington, “Orbital Blood Supply,” in *Clinical Anatomy and Physiology of the Visual System*, Elsevier, 2012, pp. 202–217.

[21] A. Cruzat, D. Pavan-Langston, and P. Hamrah, “In vivo confocal microscopy of corneal nerves: analysis and clinical correlation,” in *Seminars in ophthalmology*, 2010, vol. 25, no. 5–6, pp. 171–177.

[22] C. F. Marfurt, J. Cox, S. Deek, and L. Dvorscak, “Anatomy of the human corneal innervation,” *Exp. Eye Res.*, vol. 90, no. 4, pp. 478–492, 2010.

[23] L. J. Müller, C. F. Marfurt, F. Kruse, and T. M. T. Tervo, “Corneal nerves: structure, contents and function,” *Exp. Eye Res.*, vol. 76, no. 5, pp. 521–542, 2003.

[24] L. Oliveira-Soto and N. Efron, “Morphology of Corneal Nerves Using Confocal Microscopy,” *Cornea*, vol. 20, no. 4, pp. 374–84, May 2001.

[25] N. Witt *et al.*, “Abnormalities of Retinal Microvascular Structure and Risk of Mortality From Ischemic Heart Disease and Stroke,” *Hypertension*, vol. 47, no. 5, pp. 975–981, 2006.

[26] G. Liew, J. J. Wang, P. Mitchell, and T. Y. Wong, “Retinal vascular imaging: a new tool in microvascular disease research,” *Circ. Cardiovasc. Imaging*, vol. 1, no. 2, p. 156 LP-161, Sep. 2008.

[27] R. Kawasaki *et al.*, “Retinal Microvascular Signs and 10-Year Risk of Cerebral Atrophy: The Atherosclerosis Risk in Communities (ARIC) Study,” *Stroke*, vol. 41, no. 8, pp. 1826–1828, Aug. 2010.

[28] F. N. Doubal, T. J. MacGillivray, N. Patton, B. Dhillon, M. S. Dennis, and J. M. Wardlaw, “Fractal analysis of retinal vessels suggests that a distinct vasculopathy causes lacunar stroke.,” *Neurology*, vol. 74, no. 14, pp. 1102–7, Apr. 2010.

[29] N. Patton, T. Aslam, T. MacGillivray, A. Pattie, I. J. Deary, and B. Dhillon, “Retinal vascular image analysis as a potential screening tool for cerebrovascular disease: a rationale based on homology between cerebral and retinal microvasculatures,” *J. Anat.*, vol. 206, no. 4, pp. 319–348, 2005.

[30] N. Patton *et al.*, “The Association between Retinal Vascular Network Geometry and Cognitive Ability in an Elderly Population,” *Investig. Opthalmology Vis. Sci.*, vol. 48, no. 5, p. 1995, May 2007.

[31] R. Kawasaki *et al.*, “Retinal Microvascular Signs and Risk of Stroke: The Multi-Ethnic Study of Atherosclerosis (MESA),” *Stroke*, vol. 43, no. 12, p. 3245 LP-3251, Nov. 2012.

[32] H. Yatsuya, A. R. Folsom, T. Y. Wong, R. Klein, B. E. K. Klein, and A. R. Sharrett, “Retinal Microvascular Abnormalities and Risk of Lacunar Stroke: Atherosclerosis Risk in Communities Study,” *Stroke*, vol. 41, no. 7, p. 1349 LP-1355, Jun. 2010.

[33] L. D. Hubbard *et al.*, “Methods for evaluation of retinal microvascular abnormalities associated with hypertension/sclerosis in the atherosclerosis risk in communities study,” *Ophthalmology*, vol. 106, no. 12, pp. 2269–2280, Dec. 1999.

[34] T. Y. Wong, A. Shankar, R. Klein, B. E. K. Klein, and L. D. Hubbard, “Prospective cohort study of retinal vessel diameters and risk of hypertension,” *BMJ*, vol. 329, no. 7457, pp. 79–0, Jul. 2004.

[35] M. J. Mulvany, “Are vascular abnormalities a primary cause or secondary consequence of

hypertension?," *Hypertension*, vol. 18, no. 3 Suppl, 1991.

[36] J. H. Silverstein and a L. Rosenbloom, "Type 2 diabetes in children.," *Curr. Diab. Rep.*, vol. 1, no. 1, pp. 19–27, 2001.

[37] K. D. Kochanek, J. Xu, S. L. Murphy, A. M. Minino, and H.-C. Kung, "National Vital Statistics Reports Deaths : Final Data for 2009," *Natl. Cent. Heal. Stat.*, vol. 60, no. 3, pp. 1–117, 2012.

[38] Centers for Disease Control and Prevention, "National Diabetes Statistics Report , 2014 Estimates of Diabetes and Its Burden in the Epidemiologic estimation methods," *US Dep. Heal. Hum. Serv.*, pp. 2009–2012, 2014.

[39] D. S. Fong *et al.*, "Retinopathy in Diabetes," *Diabetes Care*, vol. 27, no. SUPPL. 1, 2004.

[40] M. Shahidi, J. Wanek, B. Gaynes, and T. Wu, "Quantitative assessment of conjunctival microvascular circulation of the human eye.," *Microvasc. Res.*, vol. 79, no. 2, pp. 109–13, Mar. 2010.

[41] I. T. Alizade, "Acoustic dysfunction and microcirculation in patients with diabetes mellitus," *Vestn. Otorinolaringol.*, no. 1, pp. 11–3, 2007.

[42] K.-D. Schaser *et al.*, "Noninvasive analysis of conjunctival microcirculation during carotid artery surgery reveals microvascular evidence of collateral compensation and stenosis-dependent adaptation," *J. Vasc. Surg.*, vol. 37, no. 4, pp. 789–797, Apr. 2003.

[43] A. G. Koutsiaris, S. V. Tachmitzi, and N. Batis, "Wall shear stress quantification in the human conjunctival pre-capillary arterioles in vivo," *Microvasc. Res.*, vol. 85, pp. 34–39, 2013.

[44] A. G. Koutsiaris *et al.*, "Volume flow and wall shear stress quantification in the human conjunctival capillaries and post-capillary venules in vivo," *Biorheology*, vol. 44, no. 5–6, pp. 375–386, 2007.

[45] S. DUENCH, T. SIMPSON, L. W. JONES, J. G. FLANAGAN, and D. FONN, "Assessment of Variation in Bulbar Conjunctival Redness, Temperature, and Blood Flow," *Optom. Vis. Sci.*, vol. 84, no. 6, pp. 511–516, Jun. 2007.

[46] D. V Patel and C. N. J. McGhee, "In vivo confocal microscopy of human corneal nerves in health, in ocular and systemic disease, and following corneal surgery: a review," *Br. J. Ophthalmol.*, vol. 93, no. 7, pp. 853–860, Jul. 2009.

[47] T. U. Linna, M. H. Vesaluoma, J. J. Pérez–Santonja, W. M. Petroll, J. L. Alió, and T. M. T. Tervo, “Effect of Myopic LASIK on Corneal Sensitivity and Morphology of Subbasal Nerves,” *Invest. Ophthalmol. Vis. Sci.*, vol. 41, no. 2, p. 393, 2000.

[48] M. P. Calvillo, J. W. McLaren, D. O. Hodge, and W. M. Bourne, “Corneal Reinnervation after LASIK: Prospective 3-Year Longitudinal Study,” *Investig. Opthalmology Vis. Sci.*, vol. 45, no. 11, p. 3991, Nov. 2004.

[49] B. H. Lee, J. W. McLaren, J. C. Erie, D. O. Hodge, and W. M. Bourne, “Reinnervation in the Cornea after LASIK,” *Invest. Ophthalmol. Vis. Sci.*, vol. 43, no. 12, p. 3660, 2002.

[50] M. A. Bragheeth and H. S. Dua, “Corneal sensation after myopic and hyperopic LASIK: clinical and confocal microscopic study.,” *Br. J. Ophthalmol.*, vol. 89, no. 5, pp. 580–5, May 2005.

[51] P. Kallinikos *et al.*, “Corneal nerve tortuosity in diabetic patients with neuropathy,” *Invest. Ophthalmol. Vis. Sci.*, vol. 45, no. 2, pp. 418–422, 2004.

[52] M. A. Dabbah, J. Graham, I. N. Petropoulos, M. Tavakoli, and R. A. Malik, “Automatic analysis of diabetic peripheral neuropathy using multi-scale quantitative morphology of nerve fibres in corneal confocal microscopy imaging,” *Med. Image Anal.*, vol. 15, no. 5, pp. 738–747, 2011.

[53] A. Zhivov *et al.*, “Imaging and Quantification of Subbasal Nerve Plexus in Healthy Volunteers and Diabetic Patients with or without Retinopathy,” *PLoS One*, vol. 8, no. 1, p. e52157, Jan. 2013.

[54] D. Ziegler *et al.*, “Early Detection of Nerve Fiber Loss by Corneal Confocal Microscopy and Skin Biopsy in Recently Diagnosed Type 2 Diabetes,” *Diabetes*, vol. 63, no. 7, pp. 2454–2463, Jul. 2014.

[55] M. Ferdousi *et al.*, “Corneal Confocal Microscopy Detects Small Fibre Neuropathy in Patients with Upper Gastrointestinal Cancer and Nerve Regeneration in Chemotherapy Induced Peripheral Neuropathy,” *PLoS One*, vol. 10, no. 10, p. e0139394, Oct. 2015.

[56] G. Ferrari *et al.*, “Corneal confocal microscopy reveals trigeminal small sensory fiber neuropathy in amyotrophic lateral sclerosis.,” *Front. Aging Neurosci.*, vol. 6, p. 278, 2014.

[57] L. Kass-Iliyya *et al.*, “Small fiber neuropathy in Parkinson’s disease: A clinical, pathological and corneal confocal microscopy study,” *Parkinsonism Relat. Disord.*, vol. 21, no. 12, pp. 1454–1460, Dec. 2015.

[58] M. K. Ikram, J. C. M. Witteman, J. R. Vingerling, M. M. B. Breteler, A. Hofman, and P. T. V. M. de Jong, “Retinal Vessel Diameters and Risk of Hypertension,” *Hypertension*, vol. 47, no. 2, pp. 189–194, 2006.

[59] T. T. Nguyen, J. J. Wang, and T. Y. Wong, “Retinal Vascular Changes in Pre-Diabetes and Prehypertension,” *Diabetes Care*, vol. 30, no. 10, pp. 2708–2715, 2007.

[60] R. S. Snell and M. A. Lemp, “The Orbital Blood Vessels,” in *Clinical Anatomy of the Eye*, Blackwell Science Ltd,., 1997, pp. 277–293.

[61] X. Wang, H. Cao, and J. Zhang, “Analysis of retinal images associated with hypertension and diabetes,” in *Engineering in Medicine and Biology Society, 2005. IEEE-EMBS 2005. 27th Annual International Conference of the*, 2006, pp. 6407–6410.

[62] M. D. Abràmoff, M. K. Garvin, and M. Sonka, “Retinal imaging and image analysis,” *Biomed. Eng. IEEE Rev.*, vol. 3, pp. 169–208, 2010.

[63] J. V. B. Soares, J. J. G. Leandro, R. M. J. Cesar, H. F. Jelinek, and M. J. Cree, “Retinal vessel segmentation using the 2-D Gabor wavelet and supervisedclassification,” *IEEE Trans Med Imaging*, vol. 25, no. 9, pp. 1214–1222, Sep. 2006.

[64] D. Marín, A. Aquino, M. Gegúndez-Arias, and J. Bravo, “A New Supervised Method for Blood Vessel Segmentation in Retinal Images by Using Gray-Level and Moment Invariants-Based Features,” *IEEE Trans Med Imaging*, vol. 30, no. 1, pp. 146–158, Jan. 2011.

[65] C. Sinthanayothin, J. F. Boyce, H. L. Cook, and T. H. Williamson, “Automated localisation of the optic disc, fovea, and retinal blood vessels from digital colour fundus images,” *Br. J. Ophthalmol.*, vol. 83, no. 8, pp. 902–910, 1999.

[66] J. Staal, M. Abràmoff, M. Niemeijer, M. Viergever, and B. Ginneken, “Ridge-Based Vessel Segmentation in Color Images of the Retina,” *IEEE Trans Med Imaging*, vol. 23, no. 4, pp. 501–509, Apr. 2004.

[67] Qin Li *et al.*, “A New Approach to Automated Retinal Vessel Segmentation Using Multiscale Analysis,” in *ICPR ’06: Proceedings of the 18th International Conference on Pattern Recognition*, 2006, vol. 4, pp. 77–80.

[68] S. Chaudhuri, S. Chatterjee, N. Katz, M. Nelson, and M. Goldbaum, “Detection of blood vessels in retinal images using two-dimensional matched filters,” *IEEE Trans. Med. Imaging*, vol. 8, no.

3, pp. 263–269, 1989.

[69] M. Sofka and C. V Stewart, “Retinal vessel centerline extraction using multiscale matched filters, confidence and edge measures,” *IEEE Trans Med Imaging*, vol. 25, no. 12, pp. 1531–1546, 2006.

[70] L. Wang, A. Bhalerao, and R. Wilson, “Analysis of Retinal Vasculature using a Multiresolution Hermite-Gaussian Model,” *IEEE Trans Med Imaging*, vol. 26, no. 2, pp. 137–152, 2007.

[71] A. Can, H. Shen, J. N. Turner, H. L. Tanenbaum, and B. Roysam, “Rapid Automated Tracing and Feature Extraction from Retinal Fundus Images Using Direct Exploratory Algorithms,” *IEEE Trans Inf Technol Biomed*, vol. 3, no. 2, pp. 125–138, Jun. 1999.

[72] O. Chutatape, L. Zheng, and S. M. Krishnan, “Retinal blood vessel detection and tracking by matched gaussian and kalman filters,” in *IEEE Engineering in Medicine and Biology Society*, 1998, vol. 20, no. 6, pp. 3144–3149.

[73] R. Pourreza, T. Banaee, H. Pourreza, and R. D. Kakhki, “A Radon Transform Based Approach for Extraction of Blood Vessels in Conjunctival Images,” in *MICAI 2008: Advances in Artificial Intelligence*, Berlin, Heidelberg: Springer Berlin Heidelberg, 2008, pp. 948–956.

[74] S. M. S. Zabihi, H. R. H. Pourreza, T. Banaee, S. M. S. Zabihi, H. R. H. Pourreza, and T. Banaee, “Vessel Extraction of Conjunctival Images Using LBPs and ANFIS,” *ISRN Mach. Vis.*, vol. 2012, pp. 1–6.

[75] J.-S. Lin, Y.-Y. Huang, and Y.-Y. Liao, “Extracting Blood Vessel in Sclera-Conjunctiva Image Based on Fuzzy C-means and Modified Cone Responses,” in *Recent Trends in Applied Artificial Intelligence*, M. Ali, T. Bosse, K. V. Hindriks, M. Hoogendoorn, C. M. Jonker, and J. Treur, Eds. Springer Berlin Heidelberg, 2013, pp. 556–565.

[76] P. Rodrigues *et al.*, “Two-dimensional segmentation of the retinal vascular network from optical coherence tomography,” vol. 18, no. 12, p. 126011, Dec. 2013.

[77] E. Ricci and R. Perfetti, “Retinal blood vessel segmentation using line operators and support vector classification,” *IEEE Trans Med Imaging*, vol. 26, no. 10, pp. 1357–1365, 2007.

[78] P. Kovesi, “Image Features from Phase Congruency,” *Videre J. Comput. Vis. Res. (MIT Press.*, vol. 1, no. 3, Feb. 1999.

[79] P. Kovesi, “Phase Congruency Detects Corners and Edges,” in *Digital Image Computing:*

Techniques and Applications - DICTA, 2003, pp. 309–318.

[80] T. Zhu *et al.*, "Fourier cross-sectional profile for vessel detection on retinal images.," *Comput. Med. Imaging Graph.*, vol. 34, no. 3, pp. 203–212, Feb. 2010.

[81] T. W. Secomb, J. P. Alberding, R. Hsu, M. W. Dewhirst, and A. R. Pries, "Angiogenesis: an adaptive dynamic biological patterning problem," *PLoS Comput. Biol.*, vol. 9, no. 3, p. e1002983, 2013.

[82] A. R. Pries, T. W. Secomb, and P. Gaehtgens, "Design principles of vascular beds," *Circ. Res.*, vol. 77, no. 5, pp. 1017–1023, 1995.

[83] A. R. Pries, B. Reglin, and T. W. Secomb, "Remodeling of blood vessels responses of diameter and wall thickness to hemodynamic and metabolic stimuli," *Hypertension*, vol. 46, no. 4, pp. 725–731, 2005.

[84] P. Vennemann, R. Lindken, and J. Westerweel, "In vivo whole-field blood velocity measurement techniques," *Exp. Fluids*, vol. 42, no. 4, pp. 495–511, 2007.

[85] P. Guimarães, "Blood Flow Velocity - Simulated Video Recordings." [Online]. Available: https://drive.google.com/drive/folders/0B5ujpT4F9zy6U1paektWQWZobEk?usp=sharing.

[86] E. I. Deryugina and J. P. Quigley, "Chick embryo chorioallantoic membrane model systems to study and visualize human tumor cell metastasis," *Histochem. Cell Biol.*, vol. 130, no. 6, pp. 1119–1130, Dec. 2008.

[87] A. M. Cimpean, D. Ribatti, and M. Raica, "The chick embryo chorioallantoic membrane as a model to study tumor metastasis," *Angiogenesis*, vol. 11, no. 4, pp. 311–319, Dec. 2008.

[88] D. Ribatti, "Chapter 5 Chick Embryo Chorioallantoic Membrane as a Useful Tool to Study Angiogenesis," *Int. Rev. Cell Mol. Biol.*, vol. 270, pp. 181–224, 2008.

[89] W. Xiang *et al.*, "Increased shear rate drives arteriolar collateral remodeling after acute microocclusion but might not concern venular collateral remodeling," *FASEB J.*, vol. 30, no. 1_Supplement, p. 721.10-, Apr. 2016.

[90] J. B. A. Maintz and M. A. Viergever, "A survey of medical image registration," *Med. Image Anal.*, vol. 2, no. 1, pp. 1–36, 1998.

[91] A. R. Pries, "A versatile video image analysis system for microcirculatory research.," *Int. J.*

Microcirc. Clin. Exp., vol. 7, no. 4, pp. 327–345, 1988.

[92] S. J. Orfanidis, *Introduction to signal processing*. Prentice Hall, 1996.

[93] F. Le Noble, V. Fleury, A. Pries, P. Corvol, A. Eichmann, and R. S. Reneman, “Control of arterial branching morphogenesis in embryogenesis: go with the flow,” *Cardiovasc. Res.*, vol. 65, no. 3, pp. 619–628, 2005.

[94] T. Fáncsi and G. Fehér, “Ultrastructural Studies of Chicken Embryo Chorioallantoic Membrane during Incubation,” *Anat. Histol. Embryol. J. Vet. Med. Ser. C*, vol. 8, no. 2, pp. 151–159, Jun. 1979.

[95] W. Xiang *et al.*, “Early adaptation of pre-existing collaterals after acute arteriolar and venular microocclusion: an in vivo study in chick chorioallantoic membrane,” in *Cardiovascular Research*, 2016, vol. 111, pp. S103--S103.

[96] E. Villani *et al.*, “In vivo confocal microscopy of the ocular surface: from bench to bedside,” *Curr. Eye Res.*, vol. 39, no. 3, pp. 213–31, Mar. 2014.

[97] D. V. Patel and C. N. McGhee, “Quantitative analysis of in vivo confocal microscopy images: A review,” *Surv. Ophthalmol.*, vol. 58, no. 5, pp. 466–475, 2013.

[98] S. Inoué, “Foundations of Confocal Scanned Imaging in Light Microscopy,” in *Handbook Of Biological Confocal Microscopy*, Boston, MA: Springer US, 2006, pp. 1–19.

[99] N. Lagali *et al.*, “Non-invasive imaging of peripheral nerve fiber degeneration in type 2 diabetes mellitus by wide-field corneal confocal microscopy and automated image processing,” *Submitt. to Ophthalmol.*, 2016.

[100] S. Allgeier *et al.*, “Mosaicking the Subbasal Nerve Plexus by Guided Eye Movements,” *Investig. Opthalmology Vis. Sci.*, vol. 55, no. 9, p. 6082, Sep. 2014.

[101] E. Poletti, J. Wigdahl, P. Guimaraes, and A. Ruggeri, *Automatic montaging of corneal sub-basal nerve images for the composition of a wide-range mosaic*. IEEE, 2014, pp. 5426–5429.

[102] S. Allgeier *et al.*, “Image Reconstruction of the Subbasal Nerve Plexus with In Vivo Confocal Microscopy,” *Investig. Opthalmology Vis. Sci.*, vol. 52, no. 9, p. 5022, Aug. 2011.

[103] F. Scarpa, E. Grisan, and A. Ruggeri, “Automatic Recognition of Corneal Nerve Structures in Images from Confocal Microscopy,” *Investig. Opthalmology Vis. Sci.*, vol. 49, no. 11, p. 4801,

Nov. 2008.

[104] E. Poletti and A. Ruggeri, “Automatic nerve tracking in confocal images of corneal subbasal epithelium,” in *Proceedings of the 26th IEEE International Symposium on Computer-Based Medical Systems*, 2013, pp. 119–124.

[105] C. Dehghani, N. Pritchard, K. Edwards, A. W. Russell, R. A. Malik, and N. Efron, “Fully Automated, Semiautomated, and Manual Morphometric Analysis of Corneal Subbasal Nerve Plexus in Individuals With and Without Diabetes,” *Cornea*, vol. 33, no. 7, pp. 696–702, Jul. 2014.

[106] K. Winter, P. Scheibe, B. Köhler, S. Allgeier, R. F. Guthoff, and O. Stachs, “Local Variability of Parameters for Characterization of the Corneal Subbasal Nerve Plexus,” *Curr. Eye Res.*, vol. 41, no. 2, pp. 186–198, Feb. 2016.

[107] I. N. Petropoulos *et al.*, “Rapid Automated Diagnosis of Diabetic Peripheral Neuropathy With In Vivo Corneal Confocal Microscopy,” *Investig. Opthalmology Vis. Sci.*, vol. 55, no. 4, p. 2071, Apr. 2014.

[108] R. Annunziata, A. Kheirkhah, S. Aggarwal, P. Hamrah, and E. Trucco, “A fully automated tortuosity quantification system with application to corneal nerve fibres in confocal microscopy images,” *Med. Image Anal.*, vol. 32, pp. 216–232, Aug. 2016.

[109] M. Parissi *et al.*, “Corneal nerve regeneration after collagen cross-linking treatment of keratoconus: a 5-year longitudinal study,” *JAMA Ophthalmol.*, vol. 134, no. 1, pp. 1–9, Jan. 2015.

[110] E. Meijering, M. Jacob, J.-C. F. Sarria, P. Steiner, H. Hirling, and M. Unser, “Design and validation of a tool for neurite tracing and analysis in fluorescence microscopy images,” *Cytom. Part A*, vol. 58A, no. 2, pp. 167–176, Apr. 2004.

[111] N. Cristianini and J. Shawe-Taylor, *An introduction to support vector machines : and other kernel-based learning methods*. Cambridge University Press, 2000.

[112] F. Scarpa, X. Zheng, Y. Ohashi, and A. Ruggeri, “Automatic evaluation of corneal nerve tortuosity in images from in vivo confocal microscopy,” *Invest. Ophthalmol. Vis. Sci.*, vol. 52, no. 9, pp. 6404–6408, 2011.

[113] J. Leckelt, P. Guimarães, A. Kott, A. Ruggeri, O. Stachs, and S. Baltrusch, “Early detection of diabetic neuropathy by investigating CNFL and IENFD in thy1-YFP mice.,” *J. Endocrinol.*, vol.

231, no. 2, pp. 147–157, Sep. 2016.

[114] F. Bucher *et al.*, “Small-Fiber Neuropathy Is Associated With Corneal Nerve and Dendritic Cell Alterations,” *Cornea*, vol. 34, no. 9, pp. 1114–1119, Sep. 2015.

[115] C. Schneider, F. Bucher, C. Cursiefen, G. R. Fink, L. M. Heindl, and H. C. Lehmann, “Corneal confocal microscopy detects small fiber damage in chronic inflammatory demyelinating polyneuropathy (CIDP),” *J. Peripher. Nerv. Syst.*, vol. 19, no. 4, pp. 322–327, Dec. 2014.

[116] D. Vagenas *et al.*, “Optimal Image Sample Size for Corneal Nerve Morphometry,” *Optom. Vis. Sci.*, vol. 89, no. 5, pp. 812–817, May 2012.

[117] M. Norberg, S. Wall, K. Boman, and L. Weinehall, “The Västerbotten Intervention Programme: background, design and implications,” *Glob. Health Action*, vol. 3, no. 0, Mar. 2010.

[118] K. Pourhamidi, L. B. Dahlin, K. Boman, and O. Rolandsson, “Heat shock protein 27 is associated with better nerve function and fewer signs of neuropathy,” *Diabetologia*, vol. 54, no. 12, pp. 3143–3149, Dec. 2011.

[119] S. Allgeier, B. Köhler, F. Eberle, S. Maier, and O. Stachs, “Elastische Registrierung von in-vivo-CLSM-Aufnahmen der Kornea,” *Bild. für die*, 2011.

[120] I. N. Petropoulos *et al.*, “The Inferior Whorl For Detecting Diabetic Peripheral Neuropathy Using Corneal Confocal Microscopy,” *Investig. Opthalmology Vis. Sci.*, vol. 56, no. 4, p. 2498, Apr. 2015.

[121] N. Pritchard *et al.*, “Utility of Assessing Nerve Morphology in Central Cornea Versus Whorl Area for Diagnosing Diabetic Peripheral Neuropathy,” *Cornea*, vol. 34, no. 7, pp. 756–761, Jul. 2015.

[122] T. Utsunomiya *et al.*, “Imaging of the Corneal Subbasal Whorl-like Nerve Plexus: More Accurate Depiction of the Extent of Corneal Nerve Damage in Patients With Diabetes,” *Investig. Opthalmology Vis. Sci.*, vol. 56, no. 9, p. 5417, Aug. 2015.

[123] M.-S. Jiang, Y. Yuan, Z.-X. Gu, and S.-L. Zhuang, “Corneal confocal microscopy for assessment of diabetic peripheral neuropathy: a meta-analysis.,” *Br. J. Ophthalmol.*, vol. 100, no. 1, pp. 9–14, Jan. 2016.

[124] E. E. B. De Clerck *et al.*, “New ophthalmologic imaging techniques for detection and monitoring of neurodegenerative changes in diabetes: a systematic review,” *Lancet Diabetes Endocrinol.*, vol. 3, no. 8, pp. 653–663, Aug. 2015.

[125] J. M. B. J. M. B. del Castillo, M. A. S. Wasfy, C. Fernandez, and J. Garcia-Sanchez, "An in vivo confocal masked study on corneal epithelium and subbasal nerves in patients with dry eye," *Invest. Ophthalmol. Vis. Sci.*, vol. 45, no. 9, pp. 3030–3035, Sep. 2004.

[126] S. De Cilla *et al.*, "Corneal subbasal nerves changes in patients with diabetic retinopathy: an in vivo confocal study," *Invest. Ophthalmol. Vis. Sci.*, vol. 50, no. 11, pp. 5155–5158, 2009.

[127] E. Villani, D. Galimberti, F. Viola, C. Mapelli, N. Del Papa, and R. Ratiglia, "Corneal Involvement in Rheumatoid Arthritis: An In Vivo Confocal Study," *Investig. Opthalmology Vis. Sci.*, vol. 49, no. 2, p. 560, Feb. 2008.

[128] G. C. Sturniolo *et al.*, "Small Fiber Peripheral Neuropathy in Wilson Disease: An In Vivo Documentation by Corneal Confocal Microscopy," *Invest. Ophthalmol. Vis. Sci.*, vol. 56, no. 2, pp. 1390–1395, Feb. 2015.

[129] E. Grisan, M. Foracchia, and A. Ruggeri, "A Novel Method for the Automatic Grading of Retinal Vessel Tortuosity," *IEEE Trans. Med. Imaging*, vol. 27, no. 3, pp. 310–319, Mar. 2008.

[130] W. E. W. Hart, M. Goldbaum, B. Côté, P. Kube, and M. R. Nelson, "Measurement and classification of retinal vascular tortuosity," *Int. J. Med. Inform.*, vol. 53, no. 2, pp. 239–252, 1999.

[131] A. A. Kalitzeos, G. Y. H. Lip, and R. Heitmar, "Retinal vessel tortuosity measures and their applications," *Exp. Eye Res.*, vol. 106, pp. 40–46, 2013.

[132] E. Trucco, H. Azegrouz, and B. Dhillon, "Modeling the Tortuosity of Retinal Vessels: Does Caliber Play a Role?," *IEEE Trans. Biomed. Eng.*, vol. 57, no. 9, pp. 2239–2247, Sep. 2010.

[133] R. Annunziata, A. Kheirkhah, S. Aggarwal, B. M. Cavalcanti, P. Hamrah, and E. Trucco, "Two-Dimensional Plane for Multi-Scale Quantification of Corneal Subbasal Nerve Tortuosity," *Investig. Opthalmology Vis. Sci.*, vol. 57, no. 3, p. 1132, Mar. 2016.

[134] N. Lagali *et al.*, "Focused Tortuosity Definitions Based on Expert Clinical Assessment of Corneal Subbasal Nerves," *Investig. Opthalmology Vis. Sci.*, vol. 56, no. 9, p. 5102, Aug. 2015.

[135] B. M. Hoşal, N. Örnek, G. Zilelioğlu, and A. H. Elhan, "Morphology of corneal nerves and corneal sensation in dry eye: a preliminary study," *Eye*, vol. 19, no. 12, pp. 1276–1279, Dec. 2005.

[136] Ö. Smedby *et al.*, "Two-Dimensional Tortuosity of the Superficial Femoral Artery in Early Atherosclerosis," *J. Vasc. Res.*, vol. 30, no. 4, pp. 181–191, 1993.

[137] E. Bullitt, G. Gerig, S. M. Pizer, Weili Lin, and S. R. Aylward, “Measuring tortuosity of the intracerebral vasculature from MRA images,” *IEEE Trans. Med. Imaging*, vol. 22, no. 9, pp. 1163–1171, Sep. 2003.

[138] P.-Y. Chang *et al.*, “Decreased Density of Corneal Basal Epithelium and Subbasal Corneal Nerve Bundle Changes in Patients with Diabetic Retinopathy,” *Am. J. Ophthalmol.*, vol. 142, no. 3, p. 488–490.e1, Sep. 2006.